# Climate Tipping Points

## Assessing the Probabilities of Triggering Them and the Amplification of Global Warming from Tipping Points within the Earth's Carbon Cycle

---

## Master's Thesis

M.Sc. Integrated Climate System Sciences

**University Hamburg**


**Author:** Jakob Deutloff

**Matriculation Number:** 7376514

**First Examiner:** Prof. Dr. Tim Lenton

**Second Examiner:** Prof. Dr. Hermann Held


**April 2023**

**Topic:** The likelihood of multiple climate tipping points being triggered by continued anthropogenic greenhouse gas emissions.

# Abstract

Continued global warming is increasing the risk of critical threshold temperatures being crossed for several tipping elements. This would commit them to abrupt and largely irreversible change with negative impacts on human well-being. The Earth's carbon cycle contains tipping elements having the potential to further increase this risk, as they store significant amounts of carbon that could be released once they are triggered. In this study, we assess the possible impacts of the two major tipping elements in the Earth's carbon cycle – the Amazon rainforest and permafrost – and calculate the probabilities of triggering for 16 tipping elements under various shared socioeconomic pathway (SSP) scenarios up to the year 2500. To conduct our analysis, we use the intermediate complexity climate model FaIR which is coupled to a conceptual model of the tipping processes within the Amazon rainforest and permafrost. Uncertainties are propagated by employing a Monte Carlo approach for the construction of large model ensembles. We find that the highest short-term temperature increase from permafrost and Amazon carbon emissions becomes possible under SSP5-8.5 with 0.4°C ($0.09 - 1.1$°C) in 2100. However, this temperature anomaly decreases since atmospheric $CH_4$ concentration anomalies are decreasing after 2100 and the highest long-term temperature increase from permafrost and Amazon carbon emissions becomes possible under SSP2-4.5 with 0.16°C ($0.03 - 0.91$°C) in 2500. Carbon emissions from permafrost and the Amazon have the potential to cause super-linearities in the transient climate response to cumulative anthropogenic $CO_2$ emissions. Moreover, they reduce the feasibility of temperature targets, increasing the probability of exceeding 2°C in 2100 under SSP1-1.9 from 9.86% to $13.5 \pm 0.39$%. Furthermore, carbon emissions from permafrost and the Amazon increase the probabilities of triggering other tipping elements. Tipping elements become more likely than not to be triggered on average 9.3 years earlier if those carbon emissions are included. Our findings emphasize the urgent need for emission reduction to mitigate the risk of triggering multiple tipping elements. The probability of tipping until 2500 on average over all tipping elements and without taking carbon emissions from the Amazon or permafrost into account is 28% under SSP1-1.9, 38% under SSP1-2.6, 65% under SSP2-4.5, 92% under SSP3-7.0, and 95% under SSP5-8.5. The highest increase in this number caused by additional carbon emissions from the Amazon and permafrost is observed under SSP2-4.5 with 3.3%. It is unlikely that tipping events can be entirely avoided, since our analysis indicates that even under SSP1-1.9 five tipping elements are more likely to be triggered than not.

# Table of Contents

# List of Abbreviations

| | |
|---|---|
| AMAZ | Amazon rainforest |
| AMOC | Atlantic meridional overturning circulation |
| AOGCM | Atmosphere-ocean general circulation model |
| AWSI | Arctic winter sea ice |
| BARI | Barents Sea winter ice |
| BORF | Boreal forest abrupt dieback |
| CTEM | Carbon tipping elements model |
| CMIP6 | Coupled model intercomparison project phase 6 |
| EAIS | East Antarctic ice sheet |
| EASB | East Antarctic subglacial basins |
| ERF | Effective radiative forcing |
| ESM | Earth System Model |
| FaIR | Finite amplitude Impulse Response model |
| GCM | Global climate model |
| GHG | Greenhouse gas |
| GLCR | Mountain Glaciers |
| GMSL | Global mean sea level |
| GMST | Global mean surface temperature |
| GPP | Gross primary production |
| GRIS | Greenland ice sheet |
| GSP | Green Sahara period |
| LABC | North Atlantic Subpolar Gyre – Labrador and Irminger Sea Convection |
| MB | Mass balance |
| MAGICC | Model for the Assessment of Greenhouse Gas Induced Climate Change |
| MICI | Marine ice cliff instability |
| MISI | Marine ice sheet instability |
| NEP | Net ecosystem production |
| PFAT | Boreal permafrost abrupt thaw |
| PFTP | Boreal permafrost collapse |
| pp | Percent points |
| RCP | Representative concentration pathway |
| REEF | Warm water coral reefs |
| RMSE | Root-mean-square error |
| SAHL | Sahel vegetation and West African monsoon |
| SLE | Sea level equivalent |
| SMB | Surface mass balance |
| SOC | Soil organic carbon |
| SPG | Subpolar Gyre |
| SSP | Shared socioeconomic pathway |
| TE | Tipping Element |
| TCRE | Transient climate response to cumulative $CO_2$ emissions |
| TUND | Boreal forests northern expansion |
| WAIS | West Antarctic ice sheet |
| WAM | West African monsoons |

# 1 Introduction

The term "tipping point" is commonly used to describe a critical threshold in the forcing of a system, at which small additional forcing leads to significant and long-term changes of the system (Lenton et al., 2008). The debate about tipping points in the climate system, referred to as "climate tipping points", has intensified over the past two decades. Increasing numbers of Earth system components have been identified which could possibly exhibit tipping behaviour (e.g., Lenton et al., 2008; Kriegler et al., 2009; Steffen et al., 2018), with 15 candidates being shortlisted in the latest IPCC report (Lee et al., 2021). These Earth system components are referred to as "tipping elements" (TEs) and occur within the biosphere, cryosphere and oceanic or atmospheric circulation (Lenton et al., 2008). The global mean surface temperature (GMST) relative to pre-industrial levels is used as a common metric to describe the forcing of the TEs (Armstrong McKay et al., 2022). This means that a tipping point can be associated with a "threshold temperature" after which the respective TE is expected to exhibit tipping behaviour (more detailed definition of TEs and tipping points in Sec.1.1). There is growing concern about the possible proximity of climate tipping points, as threshold temperatures have been revised to lower levels, with some TEs being at risk of getting "triggered" (crossing of their threshold temperature) at GMST values as low as 1°C (Lenton et al., 2019).

Additional complexity is added to the tipping points debate by interactions between different TEs, where triggering of one TE makes the triggering of others more or less likely (Kriegler et al., 2009; Lenton et al., 2019). Those causal interconnections can either have a stabilizing or destabilizing effect on the network of TEs, and are therefore either decreasing or increasing the probability of tipping cascades with domino-like tipping of several TEs. A first set of five interconnected TEs consisting of the Atlantic meridional overturning circulation, the Greenland and West Antarctic ice sheets, the Amazon rainforest and the El Niño – Southern Oscillation has been proposed by Kriegler et al. (2009), based on an expert elicitation. As current Earth system models (ESMs) [1] are unable to comprehensively represent the interactions between TEs, more conceptual models must be used to study them (Wood et al., 2019). Using a conceptual dynamic network model based on the estimates of Kriegler et al. (2009), Wunderling et al. (2021) found that TE interactions tend to destabilize the network of TEs and make tipping cascades more likely.

Cascade-like tipping of TEs within the Earth's carbon cycle after crossing a planetary threshold

[1] Two different types of global climate models (GCMs) must be distinguished: atmosphere-ocean general circulation models (AOGCMs) that are unable to predict atmospheric carbon concentrations from carbon emissions due to an incomplete or lacking representation of the carbon cycle and ESMs that have this ability (Meinshausen et al., 2020).

of 2°C of warming might further amplify global warming and therefore lead to a "hothouse Earth" with significantly higher global temperatures than in the Holocene (Steffen et al., 2018). The hypothesis of a planetary threshold challenges the concept of the transient climate response to cumulative $CO_2$ emissions (TCRE), which assumes that GMST is responding near-linearly to cumulative anthropogenic $CO_2$ emissions, with $1000\,GtCO_2$ of cumulative $CO_2$ emissions likely causing a 0.27°C to 0.63°C increase in GMST (IPCC, 2021). Steffen et al. (2018) assume that such a planetary threshold could be produced by thawing permafrost and dieback of the Amazon rainforest and boreal forests in response to global warming, together with a weakening of carbon uptake by ocean and land systems relative to human forcing. The latter is well represented in current ESMs from the coupled model intercomparison project phase 6 (CMIP6) (Eyring et al., 2016; Canadell et al., 2021). However, permafrost thaw, Amazon rainforest dieback, and Boreal forest dieback are assumed to include tipping points, which are not well resolved by ESMs (Armstrong McKay et al., 2022; Wunderling et al., 2021). In particular, the Amazon rainforest and permafrost have been identified as the two TEs with the highest potential to substantially increase atmospheric carbon concentrations (Canadell et al., 2021).

As the abrupt changes of the TEs that are assumed to unfold after the respective threshold temperature is crossed are in general negatively affecting human livelihoods, the proximity of tipping points calls for rapid reduction of anthropogenic greenhouse gas (GHG) emissions to limit global warming to 1.5°C to avoid tipping of multiple TEs (Schellnhuber et al., 2016). This is support by integrated assessment modelling studies, yielding significantly higher social costs of carbon if economic impacts from TEs are included (Cai et al., 2015; Dietz et al., 2021; Lontzek et al., 2015). If interactions between the tipping elements are allowed for within those models, the increase in the social cost of carbon is even more pronounced (Cai et al., 2016).

If all pledges made by governments are fully implemented on time, global warming can be limited to just under 2°C (Meinshausen et al., 2022). Even under this high-end mitigation scenario, multiple TEs become likely to be triggered (Armstrong McKay et al., 2022). However, current real world policies and actions are leading to a temperature increase of around 2.7°C in 2100 (Climate Action Tracker, 2022), with accordingly higher chances to trigger an increasing number of TEs. It remains challenging to make precise statements about how safe an emission scenario is with respect to triggering multiple TEs due to uncertainties within the temperature response of the climate system to anthropogenic GHG emissions and within the threshold temperatures (Forster et al., 2021; Lenton et al., 2019), with potential interactions between TEs adding to this uncertainty (Wunderling et al., 2021).

In this study, we aim to bridge this gap by calculating the probabilities of triggering any of today's know TEs under various emission scenarios. Furthermore, we estimate the possible carbon emissions and the caused increase of GMST from tipping of the Amazon rainforest and permafrost, the two major TEs within the Earth's carbon cycle which we hereafter refer to as the "carbon tipping elements". We use those estimates to explore by how much the probabilities of tipping of other TEs are increased by carbon TEs. To do this, we rely on a recent literature review carried out by Armstrong McKay et al. (2022), which is the first comprehensive reassessment of the TEs, their threshold temperatures, timescales, and impacts since Lenton et al. (2008). The updated shortlist emerging from this study includes 16 TEs with threshold temperatures between 0.8°C and 10°C. We use an intermediate complexity climate model which is coupled to a conceptual model of the carbon TEs for the construction of large model ensembles following a Mont Carlo approach (Metropolis et al., 1953) to propagate the uncertainties. Our results cover a comparatively long period of time, namely up to the year 2500.

In the following parts of the introduction, we provide a detailed definition of TEs and tipping points, followed by a description of the 16 TEs within the Earth system. Furthermore, we present recent estimates of carbon emissions from the carbon TEs and introduce our model approach.

## 1.1 Defining Tipping Elements and Tipping Points

This study is based on the comparably broad definition of a TE and its respective tipping point provided by Lenton et al. (2008) and further refined by Armstrong McKay et al. (2022). Large-scale subsystems or components ($\Sigma$) of the Earth system are referred to as TEs if they can be switched into a qualitatively different state by a small perturbation (Lenton et al., 2008; Lenton, 2011). The tipping point is the corresponding critical point in the forcing of the system $\Sigma$, at which a small additional forcing will lead to a qualitatively altered state of the system in the future. This can be formally defined by identifying a single control parameter ($\rho$) of the system for which a critical value ($\rho_{\text{crit}}$) exists from which a small perturbation ($\delta\rho > 0$) leads to a qualitative change ($\hat{F}$) in a crucial system feature ($F$) after some observation time ($T > 0$). The change of $F$ is measured with respect to a reference state of $F$ at $\rho_{\text{crit}}$:

$$|\Delta F| = |F(\rho \geq \rho_{\text{crit}} + \delta\rho|T) - F(\rho_{\text{crit}}|T)| \geq \hat{F} > 0,$$

with $\hat{F}$ being significantly higher than the natural variability of $F$ (Lenton et al., 2008). The critical point in the forcing $\rho_{\text{crit}}$ is the tipping point of the TE $\Sigma$ with the crucial system

feature $F$.

We note, that this definition does not require the qualitative change of the system feature to be irreversible, to happen abrupt, i.e., faster than the cause, or to be self-perpetuating and does therefore include phase transitions as well as bifurcations. Hence, it differs in that sense from more strict definitions, which require TEs to be self-perpetuating (e.g., Levermann et al., 2012; Armstrong McKay et al., 2022). According to the definition of Armstrong McKay et al. (2022), systems that are not self-perpetuating beyond a certain critical forcing but simply amplify a perturbation are classified as threshold-free feedbacks.

Tipping elements are defined to be at least of sub-continental scale (length scale of order $\sim 1000\,\mathrm{km}$) (Lenton et al., 2008). This definition has been extended by Armstrong McKay et al. (2022), who distinguish between "global core" and "regional impact" TEs. To qualify as a global core TE, a tipping point has to occur uniformly across a sub-continental scale for a subsystem. However, if the change in forcing is fairly uniform across a large spatial area, small-scale tipping points can be crossed near-synchronously at a sub-continental scale, which qualifies the affected subsystem as a regional impact TE.

To be classified as policy-relevant, TEs also have to fulfil the following three conditions (Lenton et al., 2008):

1. Humans infer with the TE such that decisions taken within a "political" time horizon ($\sim 100\,\mathrm{yr}$) determine whether the respective tipping point is crossed.

2. The qualitative change is observed within an "ethical" time horizon, which is usually defined as $\sim 1000\,\mathrm{yr}$ (Lenton et al., 2008) but was relaxed to $\sim 10\,\mathrm{kyr}$ by Armstrong McKay et al. (2022).

3. A significant number of people are concerned about the fate of the TE because

   i) it contributes significantly to the overall mode of operation of the Earth System;

   ii) it contributes significantly to human welfare;

   iii) it has great value in itself as a unique feature of the biosphere.

Point three has been used by Armstrong McKay et al. (2022) to further distinguish between global core and regional impact TEs, with the former having to meet (i) whereas the latter have to meet either (ii) or (iii) but not (i).

## 1.2 Tipping Elements within the Earth System

This section gives an overview over the 16 TEs within the Earth system that are currently identified (Armstrong McKay et al., 2022). For each TE, we describe its role within the Earth system, discuss the individual feedback mechanisms that are expected to produce a tipping point and present evidence for tipping dynamics. Furthermore, we revisit the estimates of the threshold temperature, the timescale, and, if applicable, the carbon emissions of each TE from Armstrong McKay et al. (2022) our further analysis is largely based on (See Tab. 1 for a summary). A special emphasis is put on the description of the carbon TEs permafrost and the Amazon rainforest.

### 1.2.1 Permafrost

Soils in cold regions like the Arctic contain perennially frozen layers, which are defined as permafrost if their temperature is at or below 0°C for two consecutive years (Burke et al., 2020). Permafrost soils are estimated to span an area of $13.9 \cdot 10^6\,\mathrm{km}^2$ (ca. 15% of the exposed land area) (Obu et al., 2019) and predominantly occur in high northern latitudes in a periglacial environment characterized by a cold, but not glacial, climate (Dobinski, 2011). A rough classification of permafrost soils is made by defining continuous permafrost as regions with $> 90\%$ of the land surface being underlain by permafrost and discontinuous permafrost as regions containing smaller amounts of permafrost (Schuur et al., 2015). Generally, continuous permafrost is found further north than discontinuous permafrost, with thick sediments overlying bedrock occurring in both permafrost regions (Fig. 1 in Schuur et al., 2015).

Historically, ecosystems within this region have been a net carbon sink (Lindgren et al., 2018), characterized by a positive net ecosystem production (NEP), which is the accumulation of carbon within the ecosystem. The NEP is defined as the difference between carbon gains of an ecosystem by gross primary production (GPP) and carbon losses from the ecosystem by plant respiration ($R_{\mathrm{plant}}$), heterotrophic respiration ($R_{\mathrm{het}}$), leaching of carbon from soils ($F_{\mathrm{leach}}$) and carbon fluxes due to disturbances ($F_{\mathrm{dist}}$), e.g., due to fire (Chapin 3. et al., 2002):

$$NEP = GPP - R_{\mathrm{plant}} - R_{\mathrm{het}} - F_{\mathrm{leach}} - F_{\mathrm{dist}}.$$

Positive values of NEP for permafrost ecosystems are the result of low carbon losses rather than high GPP (Grosse et al., 2011). These low carbon losses can, in turn, mainly be explained by low values of $R_{\mathrm{het}}$, caused by reduced decomposition rates of soil organic carbon (SOC) by soil fauna and microorganisms due to the perennially frozen conditions, low temperatures and widespread water-saturation (Mishra et al., 2021).

The carbon pool stored within the northern permafrost region is estimated to be $1460 - 1600\,\mathrm{GtC}$, of which $1070 - 1360\,\mathrm{GtC}$ are stored within permafrost soils and deposits (Canadell et al., 2021). This makes permafrost soils the largest terrestrial organic carbon pool on Earth (Walter Anthony et al., 2018), with northern permafrost regions containing about twice as much carbon as the atmosphere (Schuur et al., 2015). Surface soils ($0 - 3\,\mathrm{m}$) are estimated to contain the biggest share of this pool, with $1014^{+194}_{-175}\,\mathrm{GtC}$ (Mishra et al., 2021). The yedoma region, with deep permafrost carbon deposits ($> 3\,\mathrm{m}$), is reported to contain $327 - 466\,\mathrm{GtC}$, with $83 - 250\,\mathrm{GtC}$ from yedoma deposits, 114 GtC in taberal deposits and $130 - 213\,\mathrm{GtC}$ in thermokarst deposits (Strauss et al., 2017). Arctic river deltas also contain deep permafrost carbon deposits and store $96 \pm 55\,\mathrm{GtC}$ (Strauss et al., 2017). Additional carbon pools might exist in deep permafrost sediments outside the yedoma region, potentially containing another $\sim 400\,\mathrm{GtC}$, while subsea continental shelves below the Arctic Ocean contain an uncertain amount of carbon (Schuur et al., 2015). It must be noted, that the estimate for carbon stored within the upper 3 m includes carbon stored within this depth range from the yedoma region and Arctic river deltas.

Arctic amplification is causing temperatures in the Arctic region to rise about twice as fast as the global average temperature, making this region especially vulnerable to global warming (Schuur et al., 2015). Anthropogenic warming is already observable in permafrost soils, with a warming of $0.39 \pm 0.15$°C near the depth of zero annual temperature cycle over the 2007-2016 period (Biskaborn et al., 2019). Rising permafrost temperatures cause increased thawing of permafrost soils, which makes the stored SOC vulnerable to microbial decomposition (Elberling et al., 2013) (increase in $R_{\mathrm{het}}$) and is expected to increase GHG emissions from permafrost soils, making permafrost regions a net source of carbon (Schuur et al., 2015). The IPCC AR6 report assigned high confidence to the statement that some permafrost regions are already a net source of carbon (Canadell et al., 2021). The increased GHG emissions from permafrost soils, in turn, amplify global warming, resulting in a self-reinforcing positive feedback loop, which might exhibit tipping point dynamics (Clarke et al., 2021).

Quantifying future carbon emissions from permafrost thaw is necessary to assess possible reductions of carbon emission budgets. This is particularly interesting for overshoot scenarios, as permafrost thaw is assumed to be irreversible on centennial timescales (Schuur et al., 2015). However, modelling of permafrost soils remains highly challenging due to limited knowledge and model representation of key drivers and relationships within the permafrost response to global warming, with the main ones being discussed in the following.

Small-scale properties ($\mathcal{O}(10\,\mathrm{m})$) like water saturation caused by the topography or snow cover crucially determine the evolution of permafrost (Zhang et al., 2013). Waterlogged soils

emit methane from anaerobic respiration of microbes, whereas dry soils emit comparably higher levels of $CO_2$ from aerobic respiration (Schuur et al., 2015). However, most land surface models (e.g., Schneider von Deimling et al., 2015; Comyn-Platt et al., 2018), and especially ESMs do not resolve topography on these scales due to computational limitations (Zhang et al., 2013), which causes the relative contribution of $CO_2$ and $CH_4$ to permafrost carbon emissions to be poorly constrained (Canadell et al., 2021).

Furthermore, the decomposition rate of SOC from thawing permafrost depends on microbe activity, which might lead to complete decomposition of the stored SOC on a much shorter timescale ($\mathcal{O}(10\,\text{years})$) than expected in ESMs (compare Oechel et al., 2000; Burke et al., 2017).

Another key process leading to uncertainties in permafrost modelling are peatland fires, which can lead to a rapid release of carbon from permafrost peatlands to the atmosphere and warm the permafrost soils below the peat (Hugelius et al., 2020).

Additionally, the response of vegetation in the permafrost region to warmer temperatures and less permafrost soils is highly uncertain (McGuire et al., 2018), making it hard to predict whether the amount of carbon emitted from the soil could be offset by a more productive vegetation or not. Such an increase in vegetation productivity is associated with northward expansion of boreal forests, which is also assumed to include tipping points and is discussed in Sec. 1.2.3. Due to the additional uncertainties introduced by vegetation and to avoid overlaps with the northward expansion of boreal forests, this study and all estimates of permafrost carbon emissions cited therein do not include carbon uptake or release by vegetation.

Despite the high uncertainties involved in predicting permafrost thaw, consensus exists that it is governed by gradual and abrupt thaw processes (Canadell et al., 2021; Turetsky et al., 2020; Schuur et al., 2015). Additionally, collapse of permafrost might be possible in some regions (Armstrong McKay et al., 2022; Lenton, 2012). In the following, we discuss those three thaw processes, possible associated tipping points and the expected carbon losses.

**Gradual Thaw**

Rising temperatures in the northern permafrost region lead to a deepening of the active layer into perennially frozen permafrost layers, increasing the amount of thawed SOC and the length of the thawing period (Canadell et al., 2021). This gradual thawing of permafrost affects the surface of the frozen ground and slowly penetrates downwards ($\mathcal{O}(10^{-2}\,\text{m yr}^{-1})$ (Turetsky et al., 2019).

In their recent literature review, Armstrong McKay et al. (2022) classify gradual thaw of

boreal permafrost as a threshold-free feedback (high confidence), becoming widespread at global warming of 1.5 °C (1 to 2.4°C) (high confidence) with carbon emissions of 20 GtC $°C^{-1}$ in 2100 and 50 GtC $°C^{-1}$ in 2300 up to a maximum of 260 GtC (medium confidence), occurring over a timescale of 300 years (100 to >300 years) (medium confidence).

**Abrupt Thaw**

Parts of the northern permafrost region are susceptible to localized abrupt thawing processes, happening on a timescale of days or weeks, affecting several meters of the permafrost column (Turetsky et al., 2019). Abrupt thaw is caused by thermokarsts, the process of thawing ice-rich permafrost soils causing land-subsidence which results in the development of distinct landforms, further amplifying permafrost thaw or erosion (Olefeldt et al., 2016). Unlike gradual thaw, abrupt thaw of permafrost occurs at a natural baseline rate independent of global warming (Turetsky et al., 2020). Thermokarst landforms and areas susceptible to thermokarst development cover $\sim$ 20% of the northern permafrost region (Olefeldt et al., 2016).

Three broad categories of thermokarst landscapes can be classified (Olefeldt et al., 2016):

- Wetland thermokarst landscapes including landforms such as thermokarst bogs, fens, or shore fens (Jorgenson, 2013; Kokelj and Jorgenson, 2013).
- Lake thermokarst landscapes including landforms such as shallow, deep, and glacial thermokarst lakes and thermokarst lake basins (Jorgenson, 2013; Kokelj and Jorgenson, 2013). These landforms mark different states in the life-cycle of thermokarst lakes, which are characterized by initiation, expansion, drainage, and drainage basin development.
- Hillslope thermokarst landscapes including landforms such as active layer detachment slides, retrogressive thaw slumps, thermal erosion gullies, beaded streams, and thermokarst water tracks (Jorgenson, 2013; Kokelj and Jorgenson, 2013).

Which landform develops after a thermokarst depends on the prevailing conditions at the site (Olefeldt et al., 2016).

As abrupt thaw of boreal permafrost (PFAT) is expected to happen localized but near-synchronously on a subcontinental scale, Armstrong McKay et al. (2022) classify it as a regional impact tipping point (medium confidence), amplifying carbon emissions from gradual thaw by $25 - 75\%$ up to $60 - 195$ GtC (medium confidence) with a threshold temperature of 1.5°C (1 to 2.3°C) (medium confidence) over a timescale of 200 years (100 to 300 years) (medium confidence). Furthermore, the timescale of tipping is assumed to be partially rate-dependent, with higher exceedance of the threshold temperature leading to shorter a

timescale.

**Permafrost Collapse**

Collapse of permafrost can be caused by permafrost degradation becoming self-perpetuating due to the heat released by microbial respiration of SOC, leading to further thaw of permafrost and resulting in a positive feedback loop, which is referred to as the "compost bomb instability" (Luke and Cox, 2011). This process might occur in the yedoma region or in abruptly dried permafrost soils (Armstrong McKay et al., 2022).

The yedoma region in Siberia and Alaska includes the thickest permafrost soils, reaching thicknesses of up to 50 m (Schirrmeister et al., 2013). These deposits consist of carbon- and ice-rich loess and fluvial reworked sediments (Van Huissteden, 2020, p. 32). While covering only 7% of the permafrost area (Hugelius et al., 2014), the yedoma region contains about 33% of the total carbon stored in northern permafrost soils (compare estimates of carbon pools above) and ground ice can occupy up to 80% of the ground volume (Schuur et al., 2015). Since SOC in yedoma and thermokarst deposits is partly in low-decomposition state (Strauss et al., 2015), it is highly vulnerable to microbial decomposition (Strauss et al., 2017). This vulnerability is further amplified by the high ground-ice content, making thermokarst processes likely.

The compost bomb instability could also be triggered in permafrost soils with reduced soil moisture, causing suppressed heat conductivity (Luke and Cox, 2011). Abrupt drying of permafrost soils creating such conditions has been found to occur in 2.2 million $km^2$ if global warming exceeds 4°C (Teufel and Sushama, 2019).

Armstrong McKay et al. (2022) classify boreal permafrost collapse (PFTP) due to compost bomb instabilities in both the yedoma region and abruptly dried permafrost soils as a global core tipping point (low confidence). Carbon emissions of 125 to 250 GtC (low confidence) are expected to be released over 50 years (10-300 years) (medium confidence) after a threshold temperature of 4°C (3 to 6°C) (low confidence) is crossed. The timescale of tipping is assumed to be partially rate-dependent.

### 1.2.2 Amazon Rainforest

The Amazon rainforest (AMAZ) is the world's largest tropical forest, covering most of the Amazon basin and expanding over an area of $7.25 \cdot 10^6\,km^2$ (Gatti et al., 2021). It is a highly complex ecosystem which is to a large degree self-sustaining. Also, it is home to a remarkable share of global biodiversity, with more tree-species being found in 10.000 $m^2$ than in the whole of Europe (Dirzo and Raven, 2003; Gentry, 1988). Furthermore, the

Amazon is an integral component of the Earth's carbon cycle, accounting for around 16% of terrestrial productivity (Science Panel for the Amazon, 2021) and acting as a carbon sink in the past, storing about 0.54 $GtCyr^{-1}$ in the 1990s (Brienen et al., 2015). Sequestration of atmospheric carbon led to the formation of a total carbon pool of 150–200 GtC stored in the soils and vegetation of the Amazon rainforest (Gatti et al., 2021; Science Panel for the Amazon, 2021). However, the nature of the Amazon carbon pool is fundamentally different to the one found in permafrost regions, where most carbon is stored in the soils (Sec. 1.2.1). Tropical rainforests are generally characterized by high GPP but also high losses of organic carbon due to respiration and leaching, which results in the majority of the organic carbon being stored in the living biosphere rather than in the soils (Chapin 3. et al., 2002). In 2007, around 70% of the total carbon stored in America's rainforest were contained in living biomass, deadwood and litter, and only 30% were stored in the soils (Pan et al., 2011).

Several biogeophysical processes between the biosphere and atmosphere in the Amazon secure the existence of the forest (Science Panel for the Amazon, 2021). Some of the most essential ones are hydraulic redistribution of water from deep-rooted trees to shallow-rooted plants, a decrease of land surface temperature by evapotranspiration and the recycling of rainfall by trees, where trees transpire rainwater back to the atmosphere (Science Panel for the Amazon, 2021). On average, around 32% of the Amazonian rainfall originates from the basin (Staal et al., 2018). These biogeophysical processes are vital to secure the wet climate the forest needs to exist, especially during the dry season (Science Panel for the Amazon, 2021). Tree loss due to climate change or deforestation is considered to interrupt those self-sustaining biogeophysical processes. This would destabilize the Amazon rainforest and potentially trigger a positive feedback, which could tip the forest into a highly degraded state and turn it from a carbon sink into a carbon source (Nobre et al., 2016; Science Panel for the Amazon, 2021). Forest-fire-feedbacks could accelerate this degradation, as an open canopy allows for greater solar heating and air movement which dries out forest fuels, making them more susceptible to fire (Cochrane et al., 1999).

Impacts of deforestation and global warming on the Amazon rainforest are already observable. Recent aircraft measurements show that the southeast of the Amazon has already become a net carbon source (Gatti et al., 2021). This degradation might accelerate since the resilience of two thirds of the forest is decreasing since the early 2000s, as shown by the evaluation of remotely measured vegetation optical depth (Boulton et al., 2022). Currently, $\sim 40\%$ of the Amazon forest is estimated to be in a bistable state, and this area is projected to increase under continued global warming (Staal et al., 2020).

Synthesizing the literature, Armstrong McKay et al. (2022) classify the Amazon forest as a

global core TE (medium confidence) with a threshold temperature of 3.5°C (2 to 6°C) (low confidence) independent of deforestation. They estimate the timescale to be 100 years (50 to 200 years) (low confidence) and carbon emissions of 30 GtC for a partial dieback (40%) and 75 GtC for a total dieback of the Amazon rainforest (medium confidence). The timescale is again assumed to be partially rate-dependent.

### 1.2.3 Boreal Forests

Forests within the boreal zone encompass almost 30% of the global forest area and store $272 \pm 23$ GtC of carbon, of which 60% is stored in the soil, 20% in biomass, and the rest in deadwood and litter (Crowther et al., 2015; Pan et al., 2011). If soil carbon is excluded, boreal forests make up for about 20% of the total carbon sequestered by global forests. (Pan et al., 2011; Gauthier et al., 2015). As boreal forests are in part growing on permafrost soils (Gauthier et al., 2015), the estimate for carbon stored in boreal forest soils is partially included in the permafrost carbon pool. Besides of functioning as a major carbon pool, boreal forests impact the global climate via their albedo and the soil moisture recycling. In the winter, the low albedo trees "mask" the high albedo snow surfaces and do thereby lead to a warmer climate, whereas in summer, boreal forests cool the climate via enhanced evapotranspiration (Bonan, 2008). Adding to the importance of boreal forests, they are widely used for wood production, with 33% of the global production of sawn wood and 25% of paper originating from boreal forests (Burton, Philip J. et al., 2010).

Based on satellite observations, three alternative modes in the frequency distribution of boreal tree cover have been identified: a treeless state, an open woodland state and a closed forest state (Scheffer et al., 2012). Intermediate tree covers are relatively rare, which leads to the hypothesis of the modes being stable states of boreal forests whereas the intermediate tree covers are unstable. Transitions between the different stable tree cover states might therefore be abrupt rather than gradual as assumed by most current dynamic vegetation models (Scheffer et al., 2012; Euskirchen et al., 2009). Hence, tipping points within the boreal forest might exist, even though the governing mechanisms are not well understood yet (Scheffer et al., 2012; Abis and Brovkin, 2017). Armstrong McKay et al. (2022) distinguish between southern dieback and northern expansion of boreal forests, which are both assumed to feature tipping points.

#### Southern Dieback

Global warming is thought to destabilize the southern edge of the boreal forest, creating a tipping point, after which abrupt dieback of the forest might occur (Armstrong McKay et al., 2022). Forest fires are expected to be a dominant driver of these dynamics (Scheffer et al.,

2012). As for tropical forests, flammability of the boreal forests is increasing with decreasing tree cover, leading to a runaway feedback toward a treeless state. This inverse proportionality between flammability and tree cover is caused by the increased amount of light that is able to penetrate more open forests which leads to the increased development of lower branches, serving as ladder fuels in the case of a fire, and by increased drying of understory mosses due to exposure to wind and light (Ryan, 2002). Additional drivers of boreal forest collapse include insect outbreaks, windfall, and browsing (Scheffer et al., 2012).

In their extensive literature review, Armstrong McKay et al. (2022) classify abrupt dieback of boreal forests (BORF) as a regional impact tipping element (medium confidence) with a threshold temperature of 4°C (1.4 to 5°C) (low confidence), occurring on a timescale of 100 years (minimum 50 years) (low confidence). They expect 52 GtC to be emitted by partial (50%) dieback of boreal forests. However, counteracting biogeophysical effects such as increasing albedo would lead to a negative feedback on GMST of −0.18°C (medium confidence).

**Northern Expansion**

At the northern edge of boreal forests, low temperatures and permafrost soils are limiting factors of tree growth. However, thawing of permafrost soils and a lengthening of the growing season due to global warming are expected to enable initial tree growth in these regions according to Scheffer et al. (2012). They further assume that via a decrease in albedo and an increase in wildfire frequency, trees would then increase the heat input to soils, resulting in a positive feedback causing abrupt forestation of former tundra regions.

Northern expansion of boreal forest (TUND) is thus classified as a regional impact TE (medium confidence) with a threshold temperature of 4°C (1.5 to 7.2°C) (low confidence) and a timescale of 100 years (minimum 40 years) (low confidence) (Armstrong McKay et al., 2022). The associated carbon uptake is estimated to be 6 GtC with counteracting biogeophysical effects such as albedo decrease and enhanced evapotranspiration, leading to a total feedback of +0.14°C on GMST (low confidence). It must be noted that these estimates do not include carbon released from thawing permafrost within this region.

Given the impact estimates by Armstrong McKay et al. (2022), northern expansion of boreal forests would nearly balance their southern dieback in therms of GMST increase, even though there is an emission gap of 46 GtC. The IPCC suggest, that this difference between carbon emissions from southern dieback of boreal forests and sequestered carbon from their northern expansion is approximately zero (Canadell et al., 2021).

### 1.2.4 Sahel and West African Monsoon

The Sahel region lies between the southern edge of the Sahara and the humid savanna woodland at roughly 10°N, and spans from the coasts of Mauritania and Senegal to the western parts of the Sudan (Nicholson, 2018). The Sahel is characterized by a semi-arid climate, allowing for the growth of grasslands, shrubs, and small trees. Even though it is home to some large cities such as Dakar and Bamako, most of the population lives in rural areas, practising agriculture. Hence, they strongly depend on the local climate.

The climate and hydrology of the Sahel region are primarily governed by the West African monsoon (WAM) system (Pausata et al., 2020). The WAM is broadly characterized by moist south-westerly winds transporting moisture from the ocean to the land during the boreal summer and dry north-easterly winds during the boreal winter. Especially between mid-July and September, the rainfall peak is established in the Sahel region (Thorncroft et al., 2011). Like other monsoon systems, the WAM is driven by the thermodynamic contrast between the land (Sahara and Sahel) and the sea (Tropical Atlantic) (Pausata et al., 2020).

Changes in the intensity of the WAM had severe impacts on the Saharan and Sahel hydroclimate in the past. The Saharan desert has experienced over 230 wet periods with a more vegetated landscape called green Sahara periods (GSPs) in the past eight million years, associated with a stronger WAM (Larrasoaña et al., 2013). During those periods, the increased WAM led to more intense summer rainfalls in the Sahel and the Sahara, enabling the northward migration of vegetation into the desert (Pausata et al., 2020). The GSPs were initially triggered by enhanced solar radiation due to the variations in the Earth's orbital parameters, with a number of feedbacks amplifying this effect, leading to an abrupt onset of the GSPs (Pausata et al., 2020). The most prominent feedbacks in this regard are associated with an increase in albedo and a decrease in dust-emissions due to enhanced vegetation. Both processes lead to increased radiative forcing over the newly greened land areas, enhancing the monsoonal circulation (Gaetani et al., 2017).

Although the increased long-wave radiative forcing due to the emission of anthropogenic GHGs is qualitatively different from the increase in solar radiation triggering GSPs in the past, evidence exists that abrupt greening of the Sahara and the Sahel might also happen under continued global warming. In general, global climate models from CMIP5 and CMIP6 and the regional downscaling model CORDEX predict a strengthening of the WAM, causing wetting and northward expansion of the central and eastern Sahel (Dosio et al., 2021). The increased precipitation in those areas allows for a self-amplifying greening, as found by regional dynamic vegetation models (Erfanian et al., 2016).

Given the evidence from paleoclimatic records and modelling studies, Armstrong McKay

et al. (2022) classify the Sahel vegetation and WAM (SAHL) as a regional impact TE (low confidence) with abrupt wetting and greening happening at a threshold of 2.8°C (2 to 3.5°C) (low confidence) over a timescale of 50 years (10 to 500 years) (low confidence).

### 1.2.5 Low-Latitude Coral Reefs

Reef-building corals only exist within a narrow range of environmental conditions occurring in tropical coastal areas, characterized by shallow, alkaline waters and abundant sunlight (Frieler et al., 2013). Globally, nearly 500 million people depend on coral reefs for food, coastal protection, cultural items, and tourism income, with approximately 30 million of the poorest people depending entirely on coral reefs for food as stated by Wilkinson, C. (2004), who furthermore explain, that coral reefs significantly contribute to biodiversity by providing habitat to over a million species.

Corals depend on the symbiosis with photosynthetic dinoflagellates, where inorganic waste metabolites from the coral are exchanged for organic nutrients from dinoflagellate photosynthesis (Stat et al., 2008). Rising oceanic temperatures together with ocean-acidification caused by anthropogenic GHGs lead to the sudden elimination of the dinoflagellates, which, if the symbiosis does not recover, causes the dead of the concerned coral (Douglas, 2003). This process is referred to as "coral bleaching" since the colour of the corals results from the dinoflagellates who expose the white calcium carbonate skeleton of the coral once they die.

Coral reefs are one of the most vulnerable ecosystems to climate change. Since the 1950s, the global coverage of living corals has declined by half, catches of coral-reef-associated fishes have declined despite increasing fishing efforts, and the coral-reef-associated biodiversity has declined by at least 63% (Eddy et al., 2021). Model studies suggest that coral reefs will further decline under continued anthropogenic warming (Frieler et al., 2013; Hughes et al., 2017).

Given that coral bleaching happens regionally synchronized (as seen for the Great Barrier Reef), Armstrong McKay et al. (2022) classify warm-water coral reefs (REEF) as a regional impact TE (high confidence) with an estimated threshold temperature of 1.5°C (1 to 2°C) (high confidence), occurring over a timescale of $\sim 10$ years (medium confidence).

### 1.2.6 Greenland Ice Sheet

The Greenland ice sheet (GRIS) covers most of Greenland and is the globally second-biggest ice sheet after the Antarctic ice sheet, which together contain about 99% of the Earth's freshwater ice (Elias, 2021). Nearly all of GRIS (98%) is grounded with a bed above sea level

and would therefore directly contribute to sea level rise if melted, which results in a total sea level equivalent (SLE) (the amount global mean sea level (GMSL) would rise in case of total melt) of $7.42 \pm 0.05$ m (Morlighem et al., 2017).

The rate of change of GRIS is described by its mass balance (MB) which is given by the difference in surface mass balance (SMB) and solid ice discharge across the grounding line ($D$) (Noël et al., 2021):

$$MB = SMB - D. \tag{1}$$

The SMB, in turn, is defined as the difference between accumulation from precipitation (snow and rain) and mass loss from ablation (sublimation, drifting snow erosion and runoff) (Khan et al., 2015).

The two main positive feedbacks that might produce a tipping point after which irreversible loss of the GRIS occurs, are the elevation and the albedo-climate feedback (Robinson et al., 2012). The elevation feedback arises due to thinning of the ice sheet, lowering the ice surface and exposing it to higher temperatures, which leads to increased surface melt and therefore increased thinning. As ice sheets cover less of the land surface which typically has a lower albedo, local warming increases, causing further ice sheet melt, which is termed the albedo-climate feedback. Furthermore, the marine terminating outlet glaciers of the GRIS might be affected by marine ice sheet instability (MISI) (Khan et al., 2020) and marine ice cliff instability (MICI) (Jakobsson et al., 2018). In brief, MISI can be explained by the observation that ice flux increases with ice thickness, hence, if the ice sheet thins, becomes afloat and the grounding line retreats inland towards higher ice thickness, which is increasing towards the land interior if the ice sheet bed is retrograde sloped, ice flux towards the ocean increases and the grounding line retreats further (Pattyn, 2018). Therefore, grounding lines located on retrograde slopes, i.e., a terrain that deepens toward the land interior, are unstable and can result in a positive feedback of self-reinforcing ice-loss. MICI is associated with a collapse of buttressing ice shelves connected to the glacier. If those ice shelves collapse due to processes such as sub-shelf melting or hydro-fracturing, the ice cliff of the glacier might become unstable and fall down if higher than $\sim 90$ m above sea level (Pattyn, 2018). As outlet glaciers are retreating with global warming until GRIS becomes fully grounded, which might happen within a few centuries under high emission scenarios (Aschwanden et al., 2019), the surface mass balance-elevation feedback will be crucial as the MB is determined solely by SMB with $D = 0$ (Noël et al., 2021).

GRIS is characterized by a negative MB since the 1980s, with on average $51 \pm 17$ Gt yr$^{-1}$ being lost during the 1980-1990 period, which has increased to $286 \pm 20$ Gt yr$^{-1}$ until the 2010-2018 period (Mouginot et al., 2019). Part of this development can be explained by a

step-increase in $D$ during the early 2000s, which corresponds to widespread retreat of marine terminating glaciers (King et al., 2020). For some major glaciers, this retreat can be linked to MISI (Khan et al., 2020) or MICI (Jakobsson et al., 2018). Ice loss from GRIS since 1972 caused GMSL rise of $13.7 \pm 1.1$ mm, making it the largest single contributor to sea level rise (Mouginot et al., 2019; King et al., 2020).

GRIS will continue to shrink throughout the next millennium. Even under the low emission scenario RCP2.6, an additional $5 - 19$ cm sea level rise is expected from GRIS in 2100 relative to 2008, increasing to $59 - 191$ cm in 3000 (Aschwanden et al., 2019). Under the high emission scenario RCP8.5, those numbers increase to $14 - 33$ cm and $538 - 728$ cm respectively, underlining that GRIS loss will happen on a millennial timescale. Threshold temperatures after which GRIS loss becomes irreversible have been found in multiple modelling studies (Van Breedam et al., 2020; Robinson et al., 2012). Additional evidence for tipping dynamics of the GRIS comes from paleorecords which indicate that Greenland has been ice free during the interglacial period marine isotope stage 11 (Christ et al., 2021).

As GMSL rise from GRIS collapse would impact coastal regions globally, Armstrong McKay et al. (2022) categorize GRIS as a global core TE (high confidence) with a threshold temperature of 1.5°C (0.8 to 3°C) (high confidence), occurring over a timescale of 10 kyr (1 to 15 kyr) (medium confidence).

### 1.2.7 West Antarctic Ice Sheet

The West Antarctic ice sheet (WAIS) stores a SLE of 4.3 m, of which $\sim 80\%$ is attributed to ice grounded with a bed below sea level (Fretwell et al., 2013). Therefore, and since it is attached to floating ice shelves at the grounding line, it is classified as a marine ice sheet (Arthern and Williams, 2017).

For the MB of WAIS, eq. 1 holds as well as for GRIS, however, expected ice loss from WAIS due to global warming is associated with a high $D$ rather than a negative SMB. This is due to the fact that vast amounts of WAIS are grounded on retrograde slopes below sea level, which can cause MISI (Weertman, 1974; Schoof, 2007). Furthermore, MICI might cause abrupt retreat of WAIS marine terminating glaciers and has the potential to trigger MISI (Pattyn, 2018). However, the significance of this process for future ice loss from the WAIS is disputed (Edwards et al., 2019).

The WAIS is already loosing mass. Between 1992 and 2017 it has contributed $5.7 \pm 0.8$ mm to GMSL rise (Shepherd et al., 2019). Glaciers draining the Amundsen sea sector of the WAIS that are grounded on retrograde slopes are already undergoing MISI and retreating,

and no major bed obstacles that could prevent further MISI are found (Rignot et al., 2014).

The future development of WAIS introduces deep uncertainties to the projections of GMSL. Under RCP8.5, depending on the degree of its disintegration, WAIS could add between zero (no collapse) up to 3.3 m (full collapse) to GMSL until 2100 (Bakker et al., 2017). Most model studies indicate long-term partial collapse of WAIS, even under present warming levels or slightly above (Arthern and Williams, 2017; Garbe et al., 2020). This hypothesis is also supported by paleoclimatic records, which show partial loss of WAIS during the last interglacial (Turney et al., 2020).

Given the global impacts of GMSL rise due to potential WAIS collapse, Armstrong McKay et al. (2022) classify WAIS as a global core TE (high confidence), associated with a threshold temperature of 1.5°C (1.0 to 3.0°C) (high confidence), occurring over a timescale of 2 kyr (0.5 to 13 kyr) (medium confidence).

### 1.2.8 East Antarctic Ice Sheet

The East Antarctic ice sheet (EAIS) is by far the largest ice sheet globally, as it stores a SLE of 53.3 m, with most of the ice of being grounded with a bed above sea level (64% of SLE) (Fretwell et al., 2013). The marine part of the EAIS mainly consists of three subglacial basins, which are discussed below. Here, we focus on the "terrestrial" parts of the EAIS grounded on land above sea level, which are referred to as EAIS in the following, consistent with Armstrong McKay et al. (2022).

Due to the terrestrial nature of the EAIS, the dominant positive feedbacks that might constitute a tipping point for EAIS collapse are the elevation and the albedo feedback (Sec. 1.2.6) (Robinson et al., 2012; Garbe et al., 2020).

Recent changes of the EAIS mass remain uncertain, with negative and positive trends being supported by observations (Stokes et al., 2022). On the one hand, Wang et al. (2021) and Shepherd et al. (2019) report that the EAIS including the subglacial basins is gaining mass in recent decades which can be related to extreme snowfall events over EAIS, causing a positive SMB (Boening et al., 2012). On the other hand, Rignot et al. (2019) observe a negative mass balance of the EAIS including subglacial basins, yielding GMSL rise of $4.4 \pm 0.9$ mm between 1979 and 2017.

Paleorecords and models indicate a strong hysteresis effect of the EAIS, where multiple states of the ice sheet are possible under the same environmental boundary conditions, with the ice sheet becoming stable once it reaches continental scales (Garbe et al., 2020; Gasson et al., 2016). This stability explains the observation from paleorecords that the EAIS has only

partially melted partly during the Mid-Miocene climate optimum (17.0 – 14.8 Myr BP) with atmospheric $CO_2$ concentrations around 600 to 800 ppm (Stokes et al., 2022). However, model results show that the amount of committed ice loss from the EAIS significantly increases beyond 6°C, mainly due to the elevation feedback (Garbe et al., 2020).

Due to the massive impact EAIS collapse would have on the GMSL, Armstrong McKay et al. (2022) classify it as a global core TE (medium confidence) with a threshold temperature of 7.5°C (5 to 10°C), occurring over a timescale $\geq$ 10 ky (medium confidence).

### 1.2.9 East Antarctic Subglacial Basins

A major fraction of the 19.2 m of SLE stored in marine parts of the EAIS with a bed below sea level can be attributed to the three main East Antarctic subglacial basins (EASBs): the Wilkes, the Aurora, and the Recovery basin (Fretwell et al., 2013; Stokes et al., 2022).

As for the WAIS, the beds of the EASBs are often retrograde sloped, making them vulnerable to MISI (Mengel and Levermann, 2014). Additionally, MICI might occur once buttressing ice shelves disappear (DeConto et al., 2021).

Even though the mass change of the EAIS including the EASBs remains somewhat uncertain (Sec. 1.2.8), the EASBs considered individually are already loosing mass (Stokes et al., 2022). The mass loss from the East Antarctic region reported by Rignot et al. (2019) causing GMSL rise of $4.4 \pm 0.9$ mm between 1979 and 2017 is mainly produced by ice loss from the Wilkes subglacial basin.

Paleorecords indicate ice retreat in the Wilkes subglacial basin during the interglacial intervals of the late Pleistocene (e.g., 130 – 80 kyr BP for the last interglacial) when Antarctic air temperatures were at least two degrees higher than pre-industrial temperatures over 2500 years or more (Wilson et al., 2018). For the future development of EASBs, coupled ice-sheet/ice-shelf model experiments predict that substantial ice loss from the Wilkes and the Aurora subglacial basin will unfold over the next three millennia under RCP8.5 (Golledge et al., 2015).

Given that the collapse of EASBs could cause sea level rise with the same order of magnitude as GRIS or WAIS, Armstrong McKay et al. (2022) classify EASBs as a global core TE (high confidence) with a threshold temperature of 3°C (2 to 6°C) (medium confidence), unfolding over a timescale of 2 kyr (500 y to 10 kyr) (medium confidence).

### 1.2.10 Arctic Sea Ice

The Arctic Ocean is covered by a layer of sea ice which typically reaches its maximum extent in March (mean of $15.43 \cdot 10^6$ km$^2$ for the 1981-2010 period), melts throughout summer, and reaches the minimum extent in September (mean of $6.41 \cdot 10^6$ km$^2$ for the 1981-2010 period) (Stroeve and Notz, 2018). Arctic sea ice plays a crucial role in regulating the exchange of momentum, heat, and moisture between the atmosphere and the polar oceans and impacts the ocean salinity. Furthermore, Arctic sea ice provides a habitat for many adapted species, from ice algae to polar bears, and regulates local biochemical cycles by influencing the transfer of radiation, gas, and fluids between the atmosphere and the ocean (Meier et al., 2014). Arctic sea ice also plays a major role in the life of local communities who depend on sea ice e.g., for transportation and hunting, with about four million people living in the Arctic, of whom $\sim$10% are indigenous (Arctic Council, 2023).

The most important positive feedback associated with abrupt sea ice loss is the ice-albedo feedback (e.g., Hankel and Tziperman, 2021). Due to initially declining sea ice extent in summer, the ocean absorbs more SW radiation as high-albedo sea ice is gone and heats up with the heat being released to the atmosphere in autumn and winter, prohibiting sea ice growth. The ice-albedo feedback is assumed to be one of the reasons for the Arctic amplification of global warming (Serreze et al., 2009).

Arctic sea ice loss is already evident, with 10.6% of winter sea ice extent and 45.2% of summer sea ice extent lost in 2018 compared to the 1979-1989 period (Stroeve and Notz, 2018).

#### Arctic Winter Sea Ice

While the retreat of Arctic summer sea ice is assumed to happen linearly (Notz, 2009), some GCMs predict an abrupt decrease in Arctic winter sea ice (AWSI) (Drijfhout et al., 2015; Hezel et al., 2014), which points towards a tipping point for AWSI loss.

Several positive feedbacks have been discussed which could explain those tipping dynamics, mostly more specified versions of the ice-albedo feedback explained above. One mechanism that is assumed to play a major role is the formation of convective clouds during autumn and winter due to heat and moisture release from the ocean to the lower atmosphere, which leads to an increased downward reflection of LW radiation, prohibiting sea ice growth (Arnold et al., 2014). However, the differences in AWSI decline between GCMs can also be explained without convective clouds but with different amounts of clear sky downward LW radiation in autumn and winter due to a warmer and more moist lower atmosphere (Hankel and Tziperman, 2021).

While there is agreement between GCMs from CMIP6 that AWSI will decline in response to

anthropogenic GHG emissions, the magnitude and timing of this decline is still uncertain (Notz and Community, 2020). Under RCP8.5, GCMs predict that AWSI might disappear completely before 2300 (Hankel and Tziperman, 2021).

As AWSI impacts the Earth system beyond the Arctic, Armstrong McKay et al. (2022) classify it as a global core TE (medium confidence) with a threshold temperature of 6.3°C (4.5 to 8.7°C) (high confidence) and a timescale of 20 years (10 to 100 years) (high confidence).

**Barents Sea Winter Ice**

The abrupt loss of Barents Sea winter ice (BARI) is considered to be a subcase of AWSI collapse (Armstrong McKay et al., 2022). With a mean extent of $961 \cdot 10^3$ km$^2$ in March during the 1979 – 1989 period (calculated from numbers in Tab. 2 of Stroeve and Notz (2018)), BARI only makes up for about 6% of the total AWSI. However, loss of BARI would influence for European weather and potentially the AMOC (Smedsrud et al., 2013).

Like AWSI, BARI is already in decline. However, BARI loss is happening much faster than AWSI loss: 47.2% of the average BARI extent between 1979 and 1989 has been lost in 2018, compared to only 10.6% for AWSI (Stroeve and Notz, 2018).

The rapid decline of BARI in recent decades can be linked to increased inflow of warm Atlantic water into the Barents Sea that is self-reinforcing via atmospheric and oceanic positive feedbacks (Smedsrud et al., 2013).

Extrapolating the observed trend of BARI loss results in a year round ice-free Barents Sea between 2023 and 2036 (Onarheim and Årthun, 2017). However, BARI loss could also happen abruptly, as found in two CMIP5 models (Drijfhout et al., 2015).

Armstrong McKay et al. (2022) classify BARI as a regional impact TE (medium confidence) with a threshold temperature of 1.6°C (1.5 to 1.7°C) (low confidence) and a timescale of 25 years (low confidence).

### 1.2.11 Mountain Glaciers

About 8.9% of the global population lives in river basins that depend on mountain glacier (GLCR) discharge for at least 5% of the total river discharge in the peak-melt month (Schaner et al., 2012). The major share of this group lives in Asia (94%), some live in North and South America (4.5%) and the rest lives in Europe (1.5%). Glacier retreat due to global warming would negatively affect the freshwater availability within those river basins. Furthermore, a decrease of glacier discharge would also affect hydropower production, aquatic ecosystems

and sediment transport (Milner et al., 2017). Additionally, their meltwater adds to GMSL rise (Levermann et al., 2012).

Similar to ice sheets, the albedo-climate feedback could speed-up the retreat of GLCR, which in this case is further amplified by a decrease in snow precipitation and increased dust accumulation on the ice, both lowering the glacier albedo (Levermann et al., 2012).

Most glaciers are already loosing mass since the middle of the 17th century, with mass loss significantly accelerating since 1970 (Gulev et al., 2021), reaching the highest observed loss rates in recent decades with $267 \pm 16$ Gt yr$^{-1}$ being lost on average between 2000 and 2019 (Hugonnet et al., 2021). This means that even though glaciers only contain less than 1% of the global frozen freshwater (Radić and Hock, 2011), they have been a major driver of GMSL rise (Meier et al., 2007). Similar to ice sheets, glaciers are characterized by thermal inertia and therefore a lagged response to global warming, meaning that they are committed to further decline even if the warming levels would stabilize (Gulev et al., 2021).

The annual mean runoff from melting glaciers is typically described as a convex function of time, with the maximum being referred to as "peak water". Of 56 major global glacial basins, roughly half have already passed their peak water and nearly all other basins will follow within this century under RCP4.5 (Huss and Hock, 2018). Under RCP8.5, another 0.18 m (0.15 to 0.2 m) of GMSL rise is projected to be caused by melting glaciers until the end of the century (Fox-Kemper et al., 2021).

Given that GLCR loss is projected to happen synchronously over subcontinental scales with significant human impacts, Armstrong McKay et al. (2022) classify them as a regional impact TE (medium confidence) with a threshold temperature of 2°C (1.5 to 3°C) (medium confidence), occurring over a timescale of 200 years (50 years to 1 ky) (medium confidence).

### 1.2.12 Atlantic Meridional Overturning Circulation

Transporting water masses northward at the surface and southward at the bottom of the Atlantic Ocean, the Atlantic meridional overturning circulation (AMOC) is a key global circulation system (Boers, 2021). It influences the climate over the Atlantic and the adjacent landmasses. Northern Europe is a prominent example, which benefits from the relatively warm and wet climate caused by northward heat transport of the AMOC of $\sim 1$ PW at 30°N (Bryden and Imawaki, 2001). Due to its large scale impacts on the global climate, the AMOC is assumed to act as a mediator between other TEs and could therefore play a major role within tipping cascades.

In crude words, the two main drivers of the AMOC are wind-driven upwelling in the South

Atlantic Ocean and density driven deep convection in the Nordic Seas and Labrador Sea (Kuhlbrodt et al., 2007). The deep convection is to some degree self-sustained, as warm water masses transported northwards near the surface loose heat and freshwater along the way, resulting in cool and saline and hence dense water masses. Increased meltwater runoff from GRIS would lead to a freshening of surface water masses and hence a reducing of their density, which results in increased density stratification and could therefore prohibit deep convection and slow down the AMOC (Lohmann and Ditlevsen, 2021).

Abrupt transitions to warmer (Dansgaard-Oeschger events) and colder climates (Heinrich events) in the Northern Hemisphere during the last glacial period are associated with a strong and a weak or even non-existent AMOC respectively, indicating AMOC bistability (Rahmstorf, 2002; Brovkin et al., 2021).

Bistability of the AMOC has also been found in early box models (Stommel, 1961) and in some AOGCMs (Hawkins et al., 2011). This bistability is not found in most ESM (Liu et al., 2014), however, this might be due to model biases (Liu et al., 2017).

Evidence for the AMOC approaching a tipping point also comes from early warning indicators derived from recent observations, which suggest that the AMOC has evolved from stable conditions towards a tipping point over the course of the last century (Boers, 2021).

A shift from the current strong state of the AMOC to a weak state would have manifold impacts on the global climate. Europe would experience cooling and a shift of precipitation patterns, whereas the Antarctic region would warm (Jackson et al., 2015). Therefore, and due to the mediating role of the AMOC between other TEs, Armstrong McKay et al. (2022) classify the AMOC as a global core TE (medium confidence) with a threshold temperature of 4°C (1.4 to 8°C) (low confidence), occurring over a timescale of 50 years (15 to 300 years) (medium confidence).

### 1.2.13 North Atlantic Subpolar Gyre - Labrador and Irminger Sea Convection

The subpolar gyre (SPG) located south of Greenland is an integral part of the AMOC and comprises deep convection sites in the Labrador and Irminger Sea, where deep waters are formed (Buckley and Marshall, 2016). Shutting down this deep convection is assumed to be related to a weak or even collapsed SPG and hence reduced northward heat transport within the North Atlantic, leading to regional cooling (Caesar et al., 2018).

Cyclonic wind stress at the surface of the North Atlantic and buoyancy forcing is causing the cyclonic circulation of the SPG with horizontally diverging currents in the middle of the gyre, producing upward dooming isopycnals which are a preconditioning for deep convection

(Sgubin et al., 2017). Since deep convection in turn causes higher mixed layer depths, a strong SPG leads to increased mixed layer depths. As mixed layer depth affects the density structure and thus the strength of the SPG, positive feedbacks between deep convection and the SPG can arise, causing potential instability of the system (Sgubin et al., 2017; Born and Mignot, 2012).

Contrary to the global warming trend, the region over the SPG has cooled in recent decades (Keil et al., 2020), which is often linked to a weakening of the SPG (Swingedouw et al., 2021). Weakening of the SPG is also predicted by some CMIP5 and CMIP6 models, even though it generally remains a rare feature of them (Sgubin et al., 2017; Swingedouw et al., 2021).

Even though SPG collapse would probably affect the AMOC, Armstrong McKay et al. (2022) consider it to be a distinct TE as it is governed by other feedback mechanisms and could collapse much faster than the AMOC. The North Atlantic subpolar gyre with Labrador and Irminger sea convection (LABC) is therefore classified as a global core tipping element (medium confidence) with a threshold temperature of 1.8°C (1.1 to 3.8°C) (high confidence), occurring over a timescale of 10 years (5 to 50 years) (high confidence).

## 1.3 Carbon Emissions from Carbon Tipping Elements

We limit our analysis of the impacts from carbon TEs to PFAT, PFTP and AMAZ. PFGT is not considered, since it is classified as a threshold-free feedback by Armstrong McKay et al. (2022) and does therefore not match the definition of a TE, which needs to include a clear tipping point. Furthermore, a conceptual approach to model PFGT might not be appropriate since more sophisticated modelling techniques such as ESMs and land-surface models exist (e.g., Arora et al., 2020; Meinshausen et al., 2020). BORF and TUND are also not included in our analysis, as the carbon emissions from BORF are assumed to be balanced by TUND and invasion of temperate forests (Canadell et al., 2021). Therefore, we refer to PFAT, PFTP, and AMAZ if we speak about carbon TEs hereafter. The estimates of carbon emissions from the carbon TEs from Armstrong McKay et al. (2022) given in the sections above are informed by numerous studies, which we explore in this section to understand the rationale behind those estimates our analysis is largely based on.

### 1.3.1 Abrupt Permafrost Thaw

Since PFAT is highly dependent on small-scale features, e.g., topography, it is not included in current ESMs, and it remains challenging to quantify the associated carbon emissions (Turetsky et al., 2019). Current studies rely on simplistic inventory models (Turetsky et

| Category | | Proposed Climate Tipping Element (& Tipping Point) | Threshold (°C) Est. | Min | Max | Timescale (years) Est. | Min | Max | Max. Impact (GtC) |
|---|---|---|---|---|---|---|---|---|---|
| Global core tipping elements | PFTP | Boreal Permafrost (collapse) | 4.0 | 3.0 | 6.0 | 50 | 10 | 300 | 125 - 250 |
| | GrIS | Greenland Ice Sheet (collapse) | 1.5 | 0.8 | 3.0 | 10k | 1k | 15k | |
| | WAIS | West Antarctic Ice Sheet (collapse) | 1.5 | 1.0 | 3.0 | 2k | 500 | 13k | |
| | EAIS | East Antarctic Ice Sheet (collapse) | 7.5 | 5.0 | 10.0 | ? | 10k | ? | |
| | EASB | East Antarctic Subglacial Basin (collapse) | 3.0 | 2.0 | 6.0 | 2k | 500 | 10k | |
| | AWSI | Arctic Winter Sea Ice (collapse) | 6.3 | 4.5 | 8.7 | 20 | 10 | 100 | |
| | AMAZ | Amazon Rainforest (dieback) | 3.5 | 2.0 | 6.0 | 100 | 50 | 200 | Partial: 30 Total: 75 |
| | AMOC | Atlantic M. O. Circulation (collapse) | 4.0 | 1.4 | 8.0 | 50 | 15 | 300 | |
| | LABC | Labrador- Irminger Seas SPG Convection (collapse) | 1.8 | 1.1 | 3.8 | 10 | 5 | 50 | |
| Regional impact tipping elements | PFAT | Boreal Permafrost (abrupt thaw) | 1.5 | 1.0 | 2.3 | 200 | 100 | 300 | Adds 25-75% to gradual thaw: = 5-15 GtC per °C @2100; 12.5-37.5 GtC per °C @2300, up to max. 60-195 GtC |
| | BARI | Barents Sea Ice (abrupt loss) | 1.6 | 1.5 | 1.7 | 25 | ? | ? | |
| | GLCR | Mountain Glaciers (loss) | 2.0 | 1.5 | 3.0 | 200 | 50 | 1k | |
| | REEF | Low-latitude Coral Reefs (die-off) | 1.5 | 1.0 | 2.0 | 10 | - | - | |
| | SAHL | Sahel and W. African Monsoon (greening) | 2.8 | 2.0 | 3.5 | 50 | 10 | 500 | |
| | BORF | Boreal Forest (southern dieback) | 4.0 | 1.4 | 5.0 | 100 | 50 | ? | 52 GtC / -0.18°C |
| | TUND | Boreal Forest (northern expansion) | 4.0 | 1.5 | 7.2 | 100 | 40 | ? | -6 GtC / +0.14°C |
| Threshold-free nonlinear Feedbacks | PFGT | Boreal Permafrost (gradual thaw) | 1.5 | 1.0 | 2.4 | 300 | 100 | 300< | 20 GtC per °C @2100; 50 GtC per °C @2300, up to max 260 GtC |

**Table 1:** Category, threshold, timescale, and impact of the TEs, reproduced from Armstrong McKay et al. (2022). Colours of the second left column represent the Earth system domain of the tipping point (blue = cryosphere, green = biosphere, orange = ocean/atmosphere). All other colours represent confidence, with green = high confidence, yellow = medium confidence and red = low confidence.

al., 2020), expert elicitations (Schuur et al., 2015) or observation-based permafrost models (Schneider von Deimling et al., 2015) and suggest that abrupt thaw can up to double carbon emissions from PFGT (Turetsky et al., 2019). This estimate is partly due to the high share of $CH_4$ emissions from anaerobic respiration, accounting for $\sim 20\%$ of the total carbon emissions (Turetsky et al., 2020).

The expert judgment of cumulative carbon emissions from permafrost in 2100 under RCP8.5 in Schuur et al. (2015) is raised from $\sim 92\,\mathrm{GtC}$ to $130 - 160\,\mathrm{GtC}$ if abrupt thawing processes are included, giving an amplification of 58% (41 to 74%) of PFGT carbon emissions by PFAT. There seems to be consensus that PFAT is simply amplifying PFGT carbon emissions, meaning that PFAT carbon emissions are also linearly responding to global warming (Turetsky et al., 2020; Turetsky et al., 2019).

Relying on this limited set of studies, Armstrong McKay et al. (2022) assume that PFAT is amplifying carbon emissions from PFGT by 50% (25 to 75%).

### 1.3.2 Permafrost Collapse

Like PFAT, PFTP is also not represented by current ESMs due to the complexity involved with it (Schneider von Deimling et al., 2015). The compost bomb instability hypothesis mainly rests on the mathematical analysis of Luke and Cox (2011) and has been tested only in a few model studies.

One of them has been conducted by Khvorostyanov et al. (2008), who found that 285 GtC can be released from the Yedoma region between 2300 and 2400 if PFTP is triggered with mean emission rates of $2 - 2.8\ \mathrm{GtC\ yr^{-1}}$, using a permafrost model that explicitly accounts for microbial heat production. This is significantly higher than the 22.8 GtC of $CO_2$ emissions and 294 $\mathrm{MtCH_4}$ of $CH_4$ emissions giving total carbon emissions of 23 GtC that are released from Yedoma deposits until 2300 under RCP8.5 reported by Schneider von Deimling et al. (2015), who rely on a 2D model informed by current permafrost observations. This study also suggests that $CH_4$ emissions amplify the carbon emissions warming potential from Yedoma deposits by 40%, which is included within the uncertainty range of additional warming caused by $CH_4$ emissions from PFGT of $35 - 48\%$, for which 2.3% of the carbon is emitted as $CH_4$ (Schuur et al., 2015). Therefore, we assume that 2.3% of the carbon from PFTP is emitted as methane.

Armstrong McKay et al. (2022) also expect compost bomb instabilities to occur in the 2.2 million $\mathrm{km^2}$ of permafrost soils for which abrupt drying beyond 4°C of global warming is expected (Teufel and Sushama, 2019), adding to the carbon emissions of PFTP.

For their estimate of carbon emissions from PFTP, Armstrong McKay et al. (2022) expect that $25 - 50\%$ of the carbon from the Yedoma region and from the 2.2 million $km^2$ of permafrost soils subject to abrupt drying beyond 4°C would be released, giving total emissions of 125 to 250 GtC. However, due to the limited evidence this estimate is based on, PFTP estimates are only given with low confidence, whereas impact estimates of PFGT and PFAT are given with medium confidence (Tab. 1).

### 1.3.3 Amazon Rainforest

The main tool to predict carbon emissions from AMAZ are dynamic vegetation models, which feature different dynamic vegetation carbon stocks. Dynamic vegetation models can either be part of ESMs (Cox et al., 2000) or coupled to GCMs (Nobre et al., 1991) to explore the response of AMAZ to global warming. A common critique of most dynamic vegetation models is the under-representation of natural and anthropogenic forest fires, with only four CMIP6 models explicitly representing fire (Sanderson and Fisher, 2020). Therefore, CMIP6 models might be undersensitive to AMAZ dieback. Furthermore, the chance for AMAZ dieback is increased if anthropogenic deforestation is considered (Nobre et al., 2016). However, this effect is neither accounted for in the modelling studies introduced in the following, nor included in the estimates from Armstrong McKay et al. (2022) and therefore also not in our analysis.

One of the first modelling studies which found that loss of AMAZ might be irreversible is Nobre et al. (1991). Using a dynamic vegetation model coupled to a GCM, they found that total deforestation of the AMAZ would lead to significantly increased mean surface temperatures and a decrease in evapotranspiration and precipitation. In the south-eastern region of the AMAZ, this was found to lead to climatic conditions in which a rainforest could not exist any more, i.e., an irreversible loss of the rainforest. The first ESM featuring a dynamic vegetation model which allows for changes in vegetation type and carbon pools within the vegetation and the soil was used to investigate the response of the Amazon rainforest to global warming (Cox et al., 2000; Cox et al., 2004). It predicts that under a "business as usual" scenario, over the 21st century Amazonian temperatures would rise by more than 9 °C together with a drop in rainfall by 64%, which leads to abrupt dieback of the rainforest with 78% (35.6 GtC) of AMAZ vegetation carbon and 72% (14.3 GtC) of AMAZ soil carbon being lost until 2100.

More recent studies show that the extreme dieback of the Amazon rainforest found by Cox et al. (2004) is most likely unrealistic, since the model sensitivity of tropical land carbon to climate change is too high compared to a constraint emerging from the measured sensitivity

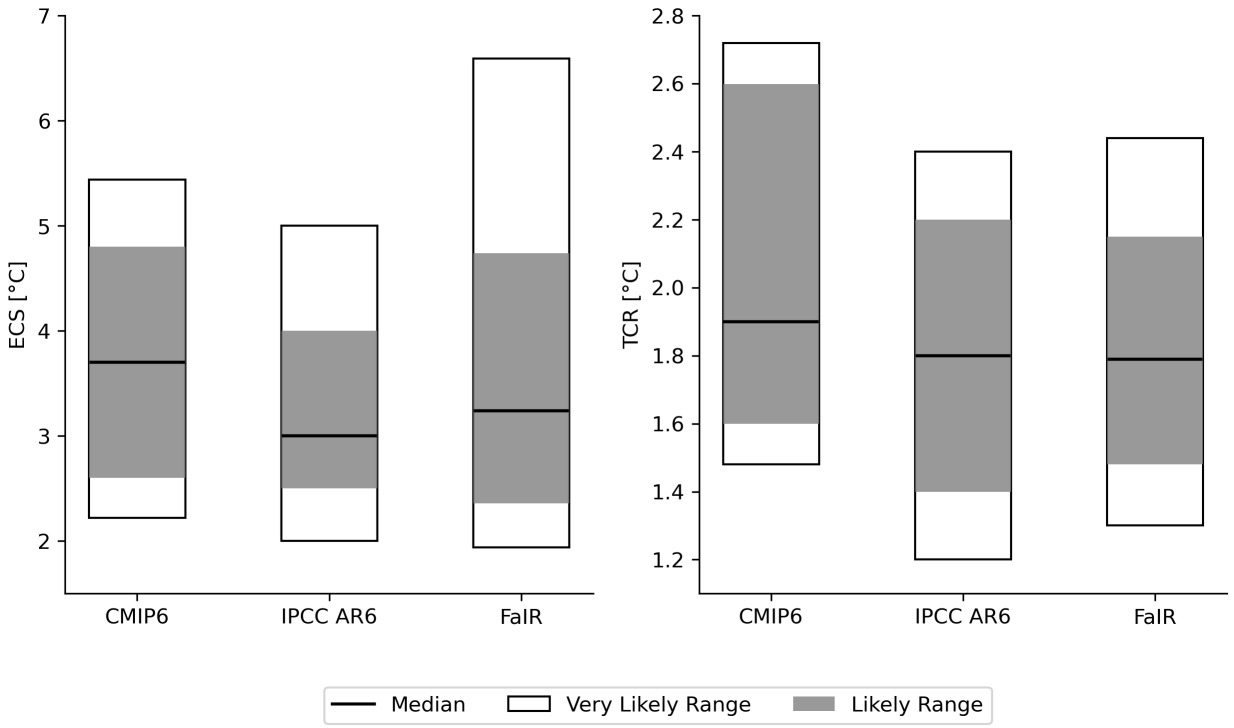


**Figure 1:** Likely range (66%), very likely range (90%) and median of the ECS and the TCR from CMIP6 models (Meehl et al., 2020), the sixth report of the IPCC (Forster et al., 2021) and the constrained parameter ensemble of FaIR (Leach et al., 2021).

of the annual growth rate of atmospheric $CO_2$ to tropical temperature anomalies (Cox et al., 2013; Wenzel et al., 2014). In the most recent ESMs containing dynamical vegetation which have been included in CMIP6, localized abrupt dieback of the Amazon rainforest was found in five out of seven models (Parry et al., 2022) under the 1pctCO2 run. However, these dieback events do not lead to a significant reduction of carbon stored within the forest.

The estimated carbon emissions from AMAZ dieback by Armstrong McKay et al. (2022) are based on the assumption that AMAZ would be degraded to secondary forest or savanna in case of tipping. This degradation is assumed to affect between 40% and 100% of the AMAZ region, with the lower bound defined by the currently bistable area of AMAZ found by Staal et al. (2020). Based on estimates of the carbon storage within AMAZ compared to degraded forest or savanna, this yields carbon emissions between 30 GtC and 75 GtC which only consist of $CO_2$.

## 1.4 Our Model Approach

To calculate whether a TE is triggered under a specific emission scenario, anthropogenic GHG emissions need to be mapped to GMST, which can then be used to infer whether the TE is

triggered by comparing GMST to the threshold temperature of the TE. To make a statement about the probability of triggering a TE, several uncertainties need to be accounted for along this calculation chain.

The uncertainty in long-term projections of GMST (climate projections) by GCMs can be partitioned into three types of uncertainty: internal variability, model uncertainty and scenario uncertainty (Hawkins and Sutton, 2009). Internal variability arises from the chaotic nature of the climate system, causing uncertainty that stays constant over time. Model uncertainty is caused by the limited prediction skill of GCMs due to incomplete knowledge of the climate system and computational limitations. Scenario uncertainty stems from incomplete knowledge of future GHG emissions. At the beginning of a model run, the total uncertainty in GMST is manly comprised by internal variability and model uncertainty (Lehner et al., 2020). Throughout the model period, the relative contribution of internal variability to total uncertainty of vanishes, becoming negligible after roughly 40 years of model lead time as model uncertainty and scenario uncertainty are increasing. Since the increase in scenario uncertainty is higher than the increase in model uncertainty, the scenario uncertainty is making up for the major share of total uncertainty towards the end of the model period, causing roughly 60% of the total uncertainty after 80 years of model lead time.

We incorporate the scenario uncertainty by performing our analysis under five different emission scenarios. Hereby, we rely on the shared socioeconomic pathways (SSPs) used in CMIP6 (O'Neill et al., 2016). Each SSP describes an alternative possible evolution of human society in absence of climate change or climate policy, and they are summarized by the names sustainability, middle of the road, regional rivalry, inequality and fossil-fuel-development (abbreviated by numbers from 1 to 5 in this order) (O'Neill et al., 2015). Each of these scenarios has been shown to possibly lead to certain additional radiative forcings at the end of the century (Riahi et al., 2016). The combinations of the SSP and the additional radiative forcing at the end of the century that is possible under the respective SSP give the combined names of the scenarios, with the first number encoding the SSP and the last numbers standing for the quantity of additional radiative forcing at the end of the century in $\mathrm{Wm}^{-2}$. We use the five high priority "Tier1" scenarios SSP1-1.9, SSP1-2.6, SSP2-4.5, SSP3-7.0, and SSP5-8.5.

To map anthropogenic GHG emissions from the SSPs to GMST until the year 2500, we use the second version of the Finite amplitude Impulse Response model (FaIR), a 0D reduced complexity climate model developed by Leach et al. (2021).

Since it only represents globally averaged variables, FaIR is unable to reproduce the internal variability of the climate system. However, since our model period is around 500 years long and uncertainty from internal variability is becoming negligible after 80 years of model lead

time compared to scenario uncertainty and model uncertainty (Lehner et al., 2020), we do not regard this a major shortcoming of our model approach.

The model uncertainty of climate models can be specified by comparing the "forced response", i.e., the response to a given emission scenario, among several climate models (Lehner et al., 2020). Common metrics to describe the forced response of climate models are the equilibrium climate sensitivity (ECS) and the transient climate response (TCR). ECS is defined as the long-term GMST increase arising from a doubling of atmospheric $CO_2$ concentrations compared to pre-industrial levels, whereas TCR is defined as the GMST increase at year 70 when atmospheric $CO_2$ concentration is doubled under a 1% per year increase scenario (Forster et al., 2021). FaIR is able to represent model uncertainty by making use of a parameter ensemble informed by CMIP6 models and constrained with the observed level and trend of anthropogenic warming (Sec. 2.2.4). While the range of TCR from the constrained parameter ensemble of FaIR is in good agreement with the latest estimate of the IPCC and generally lower than the TCR derived from CMIP6 models, higher values of ECS remain possible within the constrained parameter ensemble of FaIR compared to the estimate of the IPCC and ECS from CMIP6 models (Fig. 1). This is caused by the constraint that is applied to generate the constrained parameter ensemble of FaIR being unable to rule out high values of ECS (Leach et al., 2021). Extremely high values of GMST produced by fair towards the end of the model period might therefore be unrealistic.

When comparing values of GMST from FaIR to the threshold temperatures of the TEs, we account for the uncertainty in the threshold temperatures by relying on the respective ranges specified by (Armstrong McKay et al., 2022) (Tab. 1). It must be noted that additional uncertainty about the timing of triggering TEs might exist, since the threshold temperature of slow-onset TEs like ice sheets can be exceeded temporarily without triggering the TE if the overshoot time is short compared to the characteristic timescale of the TE (Ritchie et al., 2021). We do not account for this behaviour in this study, as it would significantly increase the complexity of our analysis.

To assess the impacts of carbon TEs and how they change the probabilities of triggering other TEs, we develop a conceptual carbon tipping elements model (CTEM) (Sec. 2.3) which is coupled to FaIR and able to represent the estimated behaviour of carbon TEs from Armstrong McKay et al. (2022) (Fig. 2). As CTEM is not process-based, our results should not be seen as diagnostic, but can be helpful to explore the general dynamics of the carbon TEs.

To propagate the uncertainties within the climate response, the carbon TEs and the threshold temperatures, we apply a Monte Carlo approach (Metropolis et al., 1953) to generate large model ensembles. These ensembles are used to analyse the potential carbon emissions and

the temperature impact of carbon TEs, how likely TEs are to be triggered under the various SSPs and how those probabilities change if carbon emissions from carbon TEs are included.

# 2 Data and Methods

## 2.1 SSP Emission Pathways

We use the CMIP6 GHG and aerosol emissions and effective radiative forcing datasets employed in the Reduced Complexity Model Intercomparison Project (Nicholls et al., 2020). Both datasets contain global average values with an annual timestep throughout the historical period (1750-2014) which shifts to a decadal timestep for the projection period (2015-2500).

The CMIP6 GHG and aerosol emission projections for the five different SSP scenarios follow Gidden et al. (2019). The emission extensions beyond 2100 follow the conventions described in Meinshausen et al. (2020). Historical emissions (1750–2014) of chemically reactive gases (CO, $CH_4$, $NH_3$, $NO_x$, $SO_2$, non-methane volatile organic compounds) carbonaceous aerosols (black carbon and organic carbon) and $CO_2$ come from the Community Emissions Data System (Hoesly et al., 2018). Historical biomass burning emissions of $CH_4$, black carbon, CO, $NH_3$, $NO_X$, organic carbon, $SO_2$ and non-methane volatile organic compounds come from Van Marle et al. (2017). Global historical $CO_2$ emissions from land-use are taken from the Global Carbon Budget 2016 (Le Quéré et al., 2016). Regional breakdown of land-use $CO_2$ emissions and $N_2O$ emissions come from the Potsdam Real-time Integrated Model for probabilistic Assessment of emissions Paths for historical emissions version 1.0 (Guetschow et al., 2016). Data gaps in the historical emissions were filled with inverse emissions based on CMIP6 concentrations from the Model for the Assessment of Greenhouse Gas Induced Climate Change (MAGICC) 7.0.0 (Meinshausen et al., 2020).

Effective radiative forcing for CMIP6 follows the data provided by Smith (2020).

## 2.2 The FaIR Model

We use the second version of the FaIR model developed by Leach et al. (2021), which is run with an annual timestep. It consists of six equations, five of which are adopted from Myhre et al. (2013). The sixth equation implements a state-dependency of the carbon cycle, which enables a better representation of the relationship between emissions and atmospheric concentrations for historical observations and projections (Leach et al., 2021). As a 0D model, FaIR represents global averages. It maps GHG and aerosol emissions to GMST (Fig. 2). Despite its relative simplicity, FaIR is flexible enough to emulate more complex ESMs from CMIP6 (Leach et al., 2021). In the following, we briefly present the structure of the individual components of the model. A more detailed mathematical description can be found in Leach et al. (2021).

### 2.2.1 Gas Cycle

The $CO_2$ gas cycle is represented by a four-timescale impulse response function, where $CO_2$ emissions accumulate in four different atmospheric pools which are added up to give the total atmospheric concentration. Qualitative analogies for each atmospheric pool can be found in Millar et al. (2017). The decay timescale of $CO_2$ within all atmospheric pools is adjusted depending on temperature, $CO_2$ emissions and atmospheric $CO_2$ concentration, allowing the effective $CO_2$ sink from the atmosphere to change in a state-dependent manner. This mechanism captures the carbon-concentration and carbon-climate feedback over land and ocean found in ESMs by Arora et al. (2020) (Leach et al., 2021). The differences due to non-linearities arising from the decay timescale adjustment have been investigated with various emission pulse experiments and found to be small with $< 0.5°C$ for pulse sizes $< 100\,GtCO_2eq$ (Leach et al., 2021).

Except for $CO_2$, all GHGs are modelled with only one atmospheric gas pool and therefore one decay timescale. The state-dependency of the decay timescale of atmospheric $CO_2$ concentrations is also applied to atmospheric $CH_4$ concentrations, but is not implemented for all other GHGs.

### 2.2.2 Effective Radiative Forcing

The atmospheric GHG concentrations are translated to effective radiative forcing (ERF) by a linear combination of a logarithmic, a linear and a square-root term. The coefficients for each term are individual for each GHG and mostly lead to only one term being used for a certain GHG. For $CO_2$ the square-root and the logarithmic terms are used, and for $CH_4$ only the logarithmic term is used. It must be noted, that overlaps between the spectral bands of GHGs identified by Etminan et al. (2016), which can be represented by including interaction terms in the calculation of ERF as done by Meinshausen et al. (2020), are not included in FaIR to reduce the structural complexity of the model. However, the maximum relative error in radiative forcing introduced by this simplification is only 1.1% (Leach et al., 2021).

Aerosol emissions are directly converted to ERF due to their short atmospheric lifetimes. A number of other mechanisms contributing to ERF such as black carbon on snow are included explicitly in FaIR, with a detailed explanation given in Leach et al. (2021). Natural variations of ERF as well as changes in ERF due to albedo changes caused by anthropogenic land-use are not represented by FaIR, but ERF values for both processes are taken directly from CMIP6 data.

### 2.2.3 Temperature Response

The sum of the ERF from all forcing agents is translated to GMST by using a three-box energy balance model. The commonly used matrix formulation of the energy balance model has been simplified to a three-timescale impulse response function, again reducing the structural complexity of FaIR. Values of GMST are given as anomalies relative to the 1850-1900 period.

### 2.2.4 Parameterization

FaIR allows for probabilistic projections of GMST with parameters selected from a constrained ensemble. To derive this constrained ensemble, Leach et al. (2021) run a $10^6$ member ensemble, sampling the uncertainty within the gas cycle, effective radiative forcing, and thermal response parameters as informed by CMIP6 models. To constrain this full parameter ensemble, they use the distributions of the observed rate and level of the anthropogenic contribution to global warming between 2010 and 2019 (anthropogenic warming index distribution), following the methodology of Haustein et al. (2017). The members of the constrained ensemble are selected by setting the section probability of each member of the full parameter ensemble equal to the likelihood of its simulated warming level and trend within the anthropogenic warming index distribution. This procedure results in a selection probability between zero and one for each member of the full parameter ensemble. The member is selected for the constrained ensemble if its selection probability is higher than a randomly generated number between zero and one, which yields a constrained ensemble with $\sim 9.6 \cdot 10^4$ members. From this constrained parameter ensemble, a subgroup of members can be selected randomly to construct a model ensemble of individual size. Additionally, a default parameterization of FaIR is available, which consists of estimates from previous model studies and measurements or central values from the constrained parameter ensemble.

To rule out possible double counting of carbon emissions from permafrost thaw or Amazon dieback, we have to make sure that these processes are not implicitly included in the parameters of FaIR. This could be the case if carbon emissions from both TEs and the respective warming were included either in the CMIP6 models used to parameterize the carbon cycle of FaIR or in the anthropogenic warming index distribution used to constrain this parameterization.

The CMIP6 data used for the parameterization of the FaIR carbon cycle is derived from the fully coupled and biogeochemical 1pctCO2 runs of eleven CMIP6 models (Arora et al., 2020). Of those eleven models, only two represent permafrost processes by including the effect of active layer thickening on decomposition of soil carbon (Canadell et al., 2021), which means they can represent PFGT but not PFAT or PFTP (See Sec. 1.3 for detailed explanation).

Only three of those eleven CMIP6 models include vegetation dynamics (GFDL-ESM4, MPI-ESM1-2-LR and UKESM1-0-LL) and are therefore able to represent eventual dieback of AMAZ (Arora et al., 2020). Of those three, only GFDL-ESM4 predicts abrupt dieback in parts of AMAZ in the 1pctCO2 run, which, however, does not lead to significant reduction of the total carbon being stored in the Amazon vegetation (Parry et al., 2022). Therefore, we assume that carbon emissions from PFTP, PFAT and AMAZ are not implicitly included in the parameterization of the full parameter ensemble of FaIR.

If carbon emissions from AMAZ, PFTP or PFAT and the resulting global warming were already observable and detected in the dataset used to constrain the full parameter ensemble, the constrained parameter ensemble of FaIR would also account for those additional carbon emissions, as members with lower climate sensitivities were more likely to be excluded. However, no multi-decadal trend of $CO_2$ or $CH_4$ fluxes over the boreal permafrost region is yet detectable (Canadell et al., 2021), hence we assume that PFAT and PFTP carbon emissions are also not included in the constrained parameter ensemble of FaIR. Carbon emissions from AMAZ need to be considered more carefully, as the forest has already turned from a sink into a carbon source at the four measurement sites inspected by (Gatti et al., 2021). To get an impression of the potential magnitude of recent carbon emissions from AMAZ, we average over the four observed trends of total C flux (0.2 $\mathrm{gCm^{-2}d^{-1}}$) and multiply this with the area of the forest of $7.25 \cdot 10^6\,\mathrm{km^2}$ (Gatti et al., 2021) and the days of the measurement period (2010–2018), which gives total emissions of 584 tC. Compared to the potential carbon emissions from AMAZ collapse of up to 75 GtC (Tab. 1), we regard this to be negligible and do assume that major contributions from AMAZ collapse are also not included in the constrained parameter ensemble of FaIR.

## 2.3 Carbon Tipping Elements Model

With CTEM, we introduce a simple, system-dynamics type model that is able to represent the carbon emissions from AMAZ, PFAT, and PFTP, with threshold temperatures, timescales, and impacts consistent with the estimates from Armstrong McKay et al. (2022) (Tab. 1). Each TE is represented by a stock of cumulative carbon emissions it adds to the SSP carbon emissions. The cumulative emissions are represented by the following logistic equation:

$$\frac{dS}{dt} = r\left(\frac{T}{P}\right) S\left(1 - \frac{S}{K}\right), \tag{2}$$

with $S$ being cumulative carbon emissions (in GtC), $r$ the maximum growth rate (in $\mathrm{yr^{-1}}$), $K$ the maximum impact (in GtC), $P$ the threshold temperature (in °C), $T$ GMST relative

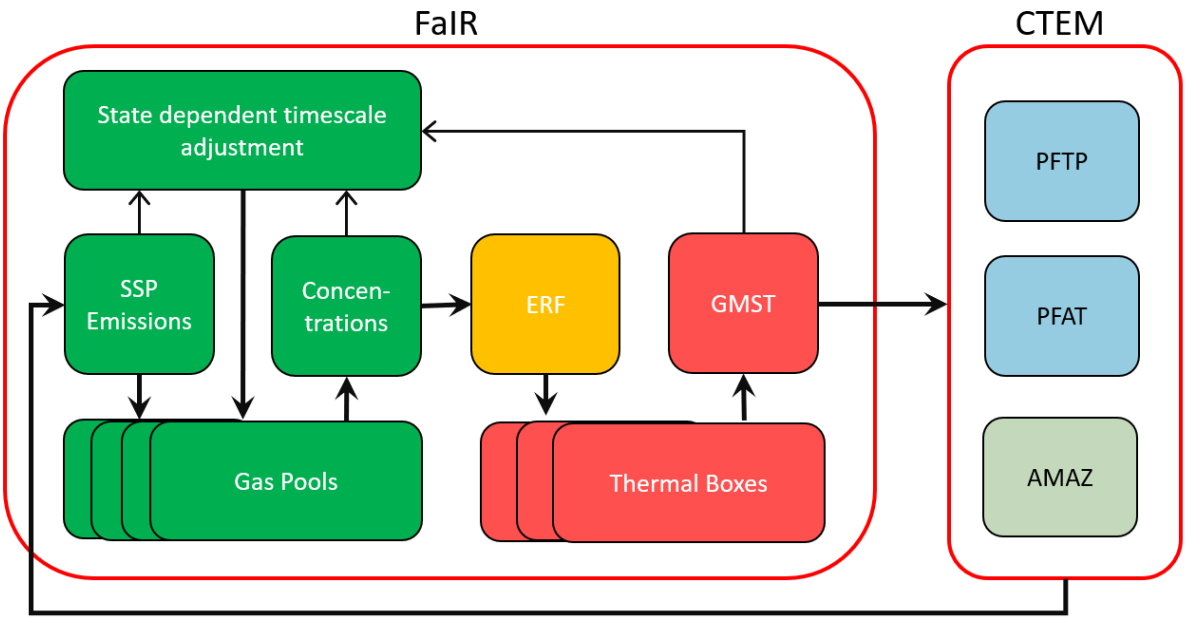


**Figure 2:** Schematic representation of our model framework. The structure of FaIR is reproduced from Leach et al. (2021). The colours split the model in into gas cycle (green), radiative forcing (yellow) and climate response (red) components. Colours of CTEM components represent the Earth system domain of the TE (blue = cryosphere, green = biosphere).

to pre-industrial levels (in °C) and $t$ time (in years). The rate-dependence of all three TEs found by Armstrong McKay et al. (2022) is included by the term $T/P$, which means higher exceedance of the threshold temperature causes faster change in $S$.

For AMAZ and PFTP, the impact is independent of GMST once they are triggered (Tab. 1). Therefore, eq. 2 can be used to represent them without further modifications being necessary.

The impact of PFAT, however, depends on GMST, with higher temperatures leading to increased carbon emissions, and different values for this feedback in 2100 and 2300 (Tab. 1). Therefore, $K$ from eq. 2 needs to be calculated as

$$K = \min(F \cdot T,\ K_{\max}) \tag{3}$$

with

$$F = \begin{cases} F_{100} & \forall\ t \leq 2100 \\ F_{100} \cdot \frac{2300-t}{200} + F_{300} \cdot \frac{t-2100}{200} & \forall\ 2100 < t < 2300 \\ F_{300} & \forall\ t \geq 2300 \end{cases} \tag{4}$$

Here, $K$ is calculated as the product of the feedback strength $F$ (in GtC °C$^{-1}$) and GMST (in °C), limited to the maximum impact $K_{\max}$ (in GtC) of PFAT. In eq. 4, we define $F$ as the feedback strength for the year 2100 ($F_{100}$) before and in 2100, as the feedback strength

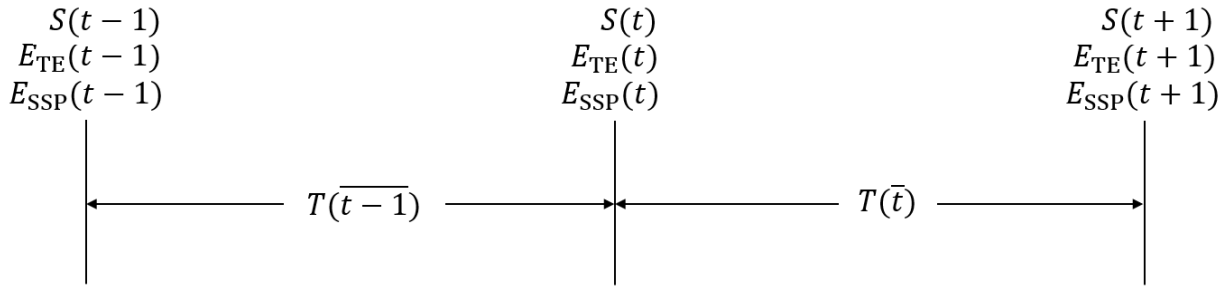


**Figure 3:** Schematic representation of the timestepping scheme in FaIR. Vertical lines represent single timesteps and horizontal arrows the time between them. Variables should be interpreted as single values given at a time step (over vertical lines), or as averages between the timesteps (between vertical lines).

for the year 2300 ($F_{300}$) in and after 2300 and interpolate linearly between these two values between 2100 and 2300.

The resulting set of three differential equations (one for each TE) is solved using a forward difference scheme, similar to the implementation of FaIR (supplement of Leach et al., 2021). In FaIR, output variables such as $T$ are assumed to be average values between two consecutive timesteps (denoted by a bar over $t$), while the values for the input variables such as the annual SSP GHG emissions ($E_{\mathrm{SSP}}$) reside at each timestep (no bar over $t$). To be consistent with this implementation, we define $S$ and the resulting annual carbon emissions from each TE ($E_{\mathrm{TE}}$) also at each timestep (Fig. 3). To calculate $S$ for each timestep ($t$) with a step size ($\Delta t$) of one year, we integrate eq. 2 which yields:

$$S(t) = \left( e^{-a(\overline{t-1})\Delta t} \left( S^{-1}(t-1) - \frac{b(\overline{t-1})}{a(\overline{t-1})} \right) + \frac{b(\overline{t-1})}{a(\overline{t-1})} \right)^{-1}, \tag{5}$$

with the auxiliary variables $a$ and $b$ being calculated as

$$a(\overline{t-1}) = r\frac{T(\overline{t-1})}{P}$$
$$b(\overline{t-1}) = \frac{rT(\overline{t-1})}{PK}.$$

For PFTP and AMAZ eq. 5 can be used directly to calculate $S$, but for PFAT $K$ needs to be calculated using eq. 3 with $T = T(\overline{t-1})$ and is therefore also time-dependent (for the full derivation please see Appendix). Irreversibility of carbon emissions from all three TEs is implemented by setting negative changes of $S$ to zero.

### 2.3.1 Coupling to FaIR

CTEM is coupled to FaIR every timestep by adding $E_{\mathrm{TE}}$ to $E_{\mathrm{SSP}}$. We for each TE we calculate $E_{\mathrm{TE}}$ from $S$ as

$$E_{\mathrm{TE}}(t) = S(t) - S(t-1).$$

The total carbon emissions $E_{\mathrm{TE}}$ are then split up into $CO_2$ and $CH_4$ emissions for all three TEs, with 2.3% of carbon emissions being methane for PFTP, 20% for PFAT and 0% for AMAZ (see Sec. 1.3 for explanation of emission fractions). The annual $CH_4$ and $CO_2$ emissions of all three TEs are then added to $E_{\mathrm{SSP}}(t)$ of the respective SSP and the sum is used to run the next timestep of FaIR, calculating $T(\bar{t})$ which is then used to force CTEM and so on.

### 2.3.2 Calibration

The CTEM needs to be calibrated to resemble the estimated behaviour of PFAT, PFTP and AMAZ summarized in Tab. 1. While values for $F_{100}$, $F_{300}$, $K$, $K_{\mathrm{max}}$, and $P$ are sampled directly from the distributions of those estimates (Sec. 2.4.1), $r$ and the initial stock ($S_0$) need to be calibrated or defined for the model to match the proposed tipping timescales ($H$). For the definition of $S_0$, we define the tipping timescale as the period over which 99% of the cumulative carbon emissions occur (Fig. 4), which means $S_0$ is defined as 0.5% of $K$ ($K_{\mathrm{max}}$ for PFAT). All calibrations of $r$ are performed under the SSP5-8.5 scenario, as most model studies which inform the emission estimates of all three TEs were performed under the corresponding RCP8.5 scenario (Armstrong McKay et al., 2022). To increase transparency, all TEs are calibrated individually, with the other two TEs being deactivated. Furthermore, we use the default parameterization of FaIR for all calibrations.

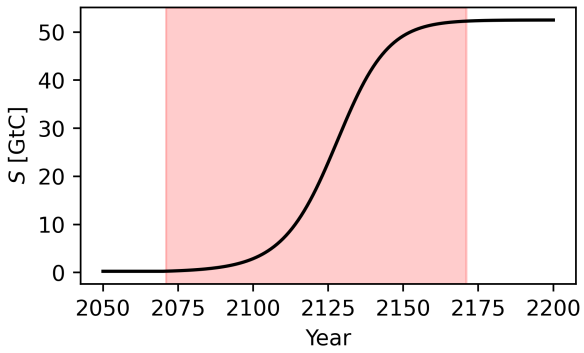


**Figure 4:** $S$ for the calibration of the mean timescale of AMAZ. The red shaded area denotes the period over which 99% of the cumulative carbon emissions occur.

For the calibration of PFTP and AMAZ, we use the respective mean estimate for $P$ and $K$. We calibrate $r$ by splitting the respective range of $H$ from Tab. 1 into $\sim 100$ equally spaced bins, with one value of $r$ fitted to each bin. We define the following objective function, which resembles the squared difference ($D$) between the observed $H$ of the model and the expected

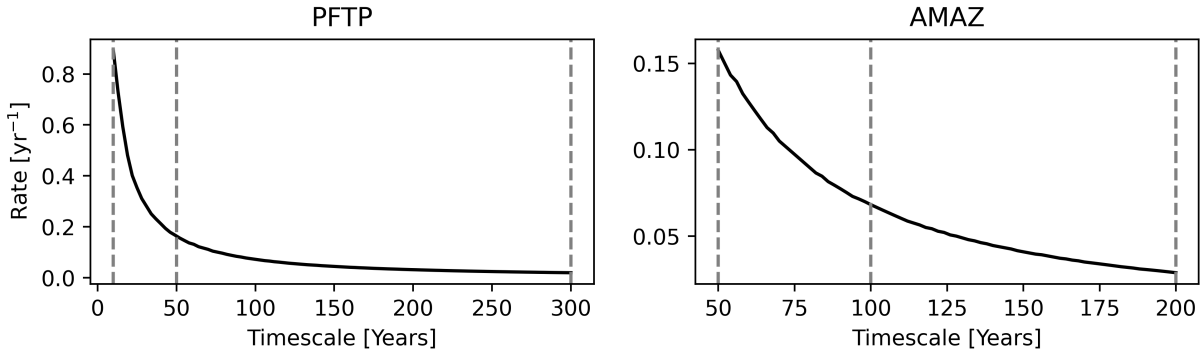


**Figure 5:** Calibrated rate ($r$) for $H$ of PFTP and AMAZ. Grey vertical lines denote maximum, mean and minimum estimate of $H$ from Tab. 1.

value:

$$D = ((Y_{\text{end}} - Y_{\text{start}}) - H)^2, \tag{6}$$

with $Y_{\text{end}}$ being the year in which 99.5% of maximum cumulative emissions are emitted and $Y_{\text{start}}$ the year in which the respective TE is triggered. These values are looked up in the model results without any further time-aggregation being necessary, which increases the performance of the calibration algorithm. The objective function is minimized for each bin of $H$ for AMAZ and PFTP using the Nealder-Mead algorithm (Gao and Han, 2012), which gives the calibrated values of $r$ (Fig. 5). The objective function has been successfully minimized to zero for all bins of $H$ for PFTP and AMAZ.

For PFAT, we only calibrate $r$ for the mean estimate of $H$, using the mean values of $P$ and $K_{\text{max}}$ with $K = K_{\text{max}}$ at all times. This is due to the fact that the timescale over which the emissions from PFAT occur is already included in the ranges of $F_{100}$ and $F_{300}$. The value of $r = 0.041$ yr$^{-1}$ corresponding to the mean value of $H = 200$ years is determined by using the objective function (eq. 6), which is minimized to zero.

### 2.3.3 Test of the Calibration

Here, we investigate how well the calibrated version of CTEM resembles the estimated values of $H$ of PFTP, AMAZ and $F_{100}$ and $F_{300}$ of PFAT from Tab. 1.

To test the emission feedbacks in 2100 and 2300 of PFAT, we generate 10 equally spaced values of $F_{100}$ and $F_{300}$, covering the whole uncertainty range and 10 equally spaced values of $P$, also covering the respective uncertainty range. With this parameter set, we generate 100 model runs, one for each combination of pairs of $F_{100}$ and $F_{300}$ and $P$. CTEM is coupled to FaIR which is run with its default parameterization under SSP5-8.5, which has also been used

for the calibration of CTEM. Now we calculate the difference between the cumulative carbon emissions from CTEM and the expected cumulative carbon emissions based on the values of $F_{100}$ and $F_{300}$ and $T$ for the years 2100 and 2300. In 2100 there are significant deviations between the two, with the cumulative emissions of PFAT from CTEM being smaller than expected (Fig. 6). The relative error of the cumulative carbon emissions in 2100 increases with increasing values for $P$, whereas the value of $F_{100}$ does not seem to have an effect on the error. Maximum errors of up to 80% are reached for the highest realization of $P$. Nevertheless, the relative error is reduced to values below 5% for all combinations of $F_{300}$ and $P$ in 2300. This implies that the medium $H$ is too large to allow for high enough emissions between crossing the tipping point of PFAT and 2100. However, we regard this as the best possible implementation of PFAT since the long-term cumulative carbon emissions still roughly match the estimates and lower values of $H$ would lead to potentially unrealistic abrupt carbon emissions.

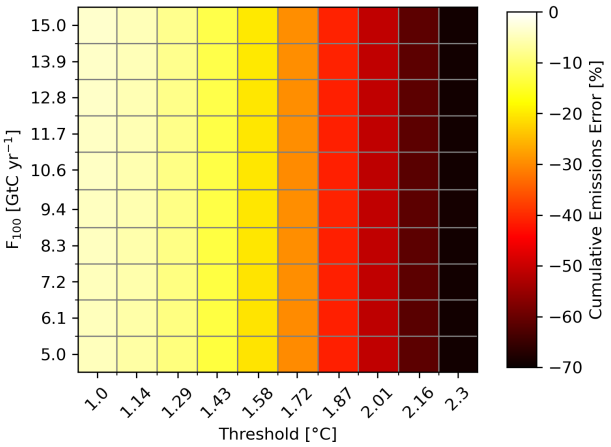


**Figure 6:** Deviations between the expected and the modelled cumulative carbon emissions from PFAT in 2100. One box represents one model realization with the respective values of $P$ and $F_{100}$ used for PFAT, with all other TEs within CTEM being deactivated and FaIR run with default parametrization under SSP5-8.5.

For PFTP and AMAZ, we test how well the estimated values of $H$ are met by CTEM for various combinations of $K$ and $P$. We produce 10 equally spaced values of $K$ and $P$, covering the whole uncertainty range and run the model for each combination for both PFTP and AMAZ, with all other TEs within CTEM being deactivated. In this manner, we produce 100 model runs for the minimum, the mean, and the maximum estimate of $H$ for PFTP and AMAZ. FaIR is again run with its default parameterization under SSP5-8.5. The relative error in $H$ of PFTP and AMAZ increases with increasing values for $H$, with CTEM producing smaller values of $H$ than expected for low $P$ and higher values for high $P$. (Fig. 7). Differences in $K$ seem to have nearly no impact on the error in $H$ for both AMAZ and PFTP. Notably, the relative errors in $H$ are higher for AMAZ, with -27% and 45% being reached for the maximum estimate of $H$. For PFTP, the errors are more symmetric, lying between -19% and 19% for the maximum estimate of $H$. The change of sign of the errors around the mean value of $P$ makes sense, as the mean value of $P$ has been used for the calibration. The observed lower values of $H$ for low $P$ and higher values of $H$ for high $P$ can be explained by the rate-dependence of both

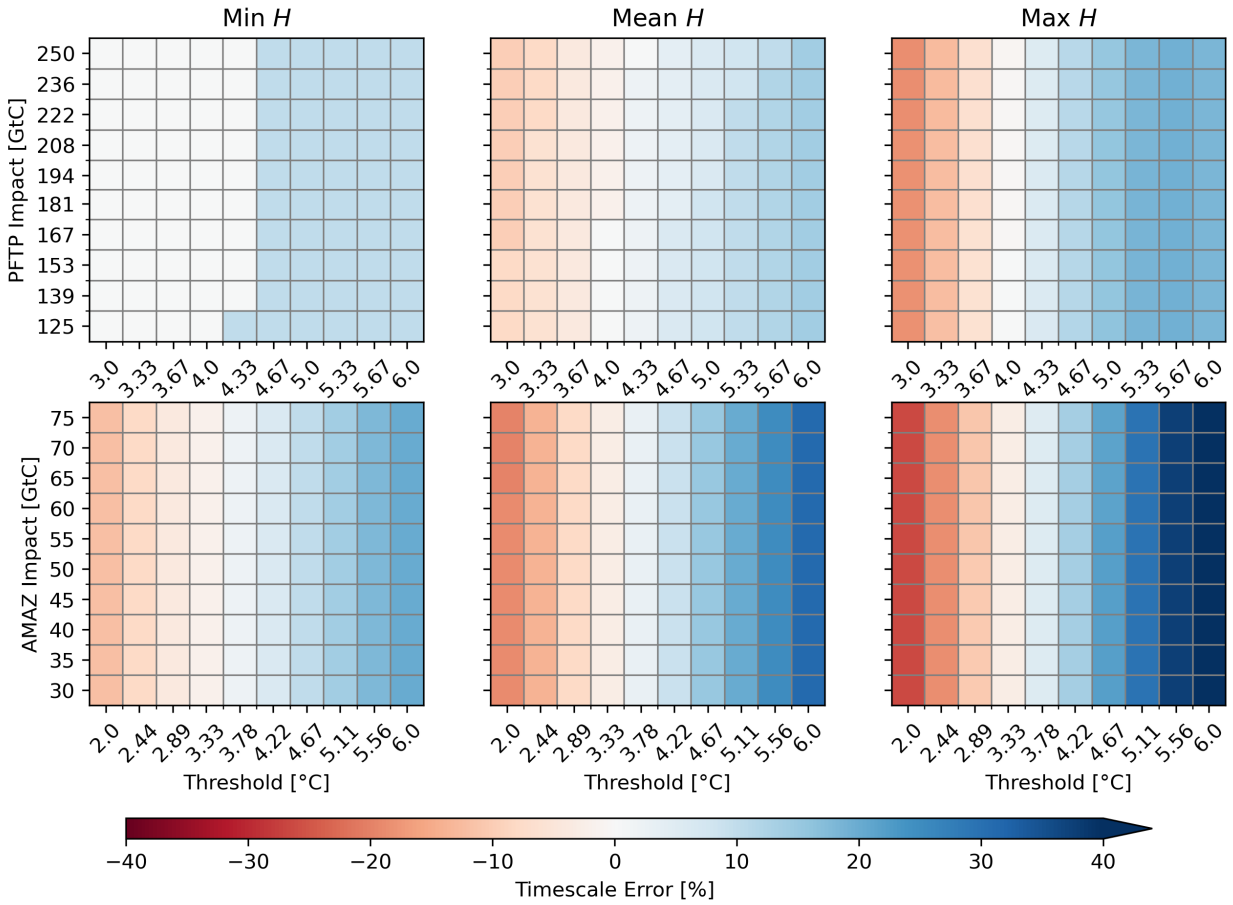


**Figure 7:** Deviations between the expected and the modelled $H$ from CTEM in percent for the minimum, mean, and maximum estimate of $H$ of PFTP and AMAZ with values of $K$ and $P$ equally spaced between the respective maximum and minimum estimate. One box represents one model realization with the respective values of $P$ and $K$ used for PFTP (upper row) or AMAZ (lower row) with all other TEs within CTEM being deactivated and FaIR run with default parametrization under SSP5-8.5.

TEs, with higher exceedance of $P$ leading to faster tipping. As the increase of $T$ slows down over time under SSP5-8.5 (Fig. 13), lower values of $P$ lead to lower $H$ and vice versa. Hence, the observed errors in $H$ of PFTP and AMAZ from CTEM comply with the rate dependence of both TEs and are therefore regarded to be realistic.

## 2.4 Model Ensembles

We construct a coupled (FaIR coupled to CTEM) and an uncoupled (FaIR only) 5000 members model ensemble for all five SSPs. Hereby, we follow a Monte Carlo scheme (Metropolis et al., 1953) to propagate the uncertainties within FaIR and CTEM. For stability analysis or the inspection of quantities near the extremes of the resulting variable distributions, we construct

up to 20 coupled model ensembles with 5000 members each to determine the robustness of the results.

### 2.4.1 Sampling Strategy

For the parameterization of FaIR, we randomly select 5000 members of the constrained parameter ensemble (see Sec.2.2.4 for the constrained ensemble). We use the same parameter sample for FaIR in both ensembles to make sure that changes in the climate response only arise from carbon emissions of the carbon TEs. To determine the probability of triggering, we sample the uncertainty range of $P$ for all TEs, again using the same parameter sample for both ensembles. For CTEM, we sample the uncertainty ranges of the whole parameter set, which consists of $H$, $P$, $K$ for PFTP and AMAZ, and $P$, $F_{100}$, $F_{300}$ and $K_{\max}$ for PFAT. For the sampling process of $P$ for all TEs and $H$ for PFTP and AMAZ, we infer probability distributions from the estimates of $P$ and $H$ in Tab. 1, deciding that the minimum estimate, the best estimate, and the maximum estimate should correspond to the 5th, the 50th and the 95th percentile of the respective probability distribution. To determine the probability distributions which best fits those percentiles, we use the "rriskDistributions" package (Belgorodski et al., 2017), which chooses out of 17 continuous probability distributions, minimizing the absolute difference between the given and the actual percentiles (for a list of all distributions see Appendix).

For the distribution of $P$ for all TEs, we derive eight log-normal, four triangular, three normal and one Gompertz distribution (Fig. 8). It must be noted, that this choice of probability distributions does not involve any additional information about the suitability of certain probability distributions, but is only based on the fitting routine introduced above. While some distributions of $P$ agree perfectly with the given percentiles (AMOC, EAIS, TUND, BARI, SAHL), others deviate substantially with RMSEs higher than 0.2°C (WAIS, BORF, EASB, LABC). In the case of WAIS, EASB, and LABC this deviation is mainly caused by too low values at the 95th percentile, which is reached at 2.3°C rather than 3°C for WAIS, 4.6°C rather than 6°C for EASB, and 3.1°C rather than 3.8°C for LABC. In the case of BORF, the relatively high RMSE is caused by a too high value at the 5th percentile (1.7°C rather than 1.4°C) and a too low value at the 50th percentile (3.8°C rather than 4°C), while the 95th percentile agrees well with the expected value (less than 0.02°C deviation). Even though the deviations between the given and the actual percentiles of those four TEs are significant, we regard them to be acceptable, given that they cannot be reduced with our methodology, meaning that other probability distributions would be needed to achieve this. However, it must be kept in mind that high probabilities of tipping might be reached at too low values of GMST for WAIS, EASB and LABC due to their imperfect probability distributions of $P$.

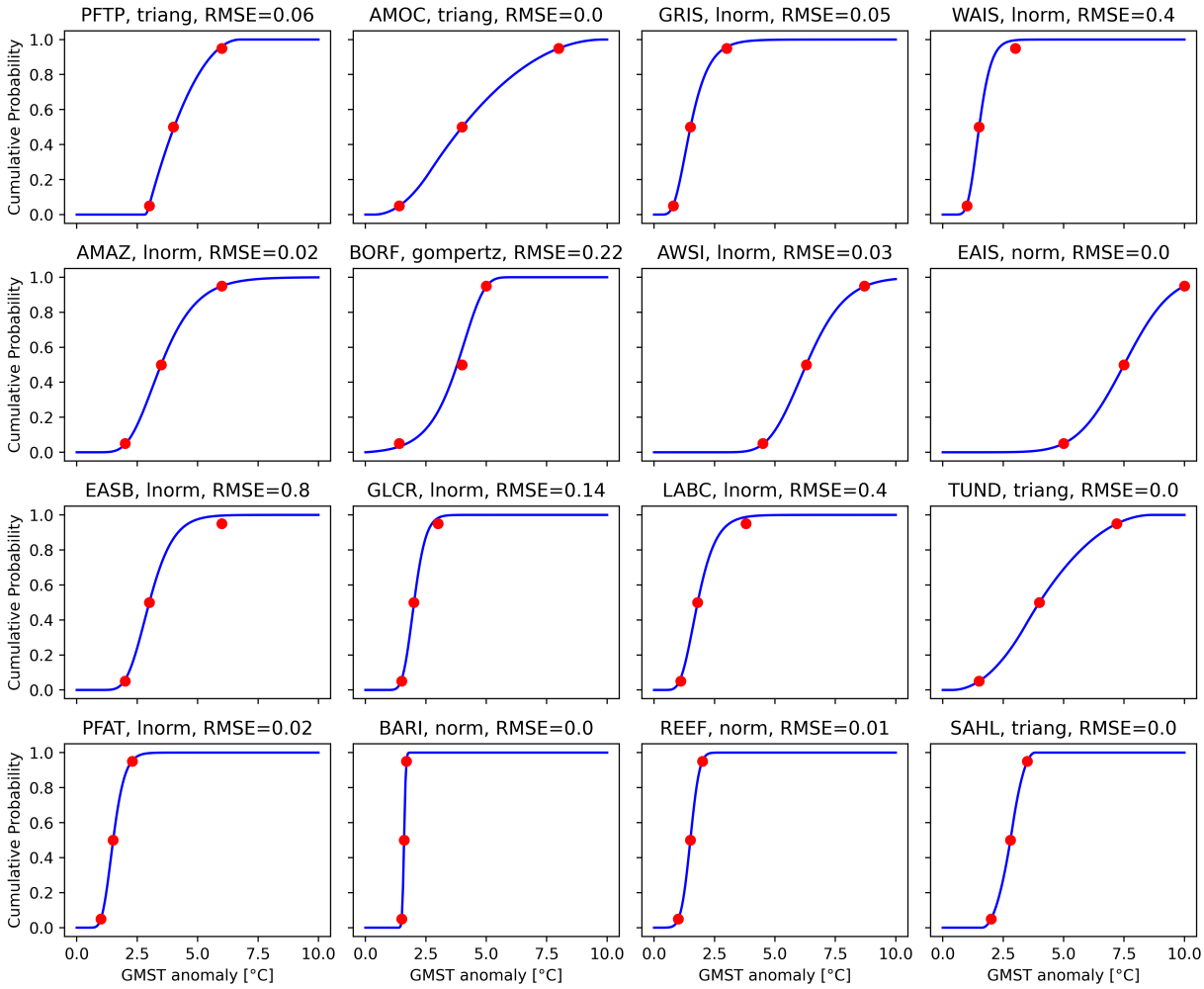


**Figure 8:** Cumulative distribution functions of $P$ for all TEs, together with the RMSE between the given percentiles (red dots) and the actual percentiles of the respective distribution. The title states TE, distribution type and RMSE in °C.

For the distribution of $H$ for PFTP and AMAZ, we derive one log-normal distribution each (Fig. 9). The distribution for AMAZ fits the given percentiles nearly perfectly, with a root-mean-square error (RMSE) of only 0.02 years, while the distribution for PFTP deviates more, with a RMSE of 14.85 years. The main source for this comparably large error is the deviation of the actual 95th percentile, which lies at 274.3 years rather than 300 years.

The impacts $K$ of PFTP and AMAZ and the maximum impact $K_{\max}$ of PFAT are sampled from continuous uniform distributions, with the same probability for all values within the given ranges from Tab. 1 (Fig. 10). We regard this reasonable since Armstrong McKay et al. (2022) only give maximum and minimum values for those variables, and we do not have any additional information about their distribution. Furthermore, the estimates of the impacts are given with low (PFTP) or medium confidence (PFAT, AMAZ) and rest on

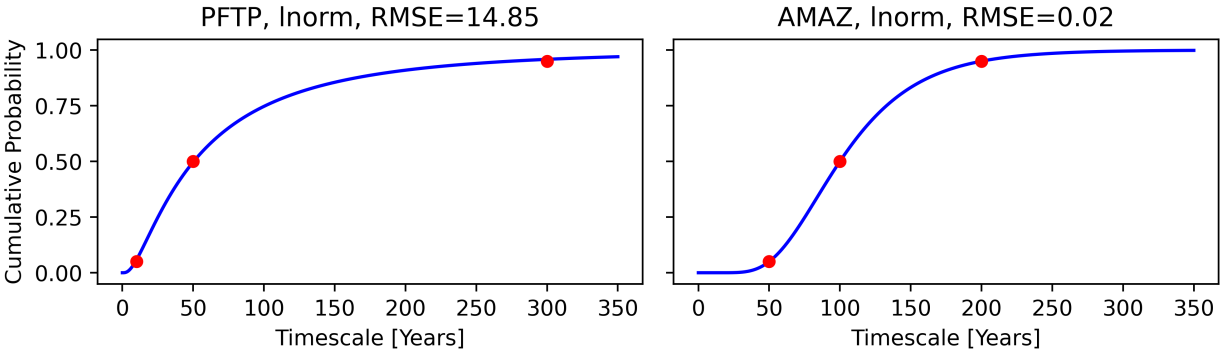


**Figure 9:** Cumulative distribution functions of $H$ for PFTP and AMAZ, together with the RMSE between the given percentiles (red dots) and the actual percentiles of the respective distribution. The title states TE, distribution and RMSE in years.

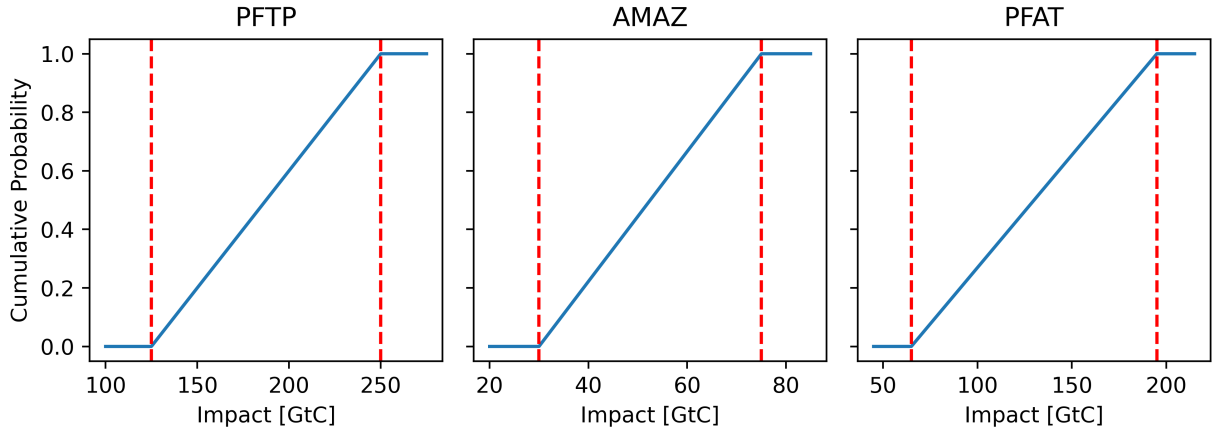


**Figure 10:** Cumulative distribution functions of $K$ for AMAZ and PFTP and $K_{\max}$ for PFAT. The dotted red lines indicate the range of the respective variable from Tab. 1.

the comparison of different model studies and expert judgments (PFAT, PFTP) or rough calculations (AMAZ) which do not give more information about the distributions of the impacts (Sec. 1.3 and Supplement of Armstrong McKay et al. (2022)).

The feedback strengths $F_{100}$ and $F_{300}$ of PFAT are also sampled from continuous uniform distributions, with the same probability for all values within the given ranges from Tab. 1 (Fig. 11). Here, the same argument holds as for the selection of the distributions of $K$ and $K_{\max}$. The estimated range of the PFAT emission feedback from Armstrong McKay et al. (2022) is based on two studies, one using inventory models (Turetsky et al., 2020) and the other one relying on expert judgments (Schuur et al., 2015). Both studies do not give any meaningful indication about the distributions of PFAT feedbacks.

We use Latin hypercube sampling (McKay et al., 1979) to sample from the probability

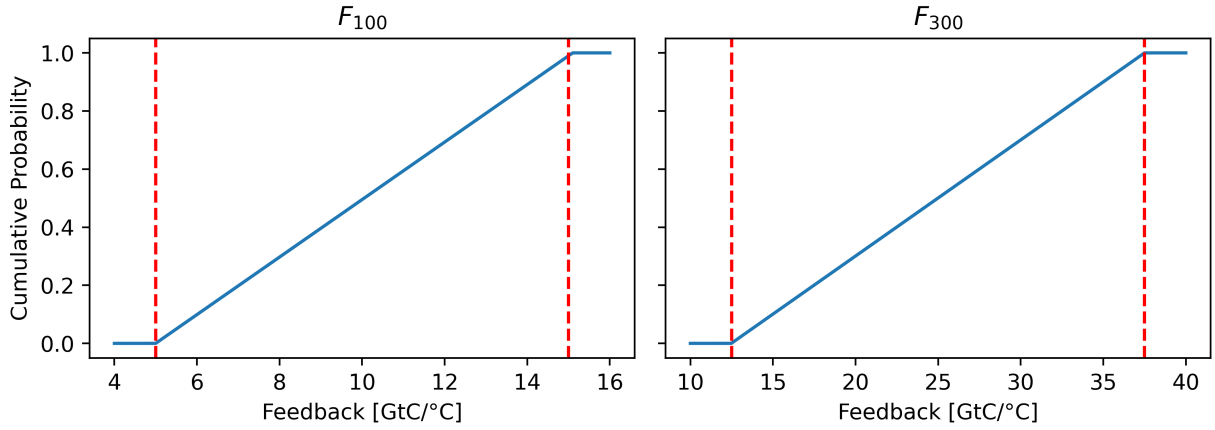


**Figure 11:** Cumulative distribution function of $F_{100}$ and $F_{300}$ of PFAT. The dotted red lines indicate the range of the respective variable from Tab. 1.

distributions of $P$, $K$, $K_{\max}$, $F_{100}$, $F_{300}$, and $H$ introduced in the sections above.
We assume that all parameters within the parameter set of CTEM are uncorrelated, except for $F_{100}$ and $F_{300}$, which are correlated with a correlation coefficient of 1. The decision about the correlation of the parameters represents our understanding that there are no correlations, or at least no clear evidence for them, between the threshold temperatures, the timescales, or the impacts of AMAZ, PFAT and PFTP. The correlation between $F_{100}$ and $F_{300}$ is established since $H$ of PFAT is included in those parameters, and we assume that $H$ is constant over time, e.g., a low feedback in 2100 associated with a high $H$ also means low feedback in 2300 due to the same high $H$ the emissions occur over.

To generate model ensembles of size $n = 5000$, the Latin hypercube sampling is performed as follows. The interval $[0,\ 1)$ is divided into $n$ disjoint intervals with the same probability, which means in our case they are of the same size. From each interval, a random value $y_\mathrm{j}$ is picked, with $j = 1, 2, ..., n$. For every $y_\mathrm{j}$, the corresponding parameter $x_\mathrm{j}$ is determined by using the inverse form of the cumulative distribution function ($F$) of the respective probability distribution:

$$x_\mathrm{j} = F^{-1}(y_\mathrm{j}), \qquad j = 1, 2, ..., n.$$

In this manner, we sample from all parameter probability distributions introduced above, which gives us a parameter sample of size ten for CTEM, and 13 additional samples of $P$, one for each TE not included in CTEM, for every coupled ensemble member. For every uncoupled ensemble member, we only use one sample of $P$ for each of the 16 TEs, which are the same values as for the corresponding coupled ensemble member.

For functions that are monotonic in each sampled parameter, Latin hypercube sampling is superior to random sampling as it reduces the variance of aggregated measured between

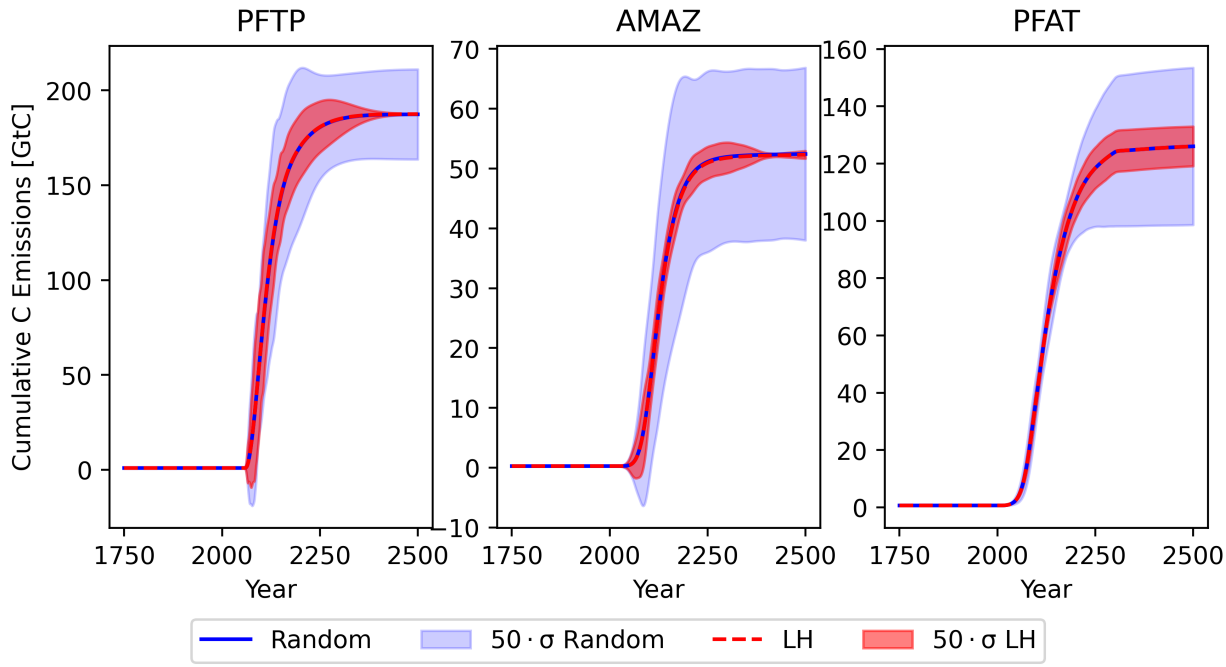


**Figure 12:** Mean ($\mu$) and fifty times standard deviation ($\sigma$) of the ensemble mean of $S$ from ten coupled 5000 member ensembles using Latin hypercube (LH) sampling and ten coupled 5000 member ensembles using random sampling, run under SSP5-8.5.

ensembles, such as the ensemble mean (Theorem 3.1 in Helton and Davis (2003)). We assume that the function for $S$ (eq. 5) CTEM is based on, is monotonic in all sampled parameters $H$, $P$, $K$, $K_{\max}$, $F_{100}$, and $F_{300}$, and that therefore Latin hypercube sampling is superior to random sampling for CTEM. Rather than proving this mathematically, we test this hypothesis in a model experiment. We construct ten coupled 5000 member ensembles using Latin hypercube sampling and another ten coupled 5000 member ensembles using random sampling for the whole parameter set of CTEM, run under SSP5-8.5 and with FaIR in its default parameterization. The results show that the variance of the ensemble mean of $S$ is small for both sampling techniques, but again reduced for all three TEs at all times when Latin hypercube sampling is used (Fig. 12). Especially for PFTP and AMAZ there is a high degree of convergence towards the end of the time series when Latin hypercube sampling is used that is not achieved by random sampling.

### 2.4.2 Robustness of Ensemble Results

To examine whether an ensemble of size 5000 is sufficiently large to approximate the distributions of the output variables with our Monte Carlo approach, we create 20 coupled ensembles with 5000 members and run under SSP5-8.5, sampling uncertainties within FaIR and CTEM. As carbon emissions from CTEM are used to calculate $T$, which is also the

final output variable of FaIR, it includes uncertainties from all parameters and is hence expected to vary most between different ensembles. Therefore, we inspect the deviation of $T$ between the 20 ensembles. While the 5th percentile and the mean of $T$ are nearly equal for all ensembles, with standard deviations below 0.06°C at all times, the 95th percentile deviates slightly between the ensembles, with a standard deviation of up to 0.24°C (Fig. 13). For all three percentiles, the deviation between the ensembles increases with model lead time. Even though we regard those deviations to be sufficiently small, given the range of $T$ between the 5th and the 95th percentile, results associated with temperatures from the upper end of their distribution should still be inspected more carefully.

## 2.5 Calculation of Tipping Probabilities

To calculate the probabilities of triggering any of the 16 TEs discussed in this study, we sample one value of $P$ from the respective distribution (Fig. 8) for each TE and each ensemble member. If $T$ of that ensemble member exceeds $P$, the TE is counted as triggered. In this manner, we derive the share of ensemble members in which a TE is triggered for each TE at all times. As all TEs discussed here are by definition irreversible on the considered timescale, the share of triggered TEs cannot decrease with time, even if $T$ would decrease. The share of ensemble members with triggered TEs is then used to further investigate the probabilities of triggering, e.g., by calculating the timing of the exceedance of certain share percentages.

## 2.6 Testing Statistical Significance

For the inspection of temperature distributions from the coupled and the uncoupled ensemble in 2100 and 2300, we generate nine additional coupled ensembles to make statements about the difference between the distributions and their statistical significance. More specifically, we calculate percentiles and the probabilities of exceeding certain temperatures from both temperature distributions. Estimates of the standard deviation of those results are only available for the coupled ensembles, as we use only one uncoupled ensemble. Therefore, the general setting is

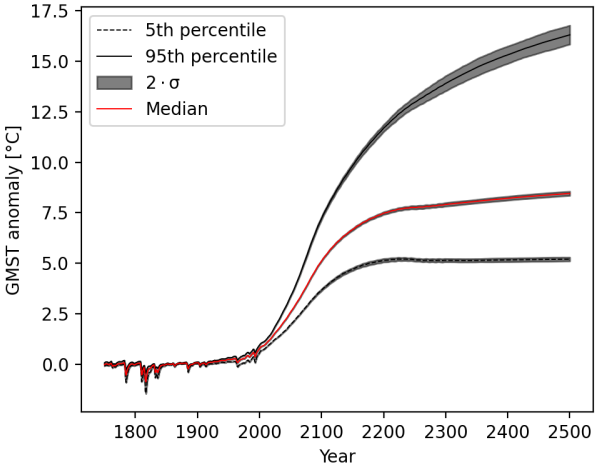


**Figure 13:** Comparison of the 5th percentile, the median and the 95th percentile of $T$ between 20 coupled ensembles with 5000 members each. Mean estimate from all ensembles and two times standard deviation ($\sigma$) between the ensembles.

that we have $n_c = 10$ samples $X$ from the coupled ensembles with the arithmetic mean ($\hat{\mu}_c$) and one estimate of the mean from the uncoupled ensemble ($\hat{\mu}_u$), which is the single value obtained from the uncoupled ensemble. We test the null hypothesis for the means of the underlying distributions $\mu_c = \mu_u$ against the alternative hypothesis $\mu_c > \mu_u$, using a one-sided Student's $t$ test following the methodology of Storch and Zwiers (1999). For this analysis to be applicable, three conditions need to be satisfied. First, all samples $X$ need to be independent. Second, the distribution that generates the samples $X$ must be the same for every sample and third, the distribution must be normal. Condition one and two are met by our construction methodology of the coupled ensemble. For condition three, we can only assume that it is met, but the Student's $t$ test is relatively robust against deviations from this condition (Storch and Zwiers, 1999).

Under the null hypothesis, the variable

$$t = \frac{\hat{\mu}_c - \hat{\mu}_u}{S_c \sqrt{\frac{1}{n_c}}},$$

with $S_c$ being the arithmetic standard deviation of the samples from the coupled ensembles, is distributed according to a Student distribution with $n_c - 1$ degrees of freedom. Therefore, we calculate the $p-$value as

$$p = 1 - \int_{-\infty}^{t} Student(t^*)dt^*,$$

with $Student(t^*)$ being the Student distribution with $n_c - 1$ degrees of freedom. The $p-$value is then compared to the significance level of 99%, i.e., $p < 0.01$ is required to reject the null hypothesis for the alternative hypothesis.

# 3 Results

In this section, we first give an overview over the additional carbon emissions from the carbon TEs and the respective temperature impacts, before we present the tipping probabilities and how they change due to the temperature impact from carbon TEs.

We give general results for all Tier1 SSPs, however, to stay within the scope of this study, we focus on SSP1-1.9, SSP2-4.5 and SSP5-8.5 for some parts of the more detailed analysis. With those three scenarios, we span the whole range of possible temperature impacts from all Tier1 SSP scenarios (Fig 14). SSP1-1.9 is the "best case" scenario with the lowest temperature increase and therefore still in compliance with the Paris Agreement, aiming to limit global warming to 1.5°C compared to pre-industrial levels (UNFCCC, 2015). SSP2-4.5 is the scenario that produces temperatures closest to the expected 2.7°C in 2100 current policies and actions are expected to lead to (Climate Action Tracker, 2022) and can be termed a "middle of the road" scenario. SSP5-8.5 can be seen as a "worst case" scenario, associated with ongoing fossil-fueled development causing a maximum global warming.

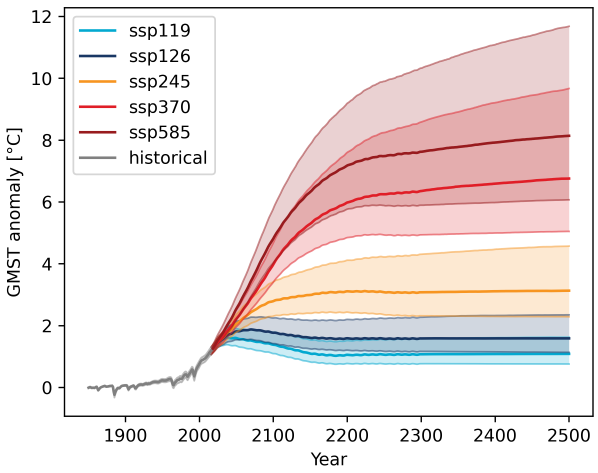


**Figure 14:** 16.6th to 83.3rd percentile (shaded) and median (solid line) of GMST relative to the 1850-1900 period for the Tier1 SSPs from the uncoupled ensemble.

The calibrated language of the IPCC for the description of probabilities is used within this study: virtually certain: 99 – 100%, extremely likely: 95 – 100%, very likely: 90 – 100%, likely: 66 – 100%, more likely than not: >50 – 100%, about as likely as not: 33 – 66%, unlikely: 0 – 33%, very unlikely: 0 – 10%, and extremely unlikely: 0 – 5% (Chen et al., 2021).

## 3.1 Emissions from Carbon Tipping Elements

We restrict the inspection of carbon emissions to the period between 2000 and the end of the model runs in 2500 since no emissions from CTEM occur before 2000. Our analysis of the carbon emissions from the carbon TES within the coupled ensemble mostly rests on the inspection of the 5th, the 95th percentile and the median of carbon emissions to gain an understanding of the ensemble spread. However, it must be noted that ensemble members with untipped carbon TEs skew the distributions towards lower values. Therefore,

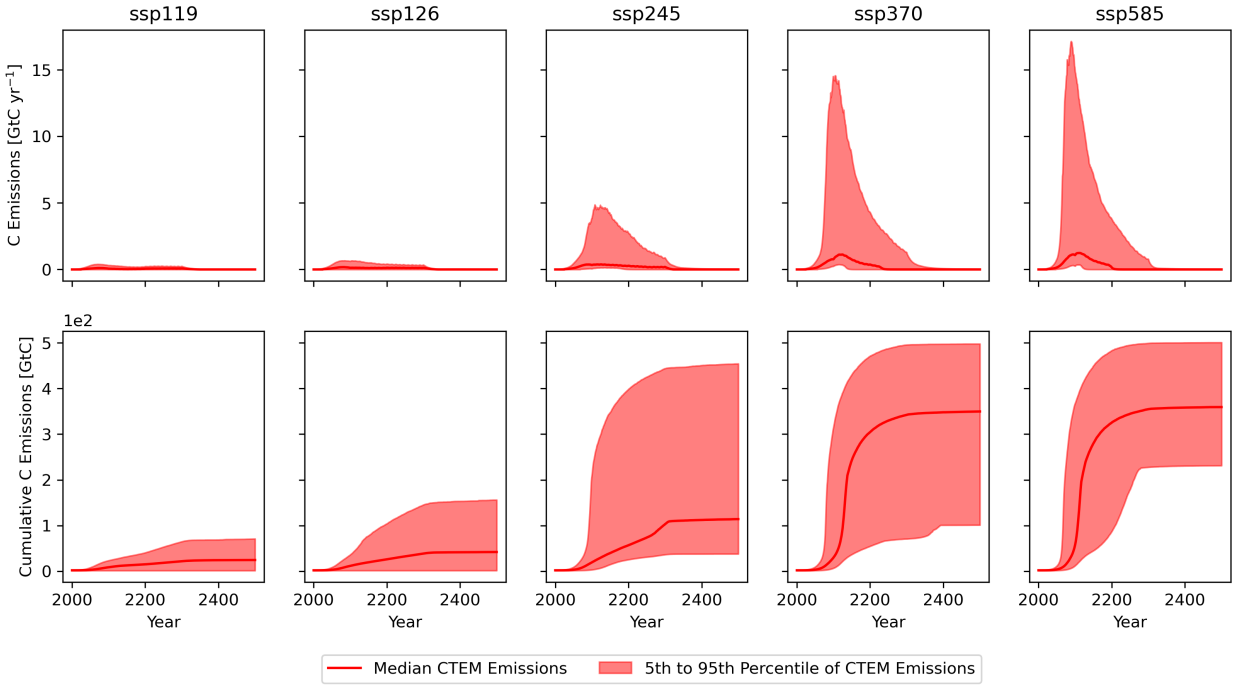


**Figure 15:** Carbon emissions and cumulative carbon emissions from the carbon TEs (modelled by CTEM) between 2000 and 2500.

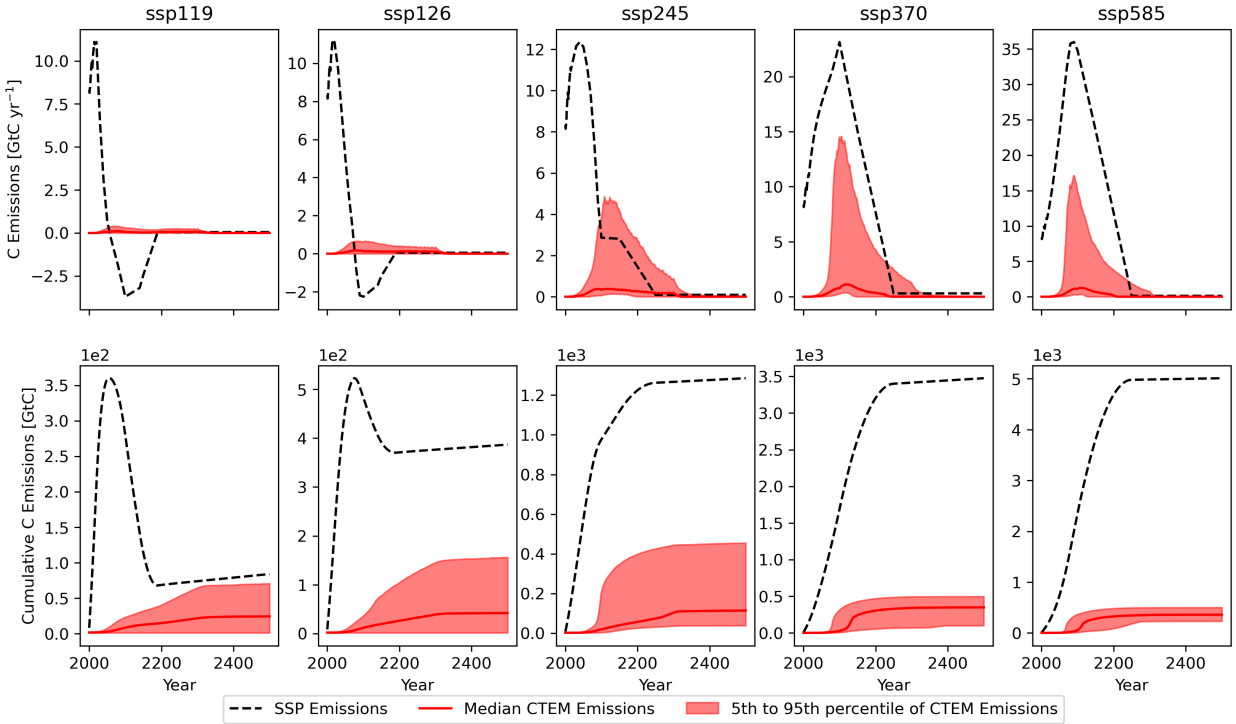


**Figure 16:** Carbon emissions and cumulative carbon emissions from the Tier1 SSP scenarios and the carbon TEs (modelled by CTEM) between 2000 and 2500.

| | | 2050 | 2100 | 2200 | 2300 | 2400 | 2500 |
|---|---|---|---|---|---|---|---|
| SSP1-1.9 | | | | | | | |
| $CO_2$ | [GtC] | 1 (0-5) | 5 (0-19) | 11 (0-36) | 16 (0-58) | 18 (0-63) | 18 (0-66) |
| $CH_4$ | [$GtCH_4$] | 0.3 (0-1.5) | 1.8 (0-5.6) | 3.5 (0-10.2) | 5.3 (0-16.7) | 5.9 (0-17.8) | 6 (0-18.3) |
| d$T$ | [°C] | 0.01 (0-0.07) | 0.04 (0-0.17) | 0.03 (0-0.2) | 0.05 (0-0.29) | 0.03 (0-0.23) | 0.03 (0-0.22) |
| SSP1-2.6 | | | | | | | |
| $CO_2$ | [GtC] | 1 (0-5) | 8 (0-29) | 20 (0-85) | 30 (0-121) | 33 (0-136) | 33 (0-152) |
| $CH_4$ | [$GtCH_4$] | 0.3 (0-1.6) | 2.6 (0-7.5) | 6.4 (0-15.9) | 9.8 (0-25.3) | 10.5 (0-27.0) | 10.7 (0-27.8) |
| d$T$ | [°C] | 0.01 (0-0.07) | 0.07 (0-0.24) | 0.08 (0-0.34) | 0.1 (0-0.49) | 0.06 (0-0.47) | 0.06 (0-0.53) |
| SSP2-4.5 | | | | | | | |
| $CO_2$ | [GtC] | 1 (0-6) | 16 (2-155) | 67 (19-324) | 102 (28-359) | 108 (30-365) | 112 (30-369) |
| $CH_4$ | [$GtCH_4$] | 0.3 (0-1.8) | 4.7 (0.4-13.6) | 15.6 (6.3-33) | 21.9 (9.2-43.3) | 22.8 (9.6-44.7) | 23.1 (9.7-45.3) |
| d$T$ | [°C] | 0.01 (0-0.08) | 0.13 (0.02-0.61) | 0.2 (0.06-0.85) | 0.22 (0.06-0.91) | 0.16 (0.03-0.89) | 0.16(0.03-0.91) |
| SSP3-7.0 | | | | | | | |
| $CO_2$ | [GtC] | 1 (0-6) | 34 (6-245) | 285 (91-381) | 318 (143-403) | 322 (154-406) | 324 (160-407) |
| $CH_4$ | [$GtCH_4$] | 0.4 (0-1.9) | 8.1 (1.5-20) | 29.3 (17-47.5) | 35.2 (22.9-53.9) | 35.6 (23.4-53.9) | 35.9 (23.6-54) |
| d$T$ | [°C] | 0.01 (0-0.08) | 0.25 (0.05-0.94) | 0.39 (0.15-0.81) | 0.31 (0.13-0.66) | 0.27 (0.1-0.63) | 0.26 (0.09-0.63) |
| SSP5-8.5 | | | | | | | |
| $CO_2$ | [GtC] | 2 (0-8) | 78 (13-283) | 304 (138-389) | 328 (235-408) | 330 (244-410) | 331 (246-411) |
| $CH_4$ | [$GtCH_4$] | 0.5 (0-2.3) | 12.4 (3.3-26.2) | 32 (20.6-50.5) | 37.1 (24.1-54.3) | 37.4 (24.3-54.6) | 37.7 (24.3-54.7) |
| d$T$ | [°C] | 0.02 (0-0.1) | 0.4 (0.09-1.11) | 0.31 (0.13-0.64) | 0.23 (0.1-0.52) | 0.19 (0.08-0.47) | 0.18 (0.08-0.47) |

**Table 2:** Median and very likely range (5th – 95th percentile) of cumulative $CO_2$ and $CH_4$ emissions and the GMST increase (d$T$) caused by the carbon TEs.

the resulting percentiles do not represent distributions of the carbon emissions from carbon TEs in case of tipping, but do also include information about the share of ensemble members that feature such tipping. This also holds for the percentiles of GMST presented in the next section.

The cumulative carbon emissions from carbon TEs are increasing from SSP1-1.9 to SSP5-8.5 (Fig. 15, Tab. 2). However, carbon emissions from the carbon TEs have the highest potential to make up for high shares of the total cumulative carbon emissions under low emission scenarios (Fig. 16). The 95th percentile of cumulative carbon emissions from carbon TEs reaches 84%, 40%, and 35% of the anthropogenic cumulative carbon emissions in 2500 under SSP1-1.9, SSP1-2.6, and SSP2-4.5 respectively. Yet, such high carbon emissions from the carbon TEs remain unlikely under SSP1-1.9 and SSP1-2.6, with the median cumulative carbon emissions being less than half as high as the 95th percentile. Even zero carbon emissions from the carbon TEs remain possible under those scenarios (Tab. 2). The confidence in the occurrence of carbon emissions from carbon TEs increases significantly under SSP2-4.5, reflected by higher median cumulative carbon emissions and zero carbon emissions becoming very unlikely since the 5th percentile is non-zero after 2050 (Fig. 15). Carbon emissions nearly as high as under SSP5-8.5 also become possible under SSP2-4.5, with the 95th percentile reaching a maximum of 454 GtC. Under the high emission scenarios SSP3-7.0 and

SSP5-8.5, such high carbon emissions from carbon TEs become more likely with increasing median cumulative carbon emissions (Fig. 15), but since anthropogenic carbon emissions are increasing even stronger, their relative contribution to the total cumulative carbon emissions decreases (Fig. 16). The 95th percentile of cumulative carbon emissions from carbon TEs only reaches 14% of the cumulative anthropogenic carbon emissions in 2500 under SSP3-7.0, and 9% under SSP5-8.

The carbon emission rates from carbon TEs can reach the same order of magnitude as anthropogenic emissions under SSP2-4.5 and higher emission scenarios, mostly between the end of the 21st century and the middle of the 22nd century (Fig. 16). However, if and when such high emission rates would occur remains highly uncertain, since the median of the carbon emission rates remains much lower than the 95th percentile at all times under those scenarios.

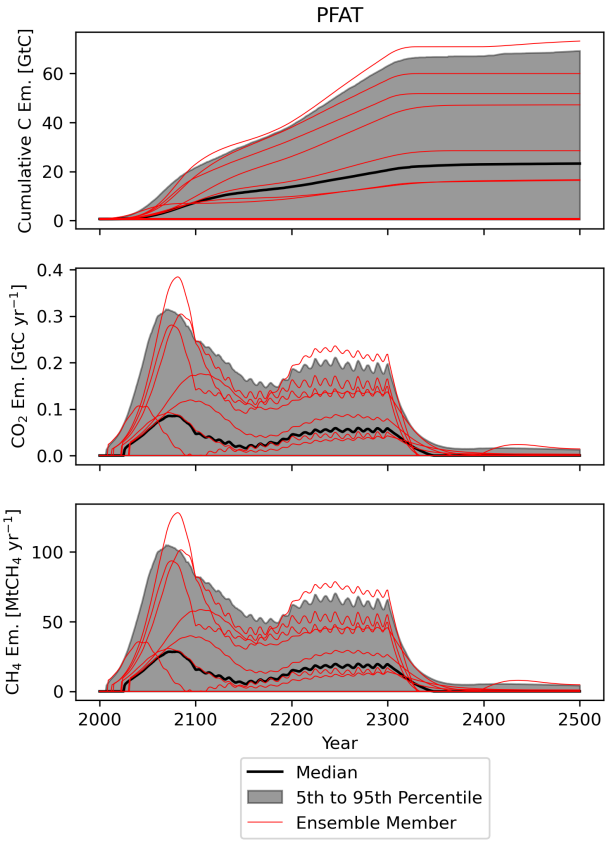


**Figure 17:** Cumulative carbon emissions, $CO_2$ emissions, and $CH_4$ emissions from PFAT under SSP1-1.9. Median and very likely range (5th to 95th percentile) together with randomly chosen ensemble members.

Methane emissions make up for higher shares of the total carbon emissions under low emission scenarios than under high emission scenarios (Tab. 2). Under SSP1-1.9, $CH_4$ emissions make up for 20% of the cumulative carbon emissions in 2500, which decreases to 7.8% under SSP5-8.5. This indicates that under low emission scenarios, predominantly PFAT is triggered which emits 20% of the carbon emissions as methane, whereas under high emission scenarios major parts of the total carbon emissions must come from PFTP and AMAZ which only emit 2.3% and 0% of the carbon as methane respectively.

For a better understanding of the individual contributions of AMAZ, PFAT, and PFTP to the total carbon emissions from carbon TEs, we analyse their behaviour under SSP1-1.9, SSP2-4.5 and SSP5-8.5.

### 3.1.1 SSP1-1.9

Under SSP1-1.9, carbon emissions from PFTP or AMAZ are extremely unlikely, with them being triggered in only 0.9% and 4.4% of the ensemble members respectively. Therefore, the only carbon TE that is likely to emit carbon under SSP1-1.9 is PFAT, which is triggered in 67% of the ensemble members. Hence, we only analyse carbon emissions from PFAT under this scenario.

The increase of cumulative carbon emissions from PFAT happens gradually and mostly between 2050 and 2300 (Fig. 17). The magnitude of the resulting cumulative carbon emissions remains uncertain, with the 95th percentile of the cumulative emissions from PFAT at 68 GtC and the 5th percentile at 0.4 GtC in 2500. Emissions of $CO_2$ and $CH_4$ follow the exact same shape, as they are both defined as fractions of the total carbon emissions (Sec. 2.3). They generally peak around 2070, followed by partial decline and remain roughly constant between 2150 and 2300 before they decline completely (Fig. 17). The smoothness of carbon emissions from PFAT is consistent with the findings of Armstrong McKay et al. (2022), who classify PFAT as a linear feedback to GMST. The maximum anthropogenic emission rates under SSP1-1.9 of 10.8 GtC $yr^{-1}$ of $CO_2$ and 388 $MtCH_4$ $yr^{-1}$, are well above the emissions from PFAT, only reaching 0.3 GtC $yr^{-1}$ and 105 $MtCH_4$ $yr^{-1}$ at the maximum of the 95th percentile. Even though individual ensemble members produce higher carbon emission rates from PFAT, they are not significantly exceeding the 95th percentile. The oscillations of both $CH_4$ and $CO_2$ emissions from PFAT on decadal timescales are induced by the oscillations of GMST in FaIR, due to variations in solar and volcanic forcing that are prescribed externally (Fig. 14).

### 3.1.2 SSP2-4.5

Tipping of PFTP and AMAZ becomes more likely under SSP2-4.5, with them being triggered in 38% and 55% of the ensemble members respectively, while tipping of PFAT becomes virtually certain, occurring in 99% of the ensemble members. Therefore, we analyse carbon emissions from all three TEs.

Our results reflect the finding of (Armstrong McKay et al., 2022) that PFTP causes the highest cumulative carbon emissions of all three carbon TEs in case of tipping, with the 95th percentiles reaching 232 GtC, 71 GtC, and 151 GtC in 2500 for PFTP, AMAZ, and PFAT respectively (Fig. 18). However, tipping of PFTP remains the exception under SSP2-4.5, which is resembled by the median of cumulative carbon emissions from PFTP staying below 1.5 GtC. As for PFAT, the $CO_2$ and $CH_4$ emissions from PFTP follow by definition the same shape, since they are defined as fractions of the total carbon emissions (Sec. 2.3). As expected

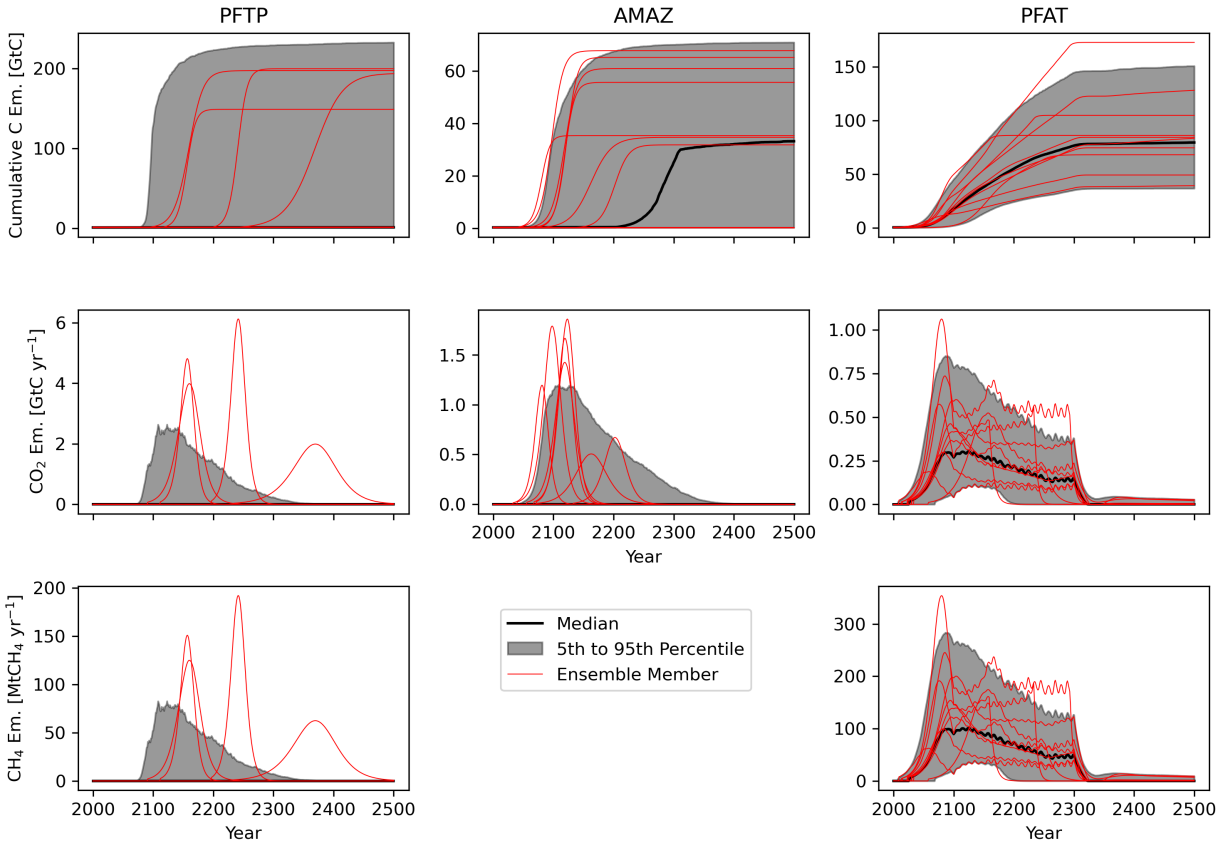


**Figure 18:** Cumulative carbon emissions, $CO_2$ emissions, and $CH_4$ emissions from PFTP, AMAZ and PFAT under SSP2-4.5. Median and very likely range (5th to 95th percentile) together with randomly chosen ensemble members.

from the low median of cumulative carbon emissions, the median and the 5th percentile of $CO_2$ and $CH_4$ emissions from PFTP stay close to zero (Fig. 18). The highest potential for emissions of $CO_2$ and $CH_4$ from PFTP is between 2100 and 2300, as indicated by the 95th percentiles. The randomly chosen ensemble members that feature tipping of PFTP under SSP2-4.5 depict that emission rates can peak at very different magnitudes and times. This behaviour stems from different values of threshold temperature, timescale, and impact of PFTP being used for each ensemble member and is analysed in more detail for SSP5-8.5.

The fact that triggering of AMAZ happens in more than half of the ensemble members under SSP2-4.5 results in relatively high confidence about the occurrence of carbon emissions from AMAZ, with the median of cumulative carbon emissions starting to rise around 2300, reaching 33 GtC in 2500 (Fig. 18). However, the timing of the emissions remains uncertain, as depicted by the median of $CO_2$ emissions, which stays close to zero. Consistent with the lower threshold temperatures of AMAZ compared to PFTP, emissions from AMAZ have the potential to occur earlier, with the 95th percentile of $CO_2$ emissions increasing around 2080.

As for PFTP, the $CO_2$ emissions seem to occur as peaks with different magnitude and with uncertain timing. However, the maximum emissions rates remain much lower than for PFTP.

Higher values for all three percentiles of cumulative carbon emissions from PFAT are reached under SSP2-4.5 compared to SSP1-1.9 (compare Fig. 18 and Fig. 17). Even the 5th percentile is non-zero and reaches 37 GtC in 2500, which is higher than the median under SSP1-1.9. The median of cumulative carbon emissions from PFAT reaches 80 GtC in 2500 under SSP2-4.5. On the one hand, this difference is caused by PFAT being triggered in more ensemble members under SSP2-4.5, on the other hand, also higher temperatures are reached under this scenario, causing higher cumulative carbon emissions from PFAT (Fig. 14). The general behaviour of $CO_2$ and $CH_4$ emissions from PFAT remains more gradual compared to PFTP and AMAZ, with carbon being released over longer timescales in all individual ensemble members (Fig. 18).

The uncertainties in the response of the individual carbon TEs explain the uncertainties in the sum of their emissions that is discussed above. The emission peaks with uncertain timing and magnitude from AMAZ and PFTP result in high values of the 95th percentile of carbon emissions from all carbon TEs under SSP2-4.5 while the median stays low (Fig. 15). The large discrepancy between the median and the 95th percentile of cumulative carbon emissions from all carbon TEs is mainly caused by the uncertain response of PFTP under SSP2-4.5, as it is still about as likely as not to be triggered but causes high carbon emissions in the case of tipping. Generally, as soon as its tipping becomes possible, the behaviour of PFTP is most important out of all three carbon TEs for the total carbon emissions from carbon TEs since PFTP has the potential to cause the highest cumulative carbon emissions and the highest emission rates, due to its high impacts and short timescales compared to the other two carbon TEs (Tab. 1).

### 3.1.3 SSP5-8.5

Under SSP5-8.5, tipping of AMAZ and PFTP becomes extremely likely, with each of them being triggered in 98% of the ensemble members, while tipping of PFAT becomes virtually certain as it is triggered in all ensemble members.

The high confidence in the tipping of PFTP under SSP5-8.5 is reflected by the 5th percentile of cumulative carbon emissions from PFTP, which strongly increases between 2160 and 2285, followed by a more gradual increase until 2500, reaching 129 GtC, while the median and the 95th percentile reach 186 GtC and 244 GtC in 2500 respectively (Fig. 19). Compared to SSP2-4.5, carbon emissions from PFTP occur more early under SSP5-8.5, with the highest potential for them to occur between 2050 and 2250, as indicated by the 95th percentiles of

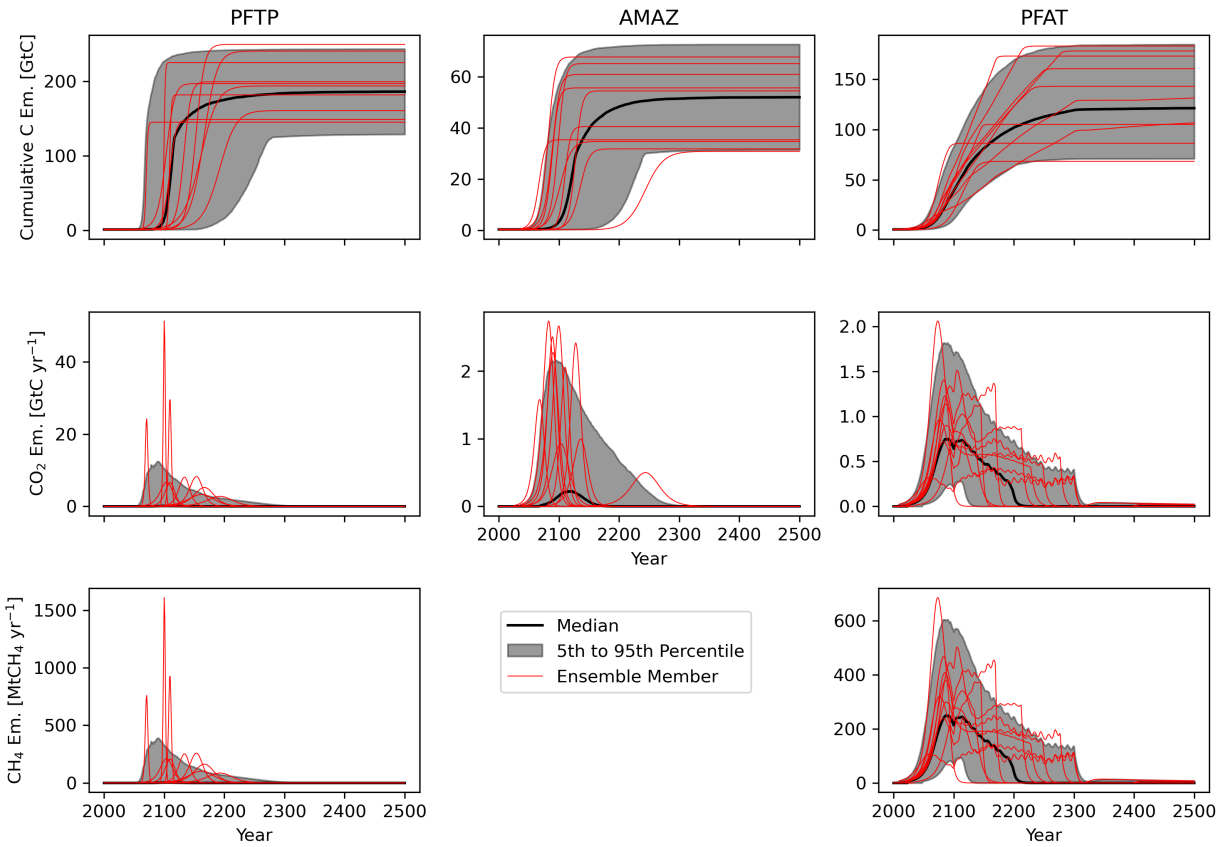


**Figure 19:** Cumulative carbon emissions, $CO_2$ emissions, and $CH_4$ emissions from PFTP, AMAZ and PFAT under SSP5-8.5. Median and very likely range (5th to 95th percentile) together with randomly chosen ensemble members.

$CO_2$ and $CH_4$ emissions. Despite the high confidence in the occurrence of carbon emissions from PFTP, their timing remains uncertain as indicated by the medians of $CO_2$ and $CH_4$ emissions, which remain near zero at all times. Some randomly chosen ensemble members that have not been triggered under SSP2-4.5 feature much higher emission rates of up to 50 GtC $yr^{-1}$ of $CO_2$, that are by far exceeding the 95th percentile of $CO_2$ emissions from PFTP.

For carbon emissions from AMAZ under SSP5-8.5, we find a behaviour comparable to PFTP with high confidence in the occurrence of carbon emissions from AMAZ, reflected by the 5th percentile and the median reaching 32 GtC and 52 GtC in 2500, while the 95th percentile reaches 73 GtC (Fig. 19). However, different to PFTP, there is more certainty about the timing of $CO_2$ emissions, as they seem to cluster around 2120, where the median of $CO_2$ emissions reaches maximum values of 0.22 GtC $yr^{-1}$. This increase in the median seems to be caused by overlapping emission peaks of the ensemble members, as indicated by the randomly chosen ensemble members. Given that the range of possible threshold temperatures is larger

for AMAZ compared to PFTP, this overlap must be caused by comparably longer timescales of AMAZ (Tab. 1). Further analysis of the emission peaks from PFTP and AMAZ is given below.

As for SSP2-4.5, there is high confidence in the occurrence of carbon emissions from PFAT under SSP5-8.5, with the 5th percentile and the median of cumulative emissions reaching 71 GtC and 121 GtC in 2500, while the 95th percentile reaches 185 GtC (Fig. 19). These estimates are much higher than for SSP2-4.5, which can be explained by the feedback of PFAT being temperature dependent and higher temperatures are reached under SSP5-8.5 (Fig. 14). Most ensemble members predict that cumulative carbon emissions from PFAT reach their maximum before 2300, which is reflected by all three percentiles showing nearly no increase after that time, and only two of the randomly picked ensemble members featuring an increase of cumulative carbon emissions from PFAT after 2300 (Fig. 19). Consistent with the maximum impact from PFAT being reached mostly before 2300 under SSP5-8.5, $CO_2$ and $CH_4$ emissions are higher and occur more early compared to SSP2-4.5 but do also fade out earlier, with the median of $CO_2$ emissions reaching zero already in 2230 (compare Fig. 18 and Fig. 19).

The behaviour of the total carbon emissions from the carbon TEs under SSP5-8.5 depicted in Fig. 15 can again be explained by analysing the carbon emissions from the individual carbon TEs. The decreased uncertainty in the magnitude of cumulative carbon emissions from all three carbon TEs compared to SSP2-4.5 can be linked to increased confidence in the occurrence of carbon emissions from PFTP and AMAZ. The uncertainty about the magnitude and timing of carbon emissions from all carbon TEs is explained by the emissions peaks from PFTP and AMAZ.

We analyse the entire coupled ensemble under SSP5-8.5 to gain a better understanding of the maximum $CO_2$ and $CH_4$ emission rates from the carbon TEs that are possible. The $CO_2$ and $CH_4$ emission rates from PFTP have the potential to be around two and three times higher than the respective maximum anthropogenic emissions under SSP5-8.5 (Tab. 3), while the maximum $CO_2$ emission rates from PFAT and AMAZ remain one magnitude lower than the maximum anthropogenic emissions. Nevertheless, due to the comparably large fraction of $CH_4$ emissions of the total carbon emissions from PFAT (20%), maximum $CH_4$ emission rates from PFAT are almost as high as those from PFTP. However, the ensemble means of the maximum $CO_2$ and $CH_4$ emission rates from the carbon TEs are much lower. Only the average peak emissions of $CO_2$ from PFTP are within the same order of magnitude as the anthropogenic maximum $CO_2$ emission rates, while the average peak $CO_2$ emissions from PFAT and AMAZ remain two magnitudes lower. Average peak emissions of $CH_4$ from PFAT

| Source | Max. $CO_2$ Ems (GtC $yr^{-1}$) | Max. $CH_4$ Ems ($MtCH_4$ $yr^{-1}$) | Year of Max. $CO_2$ Ems |
|---|---|---|---|
| SSP | 35.6 | 598 | 2090 |
| PFTP | 14.1 (0.8 – 60) | 448 (6.5 – 1883) | 2127 (2045 – 2488) |
| AMAZ | 1.7 (0.3 – 5.24) | – | 2132 (2045 – 2472) |
| PFAT | 1.2 (0.3 – 4.25) | 408 (84 – 1512) | 2098 (2046 – 2300) |

**Table 3:** Magnitude and timing of maximum $CO_2$ and $CH_4$ emissions under SSP5-8.5 from the SSP scenario and from all three carbon TEs. For the carbon TEs, the mean estimate from the coupled ensemble is given together with the maximum and the minimum value (written as: mean (min—max)), excluding ensemble members in which the respective TE is not triggered.

and PFTP are only slightly lower than the maximum anthropogenic $CH_4$ emission rates. The timing of the maximum emission rates from carbon TEs remains highly uncertain, but there seems to be clustering of maximum emissions from all three carbon TEs around the beginning of the 22nd century.

## 3.2 Atmospheric Concentrations of Carbon Dioxide and Methane

The carbon emissions from the carbon TEs discussed in the sections above result into generally higher atmospheric concentrations of $CO_2$ and $CH_4$ (Fig. 20). While the differences between the $CO_2$ concentrations of the coupled and the uncoupled ensemble generally increase over time, $CH_4$ concentrations of the coupled ensemble return to the concentrations of the uncoupled ensemble around 2350 under all SSPs. This can be explained by carbon emissions from the carbon TEs returning to zero around that time (Fig. 15) and the short atmospheric lifetime of $CH_4$ compared to $CO_2$ (Smith et al., 2021).

Another notable difference between the two GHGs is that the $CH_4$ increase due to carbon emissions from carbon TEs is more significant than the $CO_2$ increase, with the median and for SSP2-4.5, SSP3-7.0, and SSP5-8.5 even the 5th percentile of $CH_4$ concentrations from the coupled ensemble lying above the 95th percentile of the uncoupled ensemble (Fig. 20). Under SSP3-7.0 and SSP5-8.5, the maximum atmospheric $CH_4$ concentrations are almost doubled by carbon TEs. On the contrary, the median and the 5th percentile of $CO_2$ concentrations from the coupled ensemble are always within the 5th to 95th percentile range of the uncoupled ensemble.

That high cumulative carbon emissions from carbon TEs become possible even under low emission SSPs, but only become common under high emissions SSPs, is reflected by the atmospheric $CO_2$ concentrations. Especially under SSP1-1.9, SSP1-2.6 and SSP2-4.5 the distributions of atmospheric $CO_2$ concentrations are skewed towards higher values, with

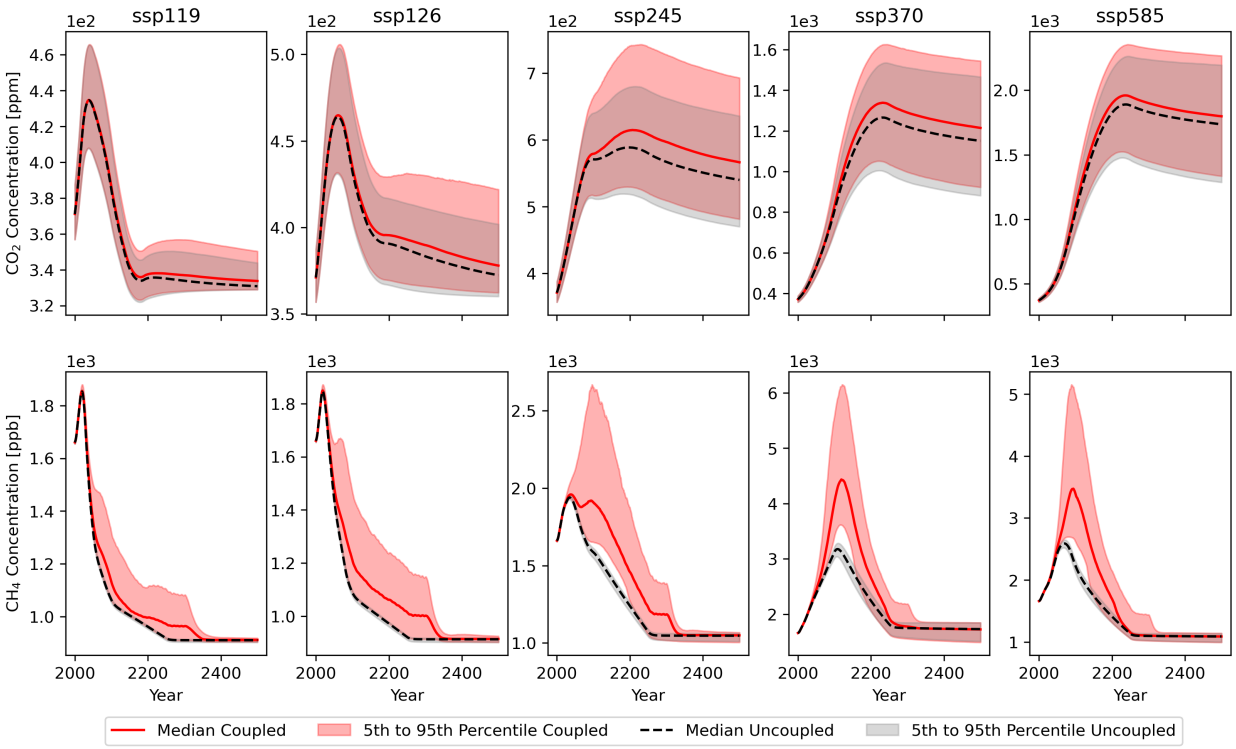


**Figure 20:** Atmospheric concentrations of $CO_2$ and $CH_4$ of the coupled and the uncoupled model ensemble for the Tier1 SSPs.

deviations between the percentiles from both ensembles increasing towards the 95th percentile (Fig. 20).

Consistent with the timing of the carbon emissions from the carbon TEs (Fig. 15) the atmospheric concentrations of $CO_2$ and $CH_4$ from the coupled ensemble start to exceed the concentrations from the uncoupled ensemble earlier under SSPs with higher anthropogenic carbon emissions (Fig. 20). As the differences in atmospheric GHG concentrations between the coupled and the uncoupled ensemble are directly resulting into GMST differences, we limit the more detailed analysis to the inspection of GMST (Sec. 3.3).

## 3.3 Temperature Impact of Carbon Tipping Elements

The carbon TEs are causing an increase in global warming (Fig. 21). Under the low emission scenarios SSP1-1.9 and SSP1-2.6, high temperature increases from carbon TEs are possible but less common, with the temperature distributions skewed towards higher values. No temperature increase from carbon TEs remains possible under those scenarios, as it is still within the very likely range (Tab. 2). The median temperature increase from carbon TEs also remains relatively small, reaching maximum values of 0.05°C and 0.1°C in 2300 under

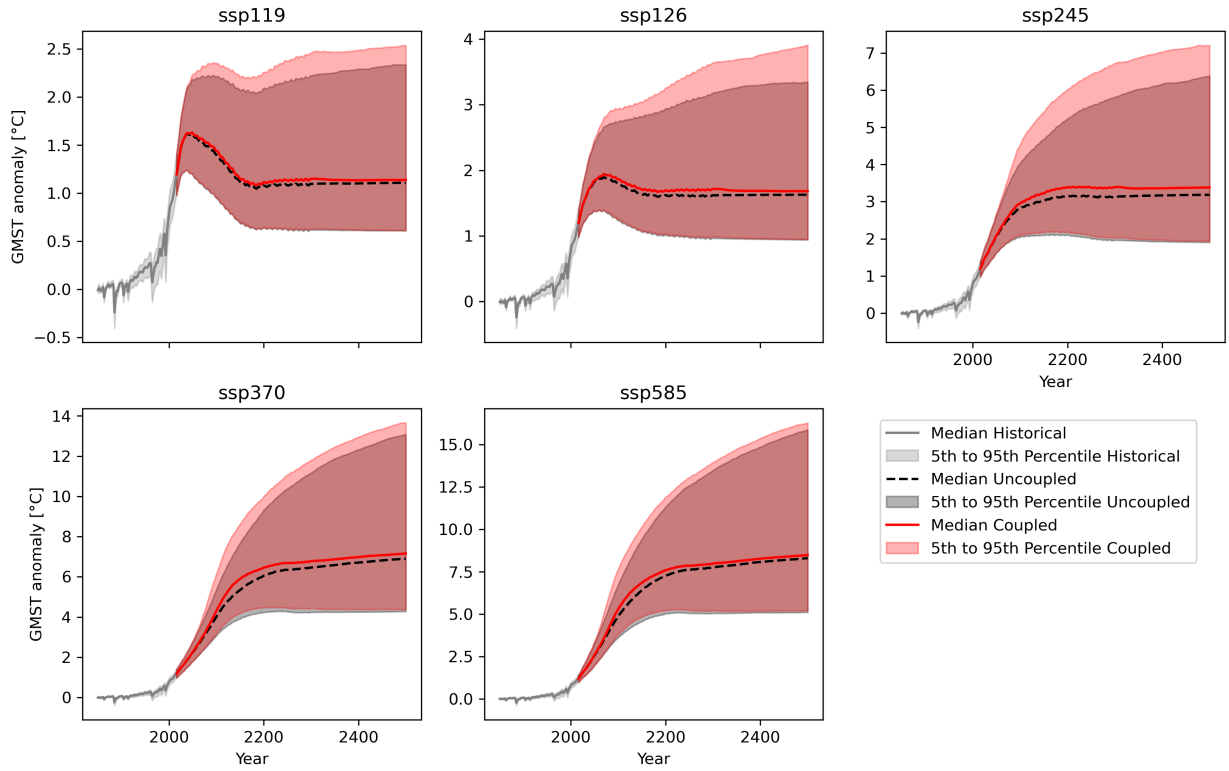


**Figure 21:** GMST relative to the 1850-1900 period of the coupled and the uncoupled ensemble for the Tier1 SSPs, together with the historical evolution.

SSP1-1.9 and SSP1-2.6 respectively. However, the upper end of the very likely range of the temperature increase from carbon TEs reaches maxima of 0.29°C in 2300 under SSP1-1.9 and 0.53°C in 2500 under SSP1-2.6, which would mean a 26% and 32% temperature increase respectively compared to the median of the uncoupled ensemble.

The highest long-term temperature increase from carbon TEs becomes possible under SSP2-4.5, with the upper end of the very likely range reaching 0.91°C in 2500 (Tab. 2), which constitutes a temperature increase of 29% compared to the median of the uncoupled ensemble. The temperature distribution is also skewed towards higher values by the impact of carbon TEs under SSP2-4.5 (Fig. 21), however high temperature increases become more common, as reflected by the median temperature increase, which reaches its maximum of 0.22°C in 2300 (Tab. 2).

High temperature impacts from carbon TEs become even more common under SSP3-7.0 and SSP5-8.5, which is indicated by the median and the 5th percentile of the temperature increase being higher than under SSP2-4.5 (Tab. 2). Therefore, the temperature distributions are less skewed but rather entirely shifted towards higher temperatures by carbon TEs (Fig. 21).

The highest short-term temperature increase from carbon TEs becomes possible under the

| Scenario | Year | 5th [°C] | 50th [°C] | 95th [°C] |
|---|---|---|---|---|
| SSP1-1.9 | 2100 | $1.018 \pm 0.007$, 1.013 | $1.489 \pm 0.007$, 1.452 | $2.356 \pm 0.022$, 2.217 |
| SSP1-1.9 | 2300 | $0.703 \pm 0.005$, 0.7 | $1.196 \pm 0.007$, 1.147 | $2.483 \pm 0.034$, 2.21 |
| SSP2-4.5 | 2100 | $2.138 \pm 0.015$, 2.102 | $2.995 \pm 0.011$, 2.869 | $4.539 \pm 0.023$, 4.057 |
| SSP2-4.5 | 2300 | $2.096 \pm 0.016$, 2.033 | $3.438 \pm 0.019$, 3.189 | $6.737 \pm 0.063$, 5.79 |

**Table 4:** Percentiles of the distributions of GMST relative to the 1850-1900 period from the coupled ensemble (mean ± standard deviation) and the uncoupled ensemble (single value after comma) in 2100 and 2300 corresponding to Fig. 22 and Fig. 23.

high emissions scenarios SSP3-7.0 and SSP5-8.5, with the upper end of the very likely range reaching 0.94°C and 1.11°C in 2100 under SSP3-70 and SSP5-8.5 respectively. This can be linked to high $CH_4$ emissions from fast PFAT degradation due to rapidly increasing temperatures (Fig. 19), which leads to peaks in the atmospheric $CH_4$ concentration anomaly around 2100 (Fig. 20). However, in agreement with atmospheric $CH_4$ concentrations, this temperature increase is of limited duration and the upper end of the very likely range decreases after 2100 under both SSP3-7.0 and SSP-8.5, reaching 0.63°C and 0.47°C respectively in 2500 (Tab. 2). Compared to the median temperature from the uncoupled ensemble, this only constitutes a temperature increase of 9% for SSP3-7.0 and 6% for SSP5-8.5. The fact that the maximum temperature increase from carbon TEs is lower under high emission scenarios than under SSP2-4.5 at the end of the model period despite higher cumulative carbon emissions (Tab.2) and atmospheric $CO_2$ concentrations (Fig. 20) needs further investigation. An explanation for this behaviour is the implementation of the forcing relationship translating atmospheric $CO_2$ and $CH_4$ concentrations to radiative forcing in FaIR. It is approximated by a logarithmic and a square-root term for $CO_2$ and by a square-root term for $CH_4$, meaning that the effect of additional atmospheric concentrations of both GHGs on GMST is decreasing for higher atmospheric concentration levels (Sec. 2.2.2).

The temperature increase from carbon TEs occurs earlier under high emission scenarios (Tab. 2), which can be explained by threshold temperatures of the carbon TEs being crossed earlier under those scenarios, as the general temperature increase is faster (Fig. 21). Interestingly, the median temperature increase from carbon TEs is declining towards the end of the model period under all SSPs (Tab. 2). This can be linked to the decreasing atmospheric methane concentrations (Fig. 20).

### 3.3.1 Temperature Distributions in 2100 and 2300

To investigate the shift in the temperature distribution caused by carbon TEs, we create nine additional coupled ensembles to be able to make statements about the statistical significance

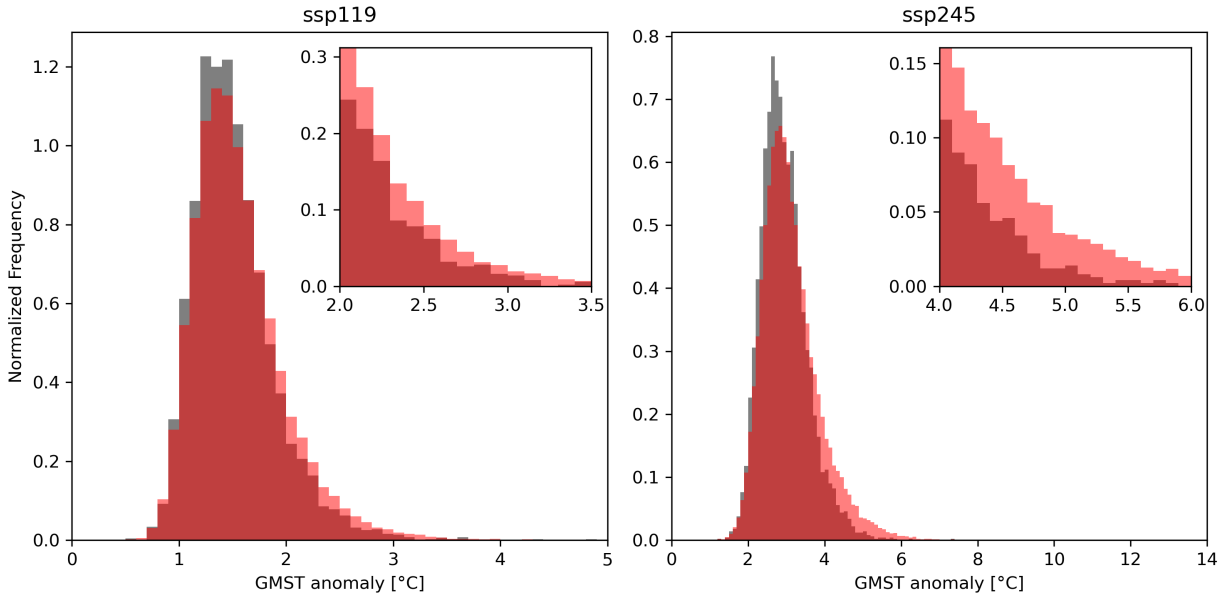


**Figure 22:** Distribution of GMST relative to the 1850-1900 period from the coupled and the uncoupled ensemble in 2100. Bins are 0.1°C wide and the frequency is normalized to give 1 for the integral over GMST.

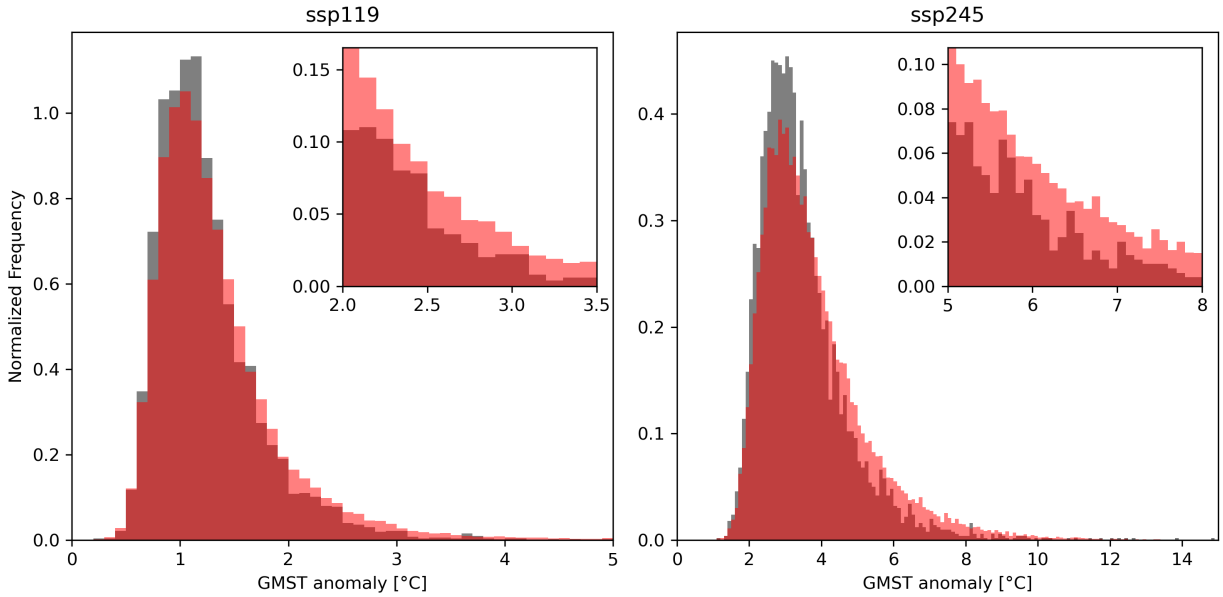


**Figure 23:** Distribution of GMST relative to the 1850-1900 period from the coupled and the uncoupled ensemble in 2300. Bins are 0.1°C wide and the frequency is normalized to give 1 for the integral over GMST.

of our results. As discussed in Sec. 2.4.2, this becomes especially important towards the high end of the uncertainty range, where model results are less robust. We focus on the analysis of the temperature distributions under SSP2-4.5, the scenario that current policies and actions are roughly following (compare Fig. 14 and Climate Action Tracker (2022)), and under SSP1-1.9, the best case scenario. The year 2100 is chosen since it is a crucial time horizon in the climate change debate, but as the major share of carbon emissions from carbon TEs occurs between 2100 and 2300 (Fig. 15), we also investigate the results in 2300. Due to computational constraints, we only store temperature data of the additional ensembles for 2100 and 2300. Hence, those ensembles are not used in other parts of our analysis.

Consistent with the temperature evolution (Fig. 21), high temperatures become more likely if carbon emissions from carbon TEs are included under both SSP1-1.9 and SSP2-4.5 in 2100 and even more pronounced in 2300 (Fig. 22, Fig. 23). This results in skewed temperature distributions towards high temperatures, as low temperatures remain possible within the coupled ensemble under those scenarios. Hence, additional uncertainty is introduced by the carbon TEs, decreasing the confidence in the prediction of GMST. We test the statistical significance of the change in the 5th, the 50th, and the 95th percentile of the temperature distributions due to carbon emissions from carbon TEs under both SSPs in 2100 and 2300 using a Student's $t-$test as described in Sec. 2.6. We find that the increase in all percentiles is statistically significant at a 99% significance level, except for the increase in the 5th percentile under SSP1-1.9 (P-value of 0.02 in 2100, and 0.05 in 2300) (Tab. 4 for mean and standard deviation). The increase in the 5th percentile of GMST due to carbon emissions from carbon TEs is generally smallest, especially under SSP1-1.9, while the highest increase is observed for the 95th percentile, being 0.95°C higher in the coupled ensemble in 2300 under SSP2-4.5.

Additional carbon emissions from the carbon TEs cause higher probabilities for the exceedance of temperature targets. The probability of exceeding 2°C under SSP1-1.9 is increased from 9.86% to $13.5 \pm 0.39$% (mean $\pm$ standard deviation) in 2100 and from 7.32% to $11 \pm 0.37$% in 2300. Under SSP2-4.5, the probability of exceeding 4°C is increased from 5.6% to $11.7 \pm 0.26$% in 2100 and from 24.14% to $33.92 \pm 0.49$% in 2300. All probability increases are statistically significant at a 99% significance level according to the Student's $t-$test (Sec. 2.6).

### 3.3.2 Transient Climate Response to Cumulative Emissions

In this section, we analyse if the carbon emissions from the carbon TEs have the potential to disrupt the near-linear relationship between cumulative anthropogenic $CO_2$ emissions and GMST, which has again been identified with high confidence by the latest IPCC report (IPCC, 2021) and led to the concept of the TCRE. We limit this analysis to SSP2-4.5, SSP3-7.0, and

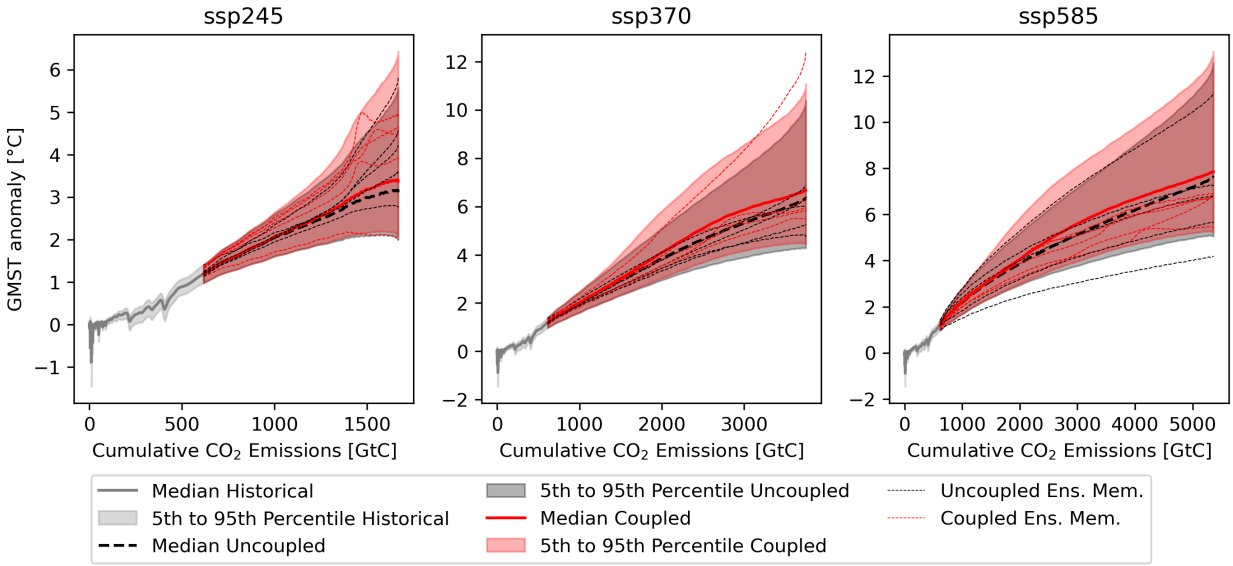


**Figure 24:** GMST relative to the 1850-1900 period plotted against cumulative anthropogenic $CO_2$ emissions for the coupled and the uncoupled ensemble, together with the historical evolution. The thin dotted lines represent random ensemble members from the coupled ensemble (red) and the uncoupled ensemble (black). Values of GMST anomalies and cumulative emissions until the year 2250 have been used, as anthropogenic carbon emissions are close to zero afterwards (Fig. 16).

SSP5-8.5, as SSP1-1.9 and SSP1-2.6 include negative carbon emissions from 2068 and 2076 respectively onwards (Fig. 16), which do not allow for the application of the TCRE concept at any later times.

The response of GMST to cumulative anthropogenic $CO_2$ emissions is near-linear within the uncoupled ensemble for all three SSPs (Fig. 24). The impact of carbon TEs is not changing this linear behaviour significantly throughout the whole ensemble, as it only slightly skews the distributions of GMST towards higher temperatures, not strong enough to speak of a super-linearity.

However, carbon TEs can lead to local super-linear behaviour of individual ensemble members under SSP2-4.5. Out of the five random members from the coupled ensemble under SSP2-4.5 depicted in Fig. 24, the four with the highest temperatures feature triggering of PFAT and either AMAZ or PFTP or both, whereas only PFAT is triggered in the ensemble member with the lowest temperatures. The former four ensemble members clearly show a local super-linear response of GMST to cumulative anthropogenic $CO_2$ emissions around 1400 GtC, while all randomly picked ensemble members of the uncoupled ensemble depict a near-linear response. Especially triggering of PFTP seems to cause those super-linearities, as it is triggered only in the three ensemble members which feature a peak in GMST under SSP2-4.5.

Even though all carbon TEs are triggered for all random members of the coupled ensemble

under SSP3-7.0 and SSP5-8.5, their GMST response to cumulative $CO_2$ emissions remains more gradual. This can be explained by higher anthropogenic $CO_2$ emission rates under these scenarios compared to SSP2-4.5, which are leading to a faster increase in cumulative $CO_2$ emissions (Fig. 16) and therefore decreased gradients in the GMST response to cumulative anthropogenic $CO_2$ emissions.

## 3.4 Probabilities of Triggering Tipping Elements

We now turn to the analysis of the probabilities of triggering the 16 TEs identified by Armstrong McKay et al. (2022) (Tab. 1) under the Tier1 SSPs and how they are influenced by additional carbon emissions from the carbon TEs. To compare those probabilities among the SSPs, we focus on the crossing of 50% probability, where triggering becomes more likely than not, and 95% probability, where triggering becomes extremely likely.

The effect of carbon TEs on the probabilities of triggering under the different SSP scenarios is clearly visible, with triggering getting more likely more early if carbon emissions from carbon TEs are included (Fig. 25, Fig. 26). On average, TEs become more likely than not to be triggered 9.3 years earlier and extremely likely 4.3 years earlier if carbon emissions from carbon TEs are included. This effect becomes more pronounced towards the end of the prediction period, since GMST is generally increasing slower at that time, which means it takes longer for the uncoupled ensemble to reach the same temperatures as the coupled ensemble (Fig. 21). Especially TEs within the cryosphere can become more likely than not to be triggered decades earlier, if carbon emissions from carbon TEs are included. EAIS and AWSI are crossing the 50% probability of triggering 25 years and 19 years earlier under SSP5-8.5 respectively, AWSI is crossing it 47 years earlier under SSP3-7.0, EASB is crossing it 26 years earlier under SSP2-4.5, and GLCR is crossing it 348 years earlier under SSP1-2.6 (Fig. 25). However, there does not seem to be a preference for cryospheric TEs to become extremely likely to be triggered much earlier due to carbon emissions from carbon TEs. The TEs for which we observe triggering becoming extremely likely more than a decade earlier if carbon TEs are included are AMAZ, BORF, and PFTP with 18, 12, and 18 years respectively under SSP5-8.5, and BORF and EASB with 36 and 13 years respectively under SSP3-7.0. As we do not consider any interactions between the TEs apart from the increase in GMST from carbon TEs, the fact that crossing of a certain probability level is reached disproportionally earlier for some TEs if carbon emissions from carbon TEs are included is solely caused by a favourable combination of the threshold temperature distribution and the maximum temperatures reached under the respective SSP and should therefore not be over interpreted.

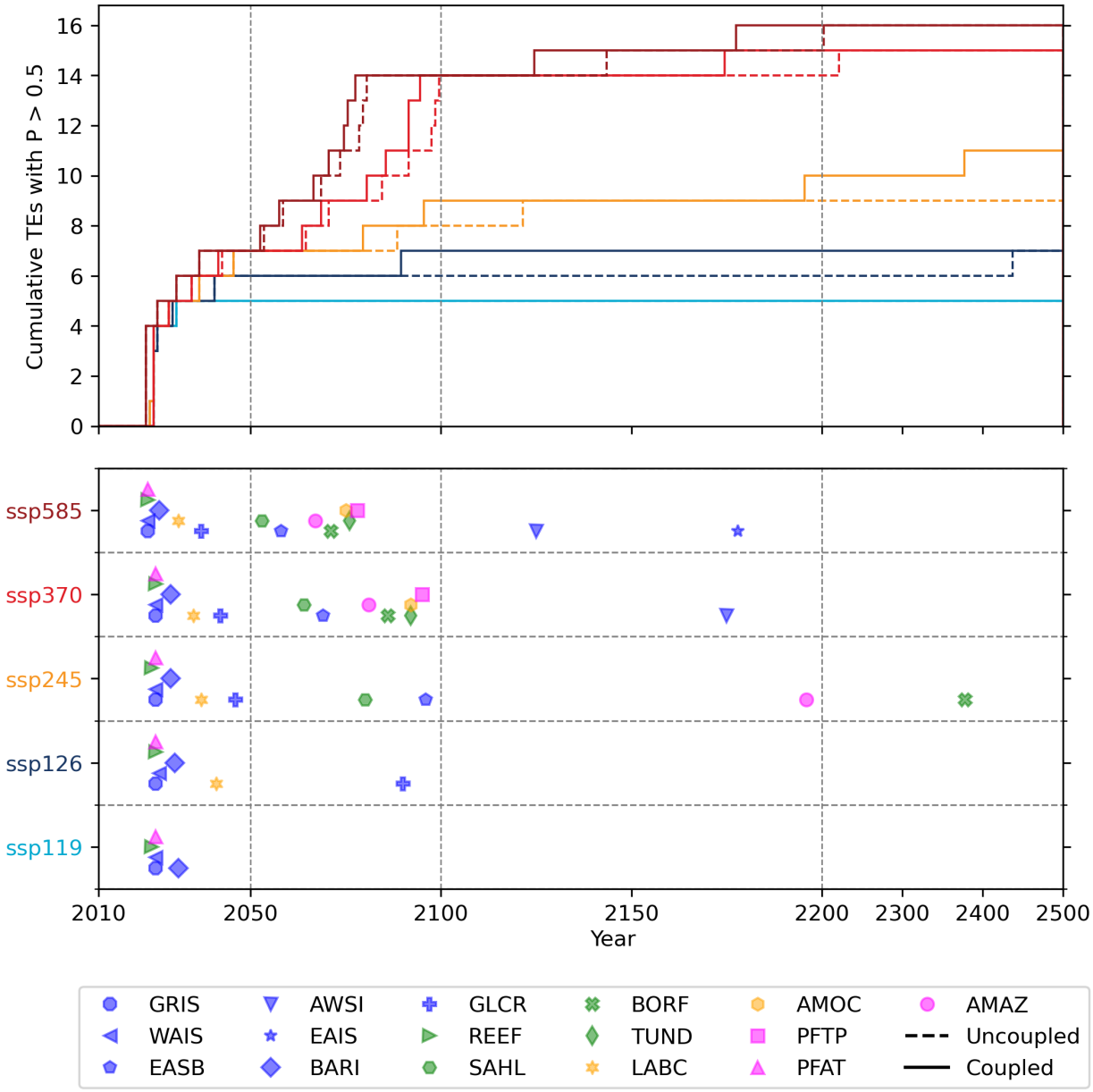


**Figure 25:** Cumulative number of TEs with a more than 50% probability (P) of getting triggered for the Tier1 SSP scenarios from the coupled and the uncoupled ensemble (upper row) and symbols of the triggered TEs corresponding to the increase of cumulative TEs in the coupled ensemble (lower row). Carbon TEs are marked with pink symbols, whereas the other TEs are marked in the colours suggested by Armstrong McKay et al. (2022), with blue for cryosphere, green for biosphere and orange for atmospheric or oceanic circulations.

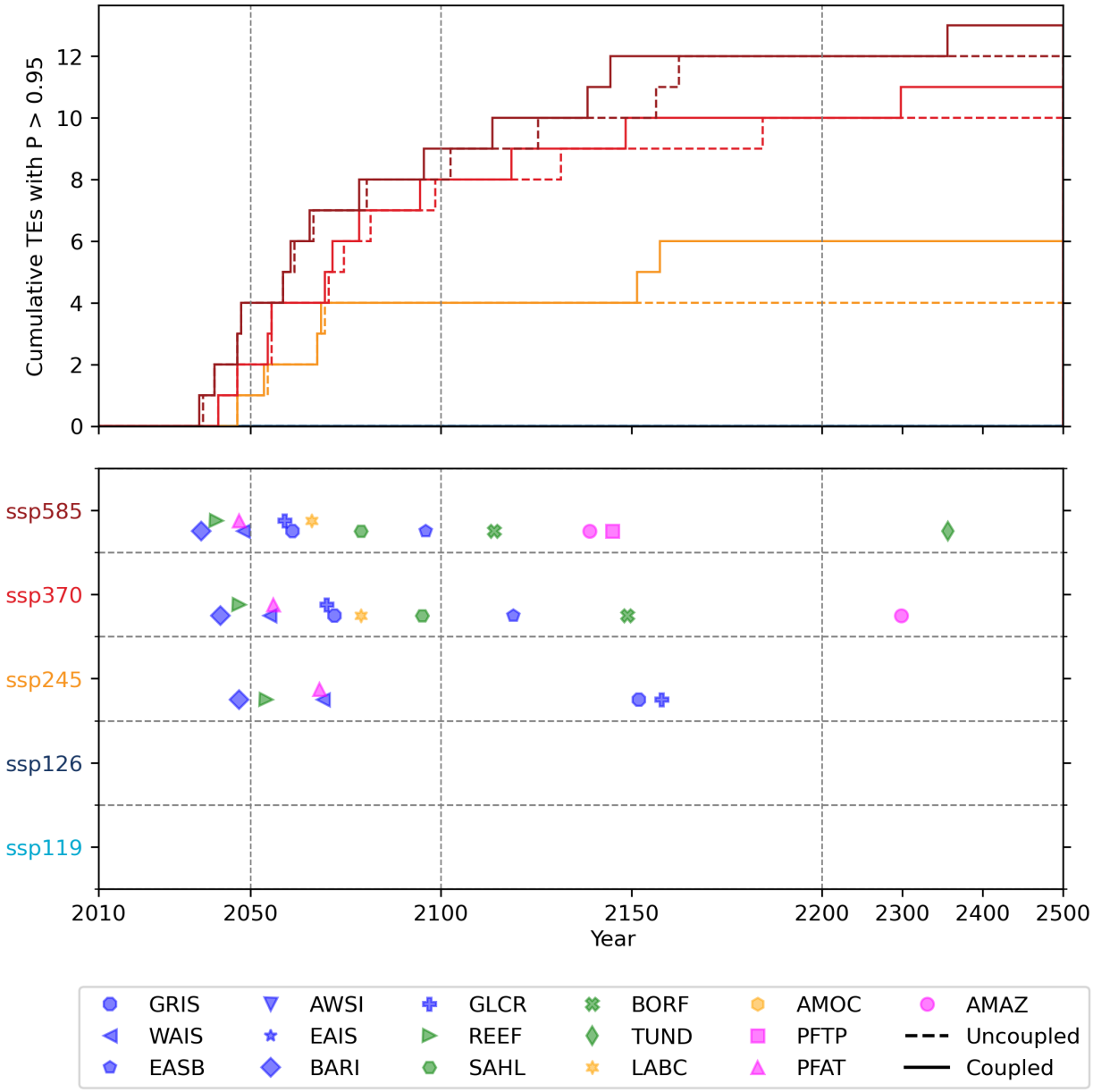


**Figure 26:** Cumulative number of TEs with a more than 95% probability (P) of getting triggered for the Tier1 SSP scenarios from the coupled and the uncoupled ensemble (upper row) and symbols of the triggered TEs corresponding to the increase of cumulative TEs in the coupled ensemble (lower row). Carbon TEs are marked with pink symbols, whereas the other TEs are marked in the colours suggested by Armstrong McKay et al. (2022), with blue for cryosphere, green for biosphere and orange for atmospheric or oceanic circulations.

Even though additional probability of triggering caused by carbon emissions from carbon TEs clearly exists, it remains small compared to the probability of triggering caused by anthropogenic carbon emissions. Only two TEs become more likely than not and four become extremely likely to be triggered in addition to the uncoupled ensemble due to the inclusion of carbon TEs in the sum over all SSPs (Fig. 25, Fig. 26). Carbon TEs do not cause high enough temperature increases to induce rapid triggering of multiple TEs following the tipping of the carbon TEs. Partly, this might be due to the fact that PFTP, which causes the highest carbon emissions of all carbon TEs, is one of the last TEs to be triggered and hence has little potential to cause earlier triggering of other TEs (Fig. 25). Moreover, even if all carbon TEs are extremely likely to be triggered, they only cause an increase of GMST of up to 0.4°C in the median under SSP5-8.5, which is too small to achieve crossing of multiple TEs threshold temperatures (Tab. 2).

For the exceedance of the 50% probability of triggering, we observe clustering of the TEs, which has the potential to occur earlier if carbon emissions from carbon TEs are included. The first cluster consisting of four TEs (GRIS, WAIS, REEF, and PFAT) will become more likely than not to be triggered by 2026, regardless of the emission scenario or whether carbon emissions from carbon TEs are included or not (Fig. 25). Three more TEs forming the second cluster (BARI, LABC and GLCR) exceed the 50% probability of being triggered before 2050 under SSP2-4.5, SSP3-7.0 and SSP5-8.5. This also happens under SSP1-2.6, but much delayed and can be partly avoided under SSP1-1.9 since only BARI becomes more likely to be triggered than not in 2031. The third cluster of seven TEs (SAHL, EASB, AMAZ, BORF, AMOC, TUND, and PFTP) is crossing the 50% probability of triggering between 2050 and 2100 under SSP5-8.5 and SSP3-7.0. This can be partly avoided under SSP2-4.5 with only SAHL and EASB and if carbon emissions from carbon TEs are included also AMAZ and BORF becoming more likely than not to be triggered until 2500. Under SSP1-1.9 and SSP1-2.6, none of the TEs from the third cluster becomes more likely to be triggered than not, independent of carbon emissions from the carbon TEs. The two remaining TEs AWSI and EAIS do also exceed the 50% probability of being triggered under SSP5-8.5 until 2300, while this is only the case for AWSI under SSP3-7.0. Hence, all 16 TEs are more likely than not to be triggered under SSP5-8.5, 15 under SSP3-70, eleven (nine) under SSP2-4.5, seven under SSP2-4.5 and five under SSP1-1.9 including (not including) the carbon emissions from carbon TEs.

As expected, less TEs are exceeding the 95% probability of being triggered than the 50% probability. No TEs become extremely likely to be triggered under SSP1-1.9 and SSP1-2.6, regardless of the carbon emissions from carbon TEs (Fig. 26). Under SSP2-4.5, four TEs (BARI, REEF, PFAT, and WAIS) and, if carbon emissions from the carbon TEs are included,

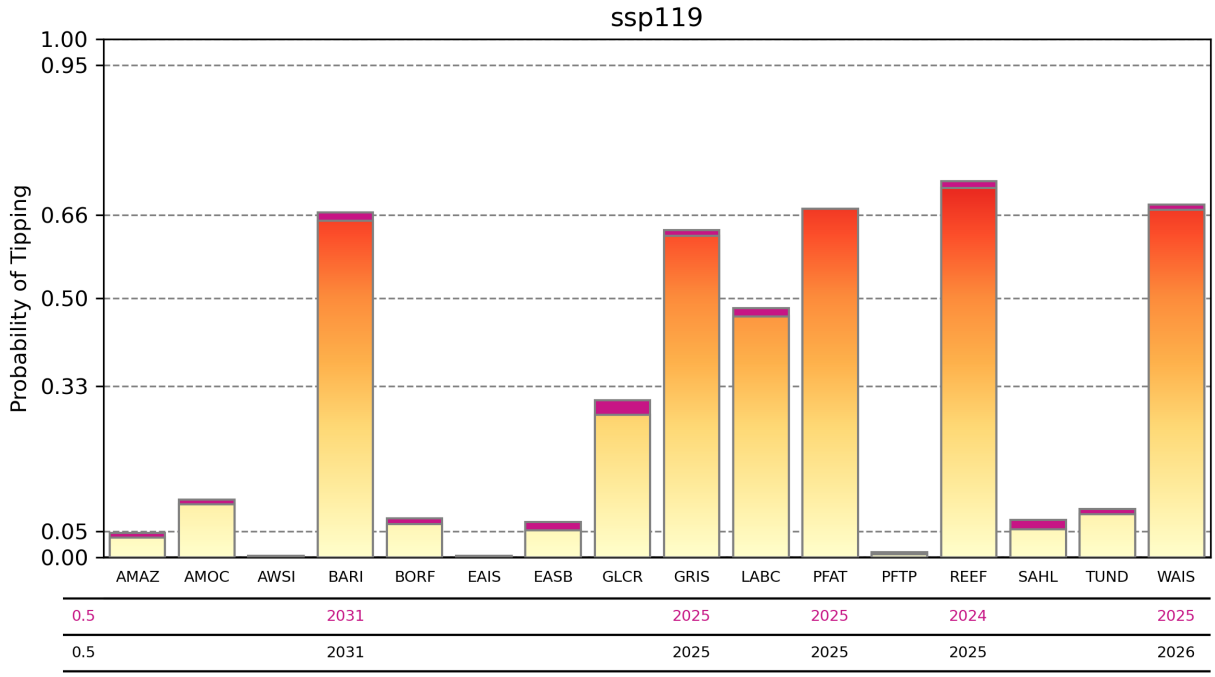


**Figure 27:** Probabilities of triggering the TEs until 2500 under SSP1-1.9. Additional probabilities from the carbon TEs are marked in purple. The table underneath states the years in which the 50% probability is crossed, with purple including carbon emissions from carbon TEs and black not.

GRIS and GLCR become extremely likely to be triggered. In addition, LABC, SAHL, EASB, and BORF and, if carbon emissions from the carbon TEs are included, AMAZ become extremely likely to be triggered under SSP3-7.0. PFTP and, if carbon emissions from carbon TEs are accounted for, TUND only become extremely likely to be triggered under SSP5-8.5. The cumulative TEs reaching probabilities of being triggered above 95% are increasing more smoothly over time, not exhibiting any clustering.

In the next sections, we analyse the probabilities of triggering and the effect of carbon TEs on them in more detail for all Tier1 SSPs. For completeness, we present the probabilities of triggering at the end of our model period in 2500. However, the increase in probabilities of triggering after 2200 is only 2% on average over all SSPs and TEs in the uncoupled ensemble. Therefore, we also provide results of the probabilities of triggering for 2200 in the Appendix.

### 3.4.1 SSP1-1.9

Out of all SSPs, this is the one with the lowest risk of triggering multiple TEs, with 28% probability of triggering on average over all TEs if carbon emissions from carbon TEs are not included. Nevertheless, the five TEs REEF, WAIS, PFAT, GRIS and BARI become more likely than not to be triggered until 2031 under SSP1-1.9, regardless of the temperature

impact from carbon TEs (Fig. 27). Furthermore, REEF, WAIS, PFAT, and, if carbon emissions from carbon TEs are included, BARI even become likely to be triggered. Except for LABC, with a probability of getting triggered just below 50%, all other TEs are unlikely to be triggered under SSP1-1.9. Triggering of AMAZ, AWSI, EAIS and PFTP is even extremely unlikely under SSP1-1.9. EASB and SAHL only remain extremely unlikely to be triggered if carbon emissions from carbon TEs are not included.

The increase in probabilities of triggering caused by carbon TEs remains relatively small under SSP1-1.9, with on average 1.1 percent points (pp) additional probability. The maximum additional probability of getting triggered is found for GLCR with 2.8 pp. The minimum additional probability of getting triggered is found for PFAT with 0 pp. This makes sense, as PFAT is in nearly all cases the first carbon TE to be triggered (compare threshold temperatures in Tab. 1). Hence, no carbon emissions from the carbon TEs are emitted before PFAT is triggered, and the temperatures stay the same in the coupled and the uncoupled ensemble.

The small increase in probabilities of triggering caused by carbon TEs can be explained by the general decease in temperatures under SSP1-1.9 after 2050 (Fig. 21). At this time, the temperature increase from carbon TEs remains small (Tab. 2) and higher temperature increases at later times have less potential to cause maximum temperatures that would lead to additional probability of triggering (Fig. 21).

### 3.4.2 SSP1-2.6

Compared to SSP1-1.9, the risk of triggering multiple TEs is slightly increased under SSP1-2.6, with 38% probability of triggering on average over all TEs if carbon emissions from carbon TEs are not included. The five TEs PFAT, REEF, GRIS, WAIS, and BARI become likely and LABC and GLCR become more likely than not to be triggered, regardless of carbon emissions from carbon TEs (Fig. 28). All other TEs remain unlikely to be triggered, but only AWSI, EAIS and PFTP are extremely unlikely to be triggered under SSP2-4.5.

The increase in probability of triggering caused by carbon emissions from carbon TEs becomes more pronounced compared to SSP1-1.9, with triggering becoming on average 2.3 pp more likely. The maximum increase in probability of getting triggered of 4.5 pp is observed for GLCR, with increases in probability of triggering above 3 pp also found for EASB and SAHL.

The increased additional probability of triggering caused by carbon TEs under SSP1-2.6 compared to SSP1-1.9 can partly be explained by generally higher temperatures, causing higher carbon emissions from carbon TEs (Fig. 21, Tab. 2). In addition, the reduction of

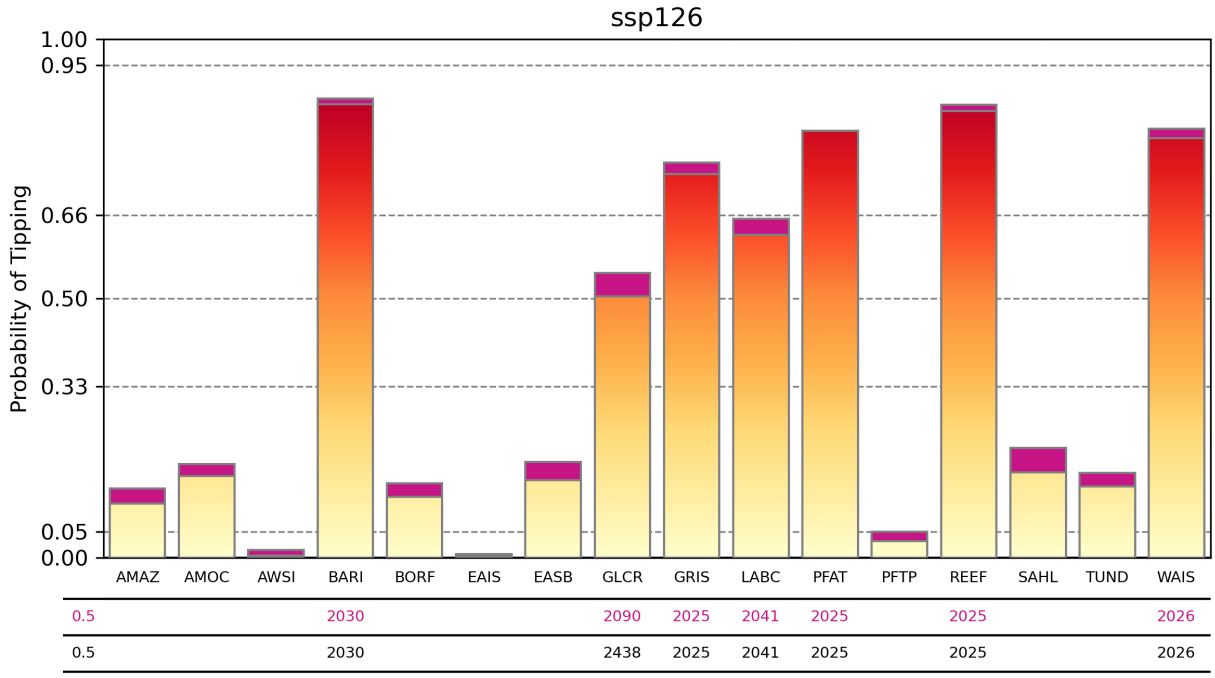


**Figure 28:** Probabilities of triggering the TEs until 2500 under SSP1-2.6. Additional probabilities from the carbon TEs are marked in purple. The table underneath states the years in which the 50% probability is crossed, with purple including carbon emissions from carbon TEs and black not.

GMST due to negative emissions is less drastic under SSP1-2.6, with the peak temperature of the median occurring in 2070 and temperature pathways with steadily increasing temperatures becoming more likely, as indicated by the monotonically increasing 95th percentile of GMST in both ensembles (Fig 21). Therefore, temperature increases from carbon TEs have higher potential to cause maximum temperatures than under SSP1-1.9.

### 3.4.3 SSP2-4.5

Going from SSP1-2.6 to SSP2-4.5 nearly doubles the risk of triggering multiple TEs, with 65% probability of triggering on average over all TEs if carbon emissions from carbon TEs are not included. The four TEs BARI, REEF, PFAT, and WAIS become extremely likely to be triggered under SSP2-4.5, with GRIS and GLCR becoming extremely likely as well if carbon emissions from carbon TEs are included (Fig. 29). SAHL and, if carbon emissions from carbon TEs are included, EASB become likely to be triggered. Additional carbon emissions from carbon TEs also lead to AMAZ and BORF becoming more likely than not to be triggered. Only AWSI, EAIS, and, if carbon emissions from carbon TEs are not accounted, for PFTP remain unlikely to be triggered, as TUND and AMOC are exceeding 33% probability of getting triggered in both ensembles. Triggering of EAIS remains extremely unlikely only if carbon emissions from the carbon TEs are not included.

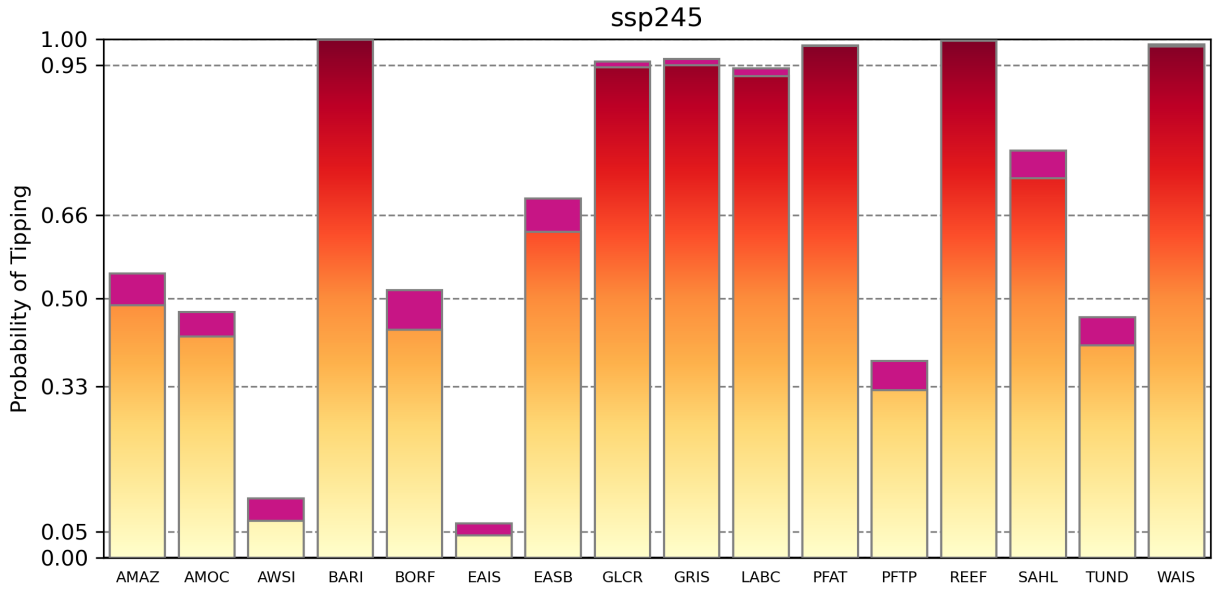


| | | | | | | | | | | | | | | | |
|---|---|---|---|---|---|---|---|---|---|---|---|---|---|---|---|
| 0.5 | 2196 | | | 2029 | 2378 | | 2096 | 2046 | 2025 | 2037 | 2025 | | 2024 | 2080 | | 2025 |
| 0.5 | | | | 2029 | | | 2122 | 2046 | 2025 | 2037 | 2025 | | 2024 | 2089 | | 2025 |
| 0.95 | | | | 2047 | | | | 2158 | 2152 | | 2068 | | 2054 | | | 2069 |
| 0.95 | | | | 2047 | | | | | | | 2068 | | 2055 | | | 2070 |

**Figure 29:** Probabilities of triggering the TEs until 2500 under SSP2-4.5. Additional probabilities from the carbon TEs are marked in purple. The table underneath states the years in which the 50% and the 95% probability are crossed, with purple including carbon emissions from carbon TEs and black not.

The increase in probabilities of triggering caused by carbon emissions from carbon TEs is highest under SSP2-4.5, with 3.3 pp additional probability on average over all TEs. The maximum increase is observed for BORF, with the probability of triggering being 7.6 pp higher if carbon emissions from carbon TEs are included. Increases in the probability of triggering due to additional carbon emissions from carbon TEs above 5 pp are also found for TUND, SAHL, PFTP, EASB, and AMAZ.

That the additional probability of triggering TEs is highest under SSP2-4.5 matches our finding that the highest long-term temperature increase from carbon TEs is possible under this scenario (Tab. 2). Furthermore, GMST is generally increasing over time, which means that emissions from carbon TEs can produce temperature maxima when they occur, which is not the case for lower emission scenarios (Fig. 21). Moreover, there is less potential for increased probabilities of triggering under higher emission scenarios, since probabilities near 100% are often reached even without additional carbon emissions from carbon TEs (see below).

Interestingly, medium probabilities of triggering get amplified stronger by carbon emissions

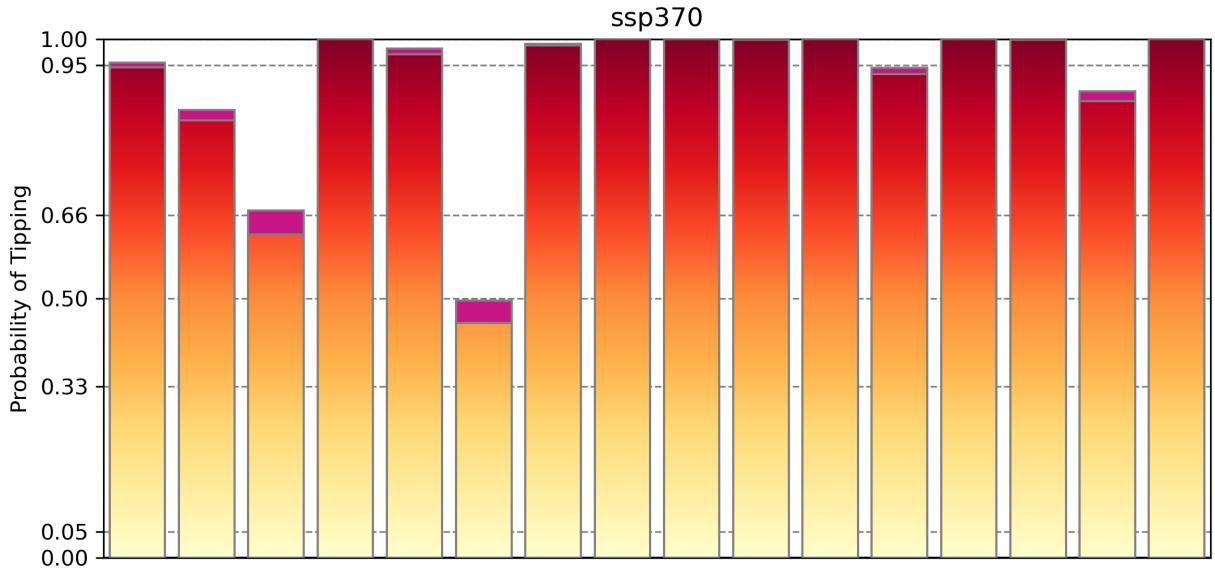


| | | | | | | | | | | | | | | | | |
|---|---|---|---|---|---|---|---|---|---|---|---|---|---|---|---|---|
| 0.5 | 2081 | 2092 | 2175 | 2029 | 2086 | | 2069 | 2042 | 2025 | 2035 | 2025 | 2095 | 2025 | 2064 | 2092 | 2025 |
| 0.5 | 2085 | 2098 | 2222 | 2029 | 2092 | | 2071 | 2043 | 2025 | 2035 | 2025 | 2100 | 2025 | 2065 | 2099 | 2025 |
| 0.95 | 2299 | | | 2042 | 2149 | | 2119 | 2070 | 2072 | 2079 | 2056 | | 2047 | 2095 | | 2055 |
| 0.95 | | | | 2042 | 2185 | | 2132 | 2071 | 2075 | 2082 | 2056 | | 2047 | 2099 | | 2056 |

**Figure 30:** Probabilities of triggering the TEs until 2500 under SSP3-7.0. Additional probabilities from the carbon TEs are marked in purple. The table underneath states the years in which the 50% and the 95% probability are crossed, with purple including carbon emissions from carbon TEs and black not.

from carbon TEs than very high or very low probabilities, which is most clearly visible under SSP2-4.5 (Fig. 29). This behaviour is caused by the mean threshold temperature having the highest probability of getting sampled (Fig. 8). Therefore, the temperature increase from carbon TEs has the highest potential to increase tipping probabilities if the GMST increase stops around the mean threshold temperature of a TEs, where tipping of the respective TE in about half of the ensemble members can be expected.

### 3.4.4 SSP3-7.0

Under this scenario, triggering multiple TEs becomes very likely, with a probability of triggering of 92% on average over all TEs if carbon emissions from carbon TEs are not accounted for. Except for EAIS and, if carbon emissions from carbon TEs are not accounted for, AWSI, all TEs become likely to be triggered under SSP3-7.0, and the ten TEs BARI, REEF, WAIS, PFAT, GLCR, GRIS, LABC, SAHL, EASB, and BORF become extremely likely to be triggered, with AMAZ only becoming extremely likely to be triggered if carbon emissions from carbon TEs are included (Fig. 30). Only EAIS is not becoming more likely

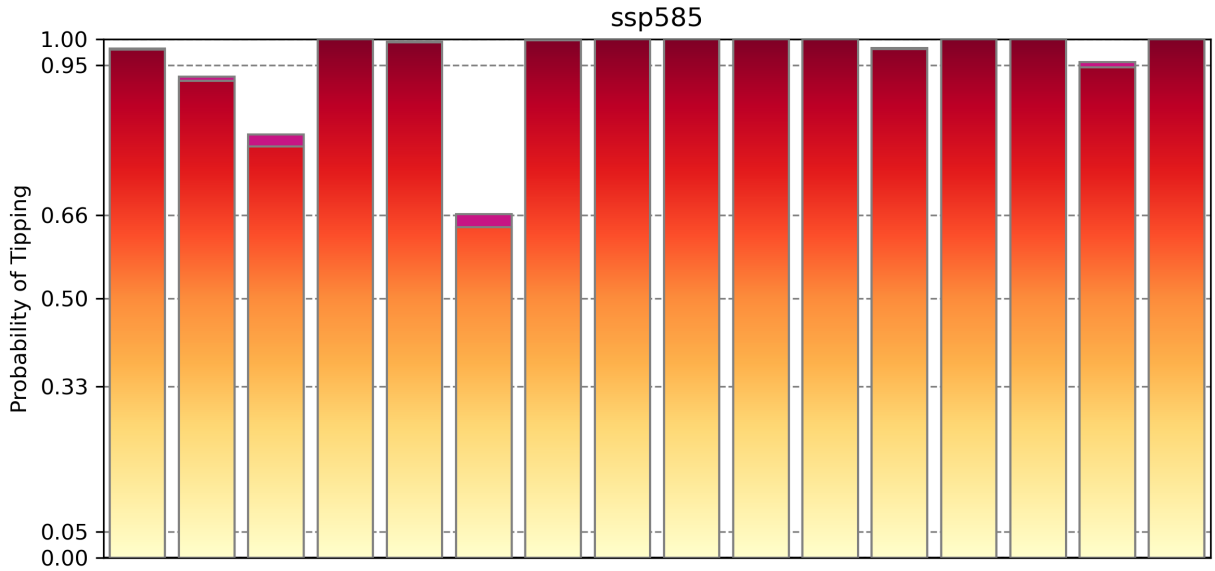


| | | | | | | | | | | | | | | | | |
|---|---|---|---|---|---|---|---|---|---|---|---|---|---|---|---|---|
| 0.5 | 2067 | 2075 | 2125 | 2026 | 2071 | 2178 | 2058 | 2037 | 2023 | 2031 | 2023 | 2078 | 2023 | 2053 | 2076 | 2023 |
| 0.5 | 2069 | 2079 | 2144 | 2026 | 2074 | 2203 | 2059 | 2037 | 2023 | 2031 | 2023 | 2081 | 2023 | 2054 | 2080 | 2023 |
| 0.95 | 2139 | | | 2037 | 2114 | | 2096 | 2059 | 2061 | 2066 | 2047 | 2145 | 2041 | 2079 | 2357 | 2048 |
| 0.95 | 2157 | | | 2038 | 2126 | | 2103 | 2059 | 2062 | 2067 | 2047 | 2163 | 2041 | 2081 | | 2048 |

**Figure 31:** Probabilities of triggering the TEs until 2500 under SSP5-8.5. Additional probabilities from the carbon TEs are marked in purple. The table underneath states the years in which the 50% and the 95% probability are crossed, with purple including carbon emissions from carbon TEs and black not.

to be triggered than not, with its probability of triggering remaining just below 50%.

The additional probability of triggering from carbon TEs is only 1 pp on average over all TEs under SSP3.7.0 since most TEs become extremely likely to be triggered even without considering additional carbon emissions from carbon TEs (Fig. 30). The highest increase in probability of triggering is again found for the TEs with medium tipping probability, namely EAIS and AWSI, with a 4.4 pp and 4.6 pp increase respectively.

### 3.4.5 SSP5-8.5

Triggering of multiple TEs becomes extremely likely under this scenario, since the probability of triggering is 95% on average over all TEs if carbon emissions from carbon TEs are not included. Except for EAIS, all TEs become likely to be triggered under SSP5-8.5 and the twelve TEs AMAZ, BARI, BORF, EASB, GLCR, GRIS, LABC, PFAT, PFTP, REEF, SAHL, and WAIS become extremely likely to be triggered (Fig. 31). If carbon emissions from carbon TEs are included, TUND is also becoming extremely likely to be triggered. The probability of triggering EAIS is remaining just under 66%.

Even though the highest short-term temperature increase from carbon TEs of 1.1°C in 2100 becomes possible under SSP5-8.5 (Tab. 2), the mean additional probability of triggering caused by carbon TEs is smallest out of all SSPs, making triggering on average only 0.44 pp more likely. This is due to rapidly increasing global warming after 2100 (Fig, 21), leading to most TEs becoming extremely likely to tip even without the effect of carbon TEs. The maximum increase in probability of triggering due to carbon emissions from carbon TEs under SSP5-8.5 is found for EAIS, which becomes 2.5 pp more likely to be triggered.

# 4 Discussion

Here we compare our results to the literature to examine whether our model approach is appropriate, to point out differences and similarities compared to previous studies, and to put our results into context to make them more tangible.

## 4.1 Performance of the Carbon Tipping Elements Model

The behaviour of the carbon TEs modelled by CTEM is generally matching the underlying estimates from Armstrong McKay et al. (2022). Threshold temperatures and impacts of all three carbon TEs are sampled directly from the respective probability distributions fitted to those estimates, and do therefore match them by definition (Sec. 2.3). The only parameter of CTEM that needs calibration and is sometimes deviating from those estimates is the timescale of tipping. Especially for PFAT those deviations matter, as carbon is released too late, which leads to a gap between observed and expected cumulative emissions in 2100 (Fig. 6), which is closed until 2300. Therefore, impacts from the carbon TEs within the 21st and the 22nd century might be slightly underestimated, especially the impacts in 2050 that stay very low under all SSPs (Tab. 2). In the detailed inspection of the results from CTEM under SSP1-1.9, SSP2-4.5, and SSP5-8.5, the difference in the nature of the carbon TEs becomes evident, with carbon emissions from PFAT being released gradually, whereas the carbon emissions from AMAZ and PFTP are more abrupt (Fig. 17, 18, and 19). This is in line with PFAT amplifying PFGT, which is a threshold-free feedback to GMST, whereas carbon emissions from AMAZ and PFTP are released independently of GMST once they are triggered (Tab. 1).

## 4.2 Carbon Emissions from Carbon Tipping Elements

The impacts from the carbon TEs estimated in this study remain somewhat speculative, as there is only limited confidence about the actual existence of tipping points within the carbon TEs, with low confidence for PFTP and medium confidence for PFAT and AMAZ (Tab. 1). The distinction between PFGT, PFAT and PFTP made by Armstrong McKay et al. (2022) for permafrost thaw also remains questionable. Most studies, including the latest IPCC report, assume that permafrost thaw can be divided into gradual and abrupt thaw processes, corresponding to PFGT and PFAT, and do not mention permafrost collapse due to compost bomb instabilities (PFTP) (e.g., Canadell et al., 2021; Turetsky et al., 2020; Schuur et al., 2015; Wang et al., 2023). Since PFTP causes the highest carbon emissions out of all three carbon TEs with up to 250 GtC (Tab. 1), there is a good chance that the impact

of tipping elements within the carbon cycle is clearly less severe than found in this study if PFTP does not prove to include a tipping point.

However, additional carbon emissions released by PFGT under continued global warming of up to 260 GtC (Tab. 1) need to be expected, which are not considered in this study. One reason to exclude PFGT is that it is not assumed to include tipping points, but to be a threshold-free feedback to global warming (Armstrong McKay et al., 2022). Furthermore, sophisticated models of PFGT already exist (e.g., Gasser et al., 2018; Burke et al., 2020), hence it would not be appropriate to represent PFGT with a simple conceptual model like CTEM. A reasonable possibility to include PFGT in our analysis would be to use the well known reduced complexity climate model MAGICC (Meinshausen et al., 2011) together with its permafrost submodule (Schneider von Deimling et al., 2012) instead of FaIR. However, this would increase the complexity of our model approach significantly.

It is challenging to compare the carbon emissions from carbon TEs identified by us to other studies, as this is to the best of our knowledge the first study to investigate the impact of all TEs within the carbon cycle. Other studies are only analysing single TEs, e.g., Cox et al. (2004) and Parry et al. (2022) for AMAZ or Schneider von Deimling et al. (2015) and Gasser et al. (2018) for permafrost thaw as a whole. Since the individual carbon emissions from the carbon TEs modelled by CTEM agree with the estimates of Armstrong McKay et al. (2022), we would only reproduce their analysis by comparing our individual carbon emission estimates to the literature. Therefore, we spare this comparison here and give a detailed overview of estimated carbon emissions from the individual carbon TEs in Sec. 1.3. Nevertheless, it must be noted that even though the uncertainty ranges of the carbon impacts identified by Armstrong McKay et al. (2022) based on numerous studies are large (factor two for PFTP and AMAZ, factor three for PFAT), they do not include all estimates from the literature. Especially, the lower bounds of AMAZ and PFTP are questionable. Carbon emissions from the Yedoma region, which make up for the major part of PFTP emissions, of only 23 GtC in 2300 under RCP5-8.5 have been found by an observations-based modelling study (Schneider von Deimling et al., 2015). This is much lower than the minimum carbon emissions of 100 GtC from the Yedoma region assumed by Armstrong McKay et al. (2022), which led to an estimated minimum impact of PFTP of 125 GtC. The minimum impact of 30 GtC for AMAZ might also be too high since no substantial carbon loss from AMAZ is observable in CMIP6 models, even if localized dieback occurs (Parry et al., 2022).

A more novel result from CTEM are the emission rates of the carbon TEs. The extremely high maxima of emission rates from PFTP, with $CO_2$ emissions of up to 60 GtC $yr^{-1}$ (Tab. 3), are most likely unrealistic, since much lower emission rates of only $2 - 2.8$ GtC $yr^{-1}$ were

found by Khvorostyanov et al. (2008). Maximum emission rates from AMAZ are much lower, but with $CO_2$ emissions of up to 5.24 GtC $yr^{-1}$ still substantial. Such high emission rates from PFTP and AMAZ become possible since we assume that timescales and impacts of both TEs are not correlated. Hence, combinations of short timescales and high impacts are possible, which might be unrealistic. Even though the carbon emission rates of PFAT are much smaller, it still has the potential to produce maximum $CH_4$ emissions nearly three times higher than the maximum anthropogenic $CH_4$ emissions (Tab. 3). This is explained by the high share of $CH_4$, which we assume to make up for 20% of the total carbon emissions from PFAT, in line with Turetsky et al. (2020). On the one hand, it is a major limitation of CTEM that it does not account for the temporal variability of the $CH_4$ emission fractions of PFTP and PFAT. On the other hand, we regard the temporal evolution of this fraction as too poorly constrained to be prescribed in CTEM since current model studies are rare and vary greatly (compare Turetsky et al. (2020) and Schneider von Deimling et al. (2015)).

## 4.3 Uncertainties in the Temperature Response

FaIR produces very high GMST anomalies towards the end of the model period, with the 95th percentile reaching 15.8°C in 2500 under SSP5-8.5 in the uncoupled ensemble (Fig. 21). Such high temperature increases are most likely unrealistic and caused by the ECS of FaIR being poorly constrained towards the upper end, with the very likely range reaching 6.6°C whereas the IPCC and CMIP6 models estimate it to reach only 5°C and 5.4°C respectively (Fig. 1).

There is high uncertainty about the magnitude of additional warming from carbon TEs (Tab. 2). For the low to medium emission scenarios (SSP1-1.9 to SSP2-4.5) this uncertainty is mainly caused by the uncertainty about whether carbon TEs are triggered or not. This is especially pronounced under the "middle of the road" scenario SSP2-4.5 where tipping of AMAZ and PFTP is about as likely as not (Fig. 29), with a very likely range of 0.03°C to 0.91°C additional warming from carbon TEs in 2500. Under the high emission scenarios SSP3-7.0 and SSP5-8.5, tipping of all three carbon TEs becomes very or even extremely likely (Fig. 30, Fig. 31). Hence, uncertainties in the additional warming from carbon TEs must be caused by the uncertainty about their impacts in terms of total carbon emissions.

## 4.4 Questioning the Planetary Threshold Hypothesis

Our results do not confirm the hypothesis of a planetary threshold temperature formulated by Steffen et al. (2018). While Steffen et al. (2018) report an additional warming of 0.14°C

$(0.07 - 0.27°C)$ from permafrost thaw and Amazon rainforest dieback in 2100 for a $\sim 2°C$ warming, we find lower warming from the carbon TEs with 0.07°C (0-0.24°C) being reached under SSP1.2.6 in 2100 with a warming of 1.8°C in the median of the uncoupled ensemble. However, those numbers need to be compared carefully since Steffen et al. (2018), unlike us, also consider PFGT, which increases their estimate. Furthermore, we only find a local super-linear responses of GMST to cumulative $CO_2$ emissions for individual ensemble members under SSP2-4.5 and not across the whole ensemble under all SSPs crossing 2°C, which would be expected in case of a planetary threshold (Fig. 24). Partly this can be explained by the large uncertainty in the threshold temperatures of the carbon tipping elements, which do not cluster around a certain value (Tab. 1), hence no synchronous tipping can be expected. However, we do not explicitly include additional carbon feedbacks the planetary threshold hypothesis is based on, namely PFGT, BORF, relative weakening of ocean and land carbon sinks, and increased bacterial respiration in the ocean. Therefore, our study alone cannot disprove the planetary threshold hypothesis, but it does cast doubt on it.

## 4.5 Scientific Context of Probabilities of Triggering Tipping Elements

Our estimates of probabilities of triggering are generally higher than the values reported by Kriegler et al. (2009), which have found much use in the climate tipping points literature (e.g., Lontzek et al. (2015), Cai et al. (2015), Cai et al. (2016)). Ranges of probabilities of triggering are provided for the year 2200 under three warming scenarios: a low temperature corridor comparable to SSP1-1.9, a medium temperature corridor comparable to SSP2-4.5 and a high temperature corridor comparable to SSP3-7.0. For the medium temperature corridor, Cai et al. (2016) infer mean probabilities of triggering from the ranges given in Kriegler et al. (2009) of 22% for AMOC, 52% for GRIS, 34% for WAIS, and 48% for AMAZ, which can be compared to our estimates in 2200 under SSP2-4.5 (without carbon TEs impacts) of 38% for AMOC, 94% for GRIS, 98% for WAIS, and 43% for AMAZ (Fig. 34).

Those deviations can be explained by the new scientific literature being published since Kriegler et al. (2009), which give reason for the threshold temperature estimates from Armstrong McKay et al. (2022) our calculation of triggering probabilities is largely based on. The increased triggering probability for the AMOC can be linked to various studies reporting unrealistic stability of the AMOC in GCMs (e.g., Liu et al. (2017)), together with increasing evidence for the proximity of a tipping point for AMOC (Boers, 2021). New indications for the proximity of a tipping point for GRIS are also derived from observations of ice loss (King et al., 2020; Boers and Rypdal, 2021), with recent modelling studies confirming this (Van Breedam et al., 2020; Robinson et al., 2012). Loss of WAIS is becoming observable

(Shepherd et al., 2019) and a tipping point might already be crossed with several glaciers in the Amundsen Sea currently undergoing MISI (Rignot et al., 2014).

## 4.6 No Tipping Cascades Triggered by Carbon Tipping Elements

Even though we find an increase in the probabilities of triggering caused by the additional carbon emissions from carbon TEs, this impact is not strong enough to trigger any tipping cascades. Additional carbon emissions from carbon TEs only cause existing clusters of TEs to be triggered more early, but are not producing any additional clusters of triggering (Fig. 25). Even under SSP2-4.5, which features the highest long-term increase in temperature of up to 0.91°C due to carbon emissions from carbon TEs, the additional probability of triggering caused by this temperature increase is only 3.3 pp on average and only two TEs become more likely than not to be triggered if this temperature increase is accounted for. Despite our finding that the impact from carbon TEs alone is too small to trigger tipping cascades, tipping cascades might still emerge as major physical interactions between TEs aside from carbon emissions are not accounted for in this study (Wunderling et al., 2021).

## 4.7 Implications of the Triggering Probabilities

As triggering probabilities are increasing strongly with anthropogenic GHG emissions, our results underline the clear urge for emission reduction to avoid climate tipping points also emphasized by earlier studies (e.g., Lenton et al. (2019) and Cai et al. (2015)). However, it might already be too late to opt for emissions pathways that are safe with regard to triggering any TE since triggering of GRIS, PFAT, REEF, WAIS and BARI becomes more likely than not until 2031, regardless of the chosen SSP (Fig. 25).

Therefore, even under SSP1-1.9 drastic impacts from tipping of several TEs must be expected. Dieback of low-latitude coral reefs becomes likely, which would severely impact biodiversity and directly affect the livelihoods of $\sim 500$ million people (Wilkinson, C., 2004) (Fig. 27). Several meters of SLR become possible due to tipping of GRIS and WAIS, which store a SLE of 7.42 m and 4.3 m respectively (Fretwell et al., 2013; Morlighem et al., 2017). Furthermore, permafrost carbon emissions are likely to be amplified by $\sim 50\%$ due to abrupt thaw processes (Armstrong McKay et al., 2022) and winter sea ice in the Barents Sea is likely to be lost, leading to changes in European weather (Smedsrud et al., 2013).

Under SSP1-2.6, warming is limited to just below 2°C (Fig. 14), which can be achieved if current climate change mitigation pledges are fulfilled on time (Meinshausen et al., 2022). Compared to SSP1-1.9, the average triggering probability is increasing by 10 pp to 38%.

Additional impacts from glacier retreat causing water shortage for up to 8.9% of the global population who depend on glacier discharge (Schaner et al., 2012), and LABC collapse, causing a regional cooling over the North Atlantic and potentially affecting the AMOC (Caesar et al., 2018), become more likely than not to occur (Fig. 28). However, especially tipping of TEs within the cryosphere might be less likely than assumed by us under SSP1-1.9 and SSP1-2.6 with peak warming reached within the 21st century (Fig. 14). The threshold temperature of slow-onset TEs like ice sheets can be exceeded temporarily without triggering the TE if the overshoot time is short compared to the characteristic timescale of the TE (Ritchie et al., 2021), which is not accounted for in this study.

A continuation of current politics and actions would lead to a warming of $\sim 2.7$°C in 2100 (Climate Action Tracker, 2022), comparable to the one observed under SSP2-4.5 (Fig.14), which is associated with a drastic increase of average tipping probabilities by 27 pp compared to SSP1-2.6. The impacts from triggered TEs become much more certain, with six TEs becoming extremely likely to be triggered if carbon emissions from carbon TEs are included, and much more numerous with AMAZ, BORF, EASB, and SAHL becoming more likely to be triggered in addition to TEs previously mentioned (Fig. 29). Sea level rise of several meters becomes more likely since EASB makes up for major parts of the 19.2 m SLE stored in marine parts of the EAIS (Fretwell et al., 2013; Stokes et al., 2022). Additional carbon emissions and a decrease in biodiversity from BORF and AMAZ dieback are about as likely as not to occur and shifts in the WAM are becoming likely, affecting local communities in the Sahel region (Nicholson, 2018). Furthermore, the highest long-term temperature increase from carbon TEs becomes possible under SSP2-4.5 (Tab. 2), causing the highest increase of triggering probabilities (3.3 pp on average) out of all SSPs. Tipping cascades due to interactions between TEs not accounted for in this study might become more likely under SSP2-4.5 since tipping of the AMOC, which acts as the main mediator between different TEs (Wunderling et al., 2021), becomes about as likely as not to occur. This should encourage increased efforts of governments worldwide to work towards the timely fulfilment of their climate change mitigation pledges, since the risk of triggering multiple TEs is reduced significantly when moving from SSP2-4.5 to SSP1-2.6.

Under the high emission scenarios SSP3-7.0 and SSP5-8.5, nearly all TEs become likely or even extremely likely to be triggered with average triggering probabilities of 92% and 95% respectively. Hence, impacts from all TEs must be expected. Tipping of the AMOC into a weaker state with manifold impacts on the Earth system (Jackson et al., 2015) is about as likely as not to happen under both scenarios. AWSI is likely to disappear completely, affecting biodiversity and causing increased heat uptake of the Arctic Ocean (Hankel and Tziperman, 2021). Carbon emissions of up to 250 GtC from PFTP become very likely, which

might be partially offset by TUND (Armstrong McKay et al., 2022). Triggering of EAIS is about as likely as not to occur, which has the potential to increase GMSL by up to 34 m (Fretwell et al., 2013).

# 5 Conclusion

We find that the highest long-term temperature increase from carbon TEs among all Tier1 SSPs becomes possible under SSP2-4.5 with 0.16°C (0.03-0.91°C) in 2500. This is due to the fact that maximum carbon emissions from the carbon TEs become possible under SSP2-4.5 since triggering of PFTP and AMAZ is about as likely as not while triggering of PFAT is extremely likely. In this case, anthropogenic carbon emissions are increased substantially by carbon emissions from carbon TEs. Under lower emission scenarios, tipping of AMAZ and PFTP and therefore high carbon emissions from carbon TEs remain unlikely, limiting the maximum temperature increase to 0.05°C (0-0.29°C) in 2300 under SSP1-1.9. Under higher emission scenarios, triggering of PFTP and AMAZ becomes likely (SSP3-7.0) or even extremely likely (SSP5-8.5), causing maximum carbon emissions to be released from the carbon TEs, with $CO_2$ emissions of 331 GtC (246-411 GtC) and $CH_4$ emissions of 37.7 $GtCH_4$ (24.3-54.7 $GtCH_4$) released until 2500 under SSP5-8.5. High $CH_4$ emissions mainly from PFAT within the 21st and 22nd century are causing maximum temperature increases of 0.4°C (0.09-1.11°C) under SSP5-8.5 in 2100. However, the temperature increase from carbon TEs decreases after 2100 under SSP5-8.5 down to 0.18°C (0.08-0.47°C) in 2500 since atmospheric $CH_4$ concentration anomalies are vanishing and because the $CO_2$ emissions from carbon TEs are small compared to the anthropogenic emissions.

Carbon emissions from carbon TEs reduce the feasibility of temperature targets, increasing the probability of exceeding 2°C in 2100 under SSP1-1.9 from 9.86% to $13.5 \pm 0.39$%. Under SSP2-4.5, the probability of exceeding a warming of 4°C in 2100 is increased from 5.6% to $11.7 \pm 0.26$%.

Furthermore, carbon TEs have the potential to cause a local super-linear response of GMST to cumulative anthropogenic $CO_2$ emissions under SSP2-4.5 at around 1400 GtC, which challenges the notion of a linear TCRE. However, such super-linear behaviour has only been found for individual ensemble members and not across the whole ensemble.

Even though clearly observable, the temperature increase from carbon TEs is not strong and abrupt enough to produce any tipping cascades, but rather leads to generally higher probabilities of triggering, making earlier triggering more likely. On average, TEs become more likely to be triggered than not 9.3 years earlier if carbon emissions from carbon TEs are accounted for.

Our results underline the urgent need for further reduction of anthropogenic GHG emissions to avoid crossing of climate tipping points, as triggering of multiple TEs is more likely than previously assumed (compare Kriegler et al., 2009). Under SSP5-8.5, all TEs become more

likely than not, and twelve out of 16 even become extremely likely to be triggered. The risk of triggering multiple TEs is only marginally decreased by moving from SSP5-8.5 to SSP3-7.0, with the average probability of triggering until 2500 being reduced from 95% to 92%. Current politics and actions are leading to a warming of $\sim 2.7$°C in 2100 (Climate Action Tracker, 2022), comparable to what we expect under SSP2-4.5. This pathway is still highly unsafe with respect to crossing climate tipping points, as the average probability of triggering until 2500 is 65%. This number is increased by 3.3 pp if carbon emissions from carbon TEs are included, which is the highest increase of triggering probabilities from carbon TEs out of all SSPs.

It seems to be too late to opt for emission reductions that keep the world safe from triggering any TE, since five TEs become more likely than not to be triggered until 2031 even under SSP1-1.9. Nevertheless, this scenario minimizes the risk of triggering multiple TEs, with an average triggering probability of 28% until 2500. Yet, it might be politically infeasible to achieve SSP1-1.9 (Jewell and Cherp, 2020). SSP1-2.6 is potentially a more realistic scenario, associated with limiting global warming to just below 2°C in 2100, which can be achieved if current climate mitigation pledges are met in full and timely by all parties (Meinshausen et al., 2022). This would limit the risk of triggering multiple TEs to an average probability of triggering until 2500 of 38%, which is increased by 2.3 pp if carbon emissions from carbon TEs are included. Therefore, moving from current policies to more strict climate policies that comply with given pledges would reduce the risk of triggering TEs on average by 28 pp and decrease the additional warming from carbon TEs. Although the debate on climate tipping points is fraught with uncertainty, our work suggests that, despite the potential temperature increase from triggered carbon TEs, it is in the hands of the human society to steer the world towards a sustainable future with limited global warming, which is necessary to significantly reduce the risk of crossing climate tipping points.

# References

Abis, Beniamino and Victor Brovkin (2017). "Environmental conditions for alternative tree-cover states in high latitudes". In: *Biogeosciences* 14.3, pp. 511–527. ISSN: 17264189. DOI: 10.5194/bg-14-511-2017.

Arctic Council (2023). *Arctic Peoples*. URL: https://www.arctic-council.org/explore/topics/arctic-peoples/ (visited on 01/23/2023).

Armstrong McKay, David I., Arie Staal, Jesse F. Abrams, Ricarda Winkelmann, Boris Sakschewski, Sina Loriani, Ingo Fetzer, Sarah E. Cornell, Johan Rockström, and Timothy M. Lenton (2022). "Exceeding 1.5°C global warming could trigger multiple climate tipping points". In: *Science (New York, N.Y.)* 377.6611, eabn7950. ISSN: 10959203. DOI: 10.1126/science.abn7950.

Arnold, Nathan P., Mark Branson, Melissa A. Burt, Dorian S. Abbot, Zhiming Kuang, David A. Randall, and Eli Tziperman (July 2014). "Effects of explicit atmospheric convection at high CO $_2$". en. In: *Proceedings of the National Academy of Sciences* 111.30, pp. 10943–10948. ISSN: 0027-8424, 1091-6490. DOI: 10.1073/pnas.1407175111. URL: https://pnas.org/doi/full/10.1073/pnas.1407175111 (visited on 01/24/2023).

Arora, Vivek K., Anna Katavouta, Richard G. Williams, Chris D. Jones, Victor Brovkin, Pierre Friedlingstein, Jörg Schwinger, Laurent Bopp, Olivier Boucher, Patricia Cadule, Matthew A. Chamberlain, James R. Christian, Christine Delire, A. Rosie A. Fisher, Tomohiro Hajima, Tatiana Ilyina, Emilie Joetzjer, Michio Kawamiya, Charles D. Koven, John P. Krasting, Rachel M. Law, David M. Lawrence, Andrew Lenton, Keith Lindsay, Julia Pongratz, Thomas Raddatz, Roland Séférian, Kaoru Tachiiri, Jerry F. Tjiputra, Andy Wiltshire, Tongwen Wu, and Tilo Ziehn (2020). "Carbon-concentration and carbon-climate feedbacks in CMIP6 models and their comparison to CMIP5 models". In: *Biogeosciences* 17.16, pp. 4173–4222. ISSN: 17264189. DOI: 10.5194/bg-17-4173-2020.

Arthern, Robert J. and C. Rosie Williams (Mar. 2017). "The sensitivity of West Antarctica to the submarine melting feedback". en. In: *Geophysical Research Letters* 44.5, pp. 2352–2359. ISSN: 0094-8276, 1944-8007. DOI: 10.1002/2017GL072514. URL: https://onlinelibrary.wiley.com/doi/abs/10.1002/2017GL072514 (visited on 01/17/2023).

Aschwanden, Andy, Mark A. Fahnestock, Martin Truffer, Douglas J. Brinkerhoff, Regine Hock, Constantine Khroulev, Ruth Mottram, and S. Abbas Khan (June 2019). "Contribution of the Greenland Ice Sheet to sea level over the next millennium". en. In: *Science Advances* 5.6, eaav9396. ISSN: 2375-2548. DOI: 10.1126/sciadv.aav9396. URL: https://www.science.org/doi/10.1126/sciadv.aav9396 (visited on 01/17/2023).

Bakker, Alexander M. R., Tony E. Wong, Kelsey L. Ruckert, and Klaus Keller (June 2017). "Sea-level projections representing the deeply uncertain contribution of the West Antarctic

ice sheet". en. In: *Scientific Reports* 7.1, p. 3880. ISSN: 2045-2322. DOI: 10.1038/s41598-017-04134-5. URL: https://www.nature.com/articles/s41598-017-04134-5 (visited on 01/18/2023).

Belgorodski, Natalia, Matthias Greiner, Kristin Tolksdorf, Katharina Schueller, Matthias Flor, and Lutz Göhring (Mar. 24, 2017). *rriskDistributions*. Version 2.1.2. URL: https://CRAN.R-project.org/package=rriskDistributions.

Biskaborn, Boris K., Sharon L. Smith, Jeannette Noetzli, Heidrun Matthes, Gonçalo Vieira, Dmitry A. Streletskiy, Philippe Schoeneich, Vladimir E. Romanovsky, Antoni G. Lewkowicz, Andrey Abramov, Michel Allard, Julia Boike, William L. Cable, Hanne H. Christiansen, Reynald Delaloye, Bernhard Diekmann, Dmitry Drozdov, Bernd Etzelmüller, Guido Grosse, Mauro Guglielmin, Thomas Ingeman-Nielsen, Ketil Isaksen, Mamoru Ishikawa, Margareta Johansson, Halldor Johannsson, Anseok Joo, Dmitry Kaverin, Alexander Kholodov, Pavel Konstantinov, Tim Kröger, Christophe Lambiel, Jean Pierre Lanckman, Dongliang Luo, Galina Malkova, Ian Meiklejohn, Natalia Moskalenko, Marc Oliva, Marcia Phillips, Miguel Ramos, A. Britta K. Sannel, Dmitrii Sergeev, Cathy Seybold, Pavel Skryabin, Alexander Vasiliev, Qingbai Wu, Kenji Yoshikawa, Mikhail Zheleznyak, and Hugues Lantuit (2019). "Permafrost is warming at a global scale". In: *Nature Communications* 10.1, pp. 1–11. ISSN: 20411723. DOI: 10.1038/s41467-018-08240-4.

Boening, Carmen, Matthew Lebsock, Felix Landerer, and Graeme Stephens (2012). "Snowfall-driven mass change on the East Antarctic ice sheet". en. In: *Geophysical Research Letters* 39.21. _eprint: https://onlinelibrary.wiley.com/doi/pdf/10.1029/2012GL053316. ISSN: 1944-8007. DOI: 10.1029/2012GL053316. URL: https://onlinelibrary.wiley.com/doi/abs/10.1029/2012GL053316 (visited on 01/19/2023).

Boers, Niklas (2021). "Observation-based early-warning signals for a collapse of the Atlantic Meridional Overturning Circulation". In: *Nature Climate Change* 11.8, pp. 680–688. ISSN: 17586798. DOI: 10.1038/s41558-021-01097-4. URL: http://dx.doi.org/10.1038/s41558-021-01097-4.

Boers, Niklas and Martin Rypdal (2021). "Critical slowing down suggests that the western Greenland Ice Sheet is close to a tipping point". In: *Proceedings of the National Academy of Sciences of the United States of America* 118.21, pp. 1–7. ISSN: 10916490. DOI: 10.1073/pnas.2024192118.

Bonan, Gordon B. (June 2008). "Forests and Climate Change: Forcings, Feedbacks, and the Climate Benefits of Forests". en. In: *Science* 320.5882, pp. 1444–1449. ISSN: 0036-8075, 1095-9203. DOI: 10.1126/science.1155121. URL: https://www.science.org/doi/10.1126/science.1155121 (visited on 01/05/2023).

Born, Andreas and Juliette Mignot (July 2012). "Dynamics of decadal variability in the Atlantic subpolar gyre: a stochastically forced oscillator". en. In: *Climate Dynamics* 39.1-

2, pp. 461–474. ISSN: 0930-7575, 1432-0894. DOI: 10.1007/s00382-011-1180-4. URL: http://link.springer.com/10.1007/s00382-011-1180-4 (visited on 03/05/2023).

Boulton, Chris A., Timothy M. Lenton, and Niklas Boers (2022). "Pronounced loss of Amazon rainforest resilience since the early 2000s". In: *Nature Climate Change* 12.3, pp. 271–278. ISSN: 17586798. DOI: 10.1038/s41558-022-01287-8.

Brienen, R. J. W., O. L. Phillips, T. R. Feldpausch, E. Gloor, T. R. Baker, J. Lloyd, G. Lopez-Gonzalez, A. Monteagudo-Mendoza, Y. Malhi, S. L. Lewis, R. Vásquez Martinez, M. Alexiades, E. Álvarez Dávila, P. Alvarez-Loayza, A. Andrade, L. E. O. C. Aragão, A. Araujo-Murakami, E. J. M. M. Arets, L. Arroyo, G. A. Aymard C., O. S. Bánki, C. Baraloto, J. Barroso, D. Bonal, R. G. A. Boot, J. L. C. Camargo, C. V. Castilho, V. Chama, K. J. Chao, J. Chave, J. A. Comiskey, F. Cornejo Valverde, L. da Costa, E. A. de Oliveira, A. Di Fiore, T. L. Erwin, S. Fauset, M. Forsthofer, D. R. Galbraith, E. S. Grahame, N. Groot, B. Hérault, N. Higuchi, E. N. Honorio Coronado, H. Keeling, T. J. Killeen, W. F. Laurance, S. Laurance, J. Licona, W. E. Magnussen, B. S. Marimon, B. H. Marimon-Junior, C. Mendoza, D. A. Neill, E. M. Nogueira, P. Núñez, N. C. Pallqui Camacho, A. Parada, G. Pardo-Molina, J. Peacock, M. Peña-Claros, G. C. Pickavance, N. C. A. Pitman, L. Poorter, A. Prieto, C. A. Quesada, F. Ramírez, H. Ramírez-Angulo, Z. Restrepo, A. Roopsind, A. Rudas, R. P. Salomão, M. Schwarz, N. Silva, J. E. Silva-Espejo, M. Silveira, J. Stropp, J. Talbot, H. ter Steege, J. Teran-Aguilar, J. Terborgh, R. Thomas-Caesar, M. Toledo, M. Torello-Raventos, R. K. Umetsu, G. M. F. van der Heijden, P. van der Hout, I. C. Guimarães Vieira, S. A. Vieira, E. Vilanova, V. A. Vos, and R. J. Zagt (Mar. 2015). "Long-term decline of the Amazon carbon sink". en. In: *Nature* 519.7543, pp. 344–348. ISSN: 0028-0836, 1476-4687. DOI: 10.1038/nature14283. URL: http://www.nature.com/articles/nature14283 (visited on 01/10/2023).

Brovkin, Victor, Edward Brook, John W. Williams, Sebastian Bathiany, Timothy M. Lenton, Michael Barton, Robert M. DeConto, Jonathan F. Donges, Andrey Ganopolski, Jerry McManus, Summer Praetorius, Anne de Vernal, Ayako Abe-Ouchi, Hai Cheng, Martin Claussen, Michel Crucifix, Gilberto Gallopín, Virginia Iglesias, Darrell S. Kaufman, Thomas Kleinen, Fabrice Lambert, Sander van der Leeuw, Hannah Liddy, Marie France Loutre, David McGee, Kira Rehfeld, Rachael Rhodes, Alistair W.R. Seddon, Martin H. Trauth, Lilian Vanderveken, and Zicheng Yu (2021). "Past abrupt changes, tipping points and cascading impacts in the Earth system". In: *Nature Geoscience* 14.8. Publisher: Springer US ISBN: 4156102100790, pp. 550–558. ISSN: 17520908. DOI: 10.1038/s41561-021-00790-5. URL: http://dx.doi.org/10.1038/s41561-021-00790-5.

Bryden, H.L. and S. Imawaki (2001). "Ocean heat transport". In: *Ocean Circulation and Climate: Observing and Modelling the Global Ocean*. Ed. by G. Siedler, J. Church, and J. Gould. 77. Academic Press, pp. 455–474. URL: https://eprints.soton.ac.uk/54882/.

Buckley, Martha W. and John Marshall (Mar. 2016). "Observations, inferences, and mechanisms of the Atlantic Meridional Overturning Circulation: A review". en. In: *Reviews of Geophysics* 54.1, pp. 5–63. ISSN: 8755-1209, 1944-9208. DOI: 10.1002/2015RG000493. URL: https://onlinelibrary.wiley.com/doi/10.1002/2015RG000493 (visited on 03/05/2023).

Burke, Eleanor J., Altug Ekici, Ye Huang, Sarah E. Chadburn, Chris Huntingford, Philippe Ciais, Pierre Friedlingstein, Shushi Peng, and Gerhard Krinner (2017). "Quantifying uncertainties of permafrost carbon-climate feedbacks". In: *Biogeosciences* 14.12, pp. 3051–3066. ISSN: 17264189. DOI: 10.5194/bg-14-3051-2017.

Burke, Eleanor J., Yu Zhang, and Gerhard Krinner (2020). "Evaluating permafrost physics in the Coupled Model Intercomparison Project 6 (CMIP6) models and their sensitivity to climate change". In: *Cryosphere* 14.9, pp. 3155–3174. ISSN: 19940424. DOI: 10.5194/tc-14-3155-2020.

Burton, Philip J., Bergeron, Yves, Bogdanski, Bryan E.C., Juday, Glenn Patrick, Kuuluvainen, Timo, McAfee, Brenda, Ogden, Aynslie, and Teplyakov, Victor K. (2010). "Sustainability of Boreal Forests and Forestry in a Changing Environment". In: *Forests and Society – Responding to Global Drivers of Change*. Ed. by Gerardo, Mery, Katila, Pia, Galloway, Glen, I. Alfaro, René, Kanninen, Markku, Lobovikov, Maxim, and Varjo, Jari. 25. Vienna: IUFRO World Series, pp. 249–282. URL: https://www.iufro.org/science/wfse/forests-society-global-drivers/.

Caesar, L., S. Rahmstorf, A. Robinson, G. Feulner, and V. Saba (Apr. 2018). "Observed fingerprint of a weakening Atlantic Ocean overturning circulation". en. In: *Nature* 556.7700, pp. 191–196. ISSN: 0028-0836, 1476-4687. DOI: 10.1038/s41586-018-0006-5. URL: http://www.nature.com/articles/s41586-018-0006-5 (visited on 02/06/2023).

Cai, Yongyang, Kenneth L. Judd, Timothy M. Lenton, Thomas S. Lontzek, and Daiju Narita (Apr. 2015). "Environmental tipping points significantly affect the cost-benefit assessment of climate policies". en. In: *Proceedings of the National Academy of Sciences* 112.15, pp. 4606–4611. ISSN: 0027-8424, 1091-6490. DOI: 10.1073/pnas.1503890112. URL: https://pnas.org/doi/full/10.1073/pnas.1503890112 (visited on 03/03/2023).

Cai, Yongyang, Timothy M Lenton, and Thomas S Lontzek (2016). "Risk of multiple interacting tipping points should encourage rapid CO2 emission reduction". In: *Nature Climate Change* 6.5, pp. 520–525. ISSN: 17586798. DOI: 10.1038/nclimate2964.

Canadell, J.G., P.M.S. Monteiro, M.H. Costa, L. Cotrim da Cunha, P.M. Cox, A.V. Eliseev, S. Henson, M. Ishii, S. Jaccard, C. Koven, A. Lohila, P.K. Patra, S. Piao, J. Rogelj, S. Syampungani, S. Zaehle, and K. Zickfeld (2021). "Global Carbon and other Biogeochemical Cycles and Feedbacks". In: *Climate Change 2021: The Physical Science Basis. Contribution of Working Group I to the Sixth Assessment Report of the Intergovernmental Panel on*

*Climate Change*. Ed. by V. Masson-Delmotte, P. Zhai, A. Pirani, S.L. Connors, C. Péan, S. Berger, N. Caud, Y. Chen, L. Goldfarb, M.I. Gomis, M. Huang, K. Leitzell, E. Lonnoy, J.B.R. Matthews, T.K. Maycock, T. Waterfield, O. Yelekçi, R. Yu, and B. Zhou. Cambridge, United Kingdom and New York, NY, USA: Cambridge University Press, pp. 673–816. DOI: 10.1017/9781009157896.007.

Chapin 3., Stuart F., Pamela A. Matson, and Harold A. Mooney (2002). *Principals of Terrestrial Ecosystem Ecology*. New York: Springer-Verlag. ISBN: 0-387-95439-2.

Chen, D., M. Rojas, B.H. Samset, K. Cobb, A. Diongue Niang, P. Edwards, S. Emori, S.H. Faria, E. Hawkins, P. Hope, P. Huybrechts, M. Meinshausen, S.K. Mustafa, G.-K. Plattner, and A.-M. Tréguier (2021). "Framing, Context, and Methods". In: *Climate Change 2021: The Physical Science Basis. Contribution of Working Group I to the Sixth Assessment Report of the Intergovernmental Panel on Climate Change*. Ed. by V. Masson-Delmotte, P. Zhai, A. Pirani, S.L. Connors, C. Péan, S. Berger, N. Caud, Y. Chen, L. Goldfarb, M.I. Gomis, M. Huang, K. Leitzell, E. Lonnoy, J.B.R. Matthews, T.K. Maycock, T. Waterfield, O. Yelekçi, R. Yu, and B. Zhou. Cambridge, United Kingdom and New York, NY, USA: Cambridge University Press, pp. 147–286. DOI: 10.1017/9781009157896.003.

Christ, Andrew J., Paul R. Bierman, Joerg M. Schaefer, Dorthe Dahl-Jensen, Jørgen P. Steffensen, Lee B. Corbett, Dorothy M. Peteet, Elizabeth K. Thomas, Eric J. Steig, Tammy M. Rittenour, Jean-Louis Tison, Pierre-Henri Blard, Nicolas Perdrial, David P. Dethier, Andrea Lini, Alan J. Hidy, Marc W. Caffee, and John Southon (Mar. 2021). "A multimillion-year-old record of Greenland vegetation and glacial history preserved in sediment beneath 1.4 km of ice at Camp Century". en. In: *Proceedings of the National Academy of Sciences* 118.13, e2021442118. ISSN: 0027-8424, 1091-6490. DOI: 10.1073/pnas.2021442118. URL: https://pnas.org/doi/full/10.1073/pnas.2021442118 (visited on 01/09/2023).

Clarke, Joseph, Chris Huntingford, Paul Ritchie, and Peter Cox (2021). "The compost bomb instability in the continuum limit". In: *European Physical Journal: Special Topics* 230.16-17, pp. 3335–3341. ISSN: 19516401. DOI: 10.1140/epjs/s11734-021-00013-3. URL: https://doi.org/10.1140/epjs/s11734-021-00013-3.

Climate Action Tracker (Nov. 2022). *The CAT Thermometer*. en. URL: https://climateactiontracker.org/global/cat-thermometer/ (visited on 02/07/2023).

Cochrane, Mark A., Ane Alencar, Mark D. Schulze, Carlos M. Souza, Daniel C. Nepstad, Paul Lefebvre, and Eric A. Davidson (June 1999). "Positive Feedbacks in the Fire Dynamic of Closed Canopy Tropical Forests". en. In: *Science* 284.5421, pp. 1832–1835. ISSN: 0036-8075, 1095-9203. DOI: 10.1126/science.284.5421.1832. URL: https://www.science.org/doi/10.1126/science.284.5421.1832 (visited on 01/10/2023).

Comyn-Platt, Edward, Garry Hayman, Chris Huntingford, Sarah E Chadburn, Eleanor J Burke, Anna B Harper, William J Collins, Christopher P Webber, Tom Powell, Peter M

Cox, Nicola Gedney, and Stephen Sitch (2018). "Carbon budgets for 1.5 and 2 °C targets lowered by Natural Wetland and Permafrost Feedbacks". In: *Nature Geoscience* 11.August. ISSN: 1752-0908. URL: http://dx.doi.org/10.1038/s41561-018-0174-9.

Cox, Peter M, Richard A Betts, Chris D Jones, Steven A Spall, and Ian J. Totterdell (2000). "Acceleration of global warming due to carbon-cycle feedbacks inacoupled climatemodel". In: *Nature* 408.November, pp. 184–187.

Cox, Peter M., R. A. Betts, M. Collins, P. P. Harris, C. Huntingford, and C. D. Jones (2004). "Amazonian forest dieback under climate-carbon cycle projections for the 21st century". In: *Theoretical and Applied Climatology* 78.1-3, pp. 137–156. ISSN: 0177798X. DOI: 10.1007/s00704-004-0049-4.

Cox, Peter M., David Pearson, Ben B. Booth, Pierre Friedlingstein, Chris Huntingford, Chris D. Jones, and Catherine M. Luke (2013). "Sensitivity of tropical carbon to climate change constrained by carbon dioxide variability". In: *Nature* 494.7437, pp. 341–344. ISSN: 00280836. DOI: 10.1038/nature11882.

Crowther, T. W., H. B. Glick, K. R. Covey, C. Bettigole, D. S. Maynard, S. M. Thomas, J. R. Smith, G. Hintler, M. C. Duguid, G. Amatulli, M.-N. Tuanmu, W. Jetz, C. Salas, C. Stam, D. Piotto, R. Tavani, S. Green, G. Bruce, S. J. Williams, S. K. Wiser, M. O. Huber, G. M. Hengeveld, G.-J. Nabuurs, E. Tikhonova, P. Borchardt, C.-F. Li, L. W. Powrie, M. Fischer, A. Hemp, J. Homeier, P. Cho, A. C. Vibrans, P. M. Umunay, S. L. Piao, C. W. Rowe, M. S. Ashton, P. R. Crane, and M. A. Bradford (Sept. 2015). "Mapping tree density at a global scale". en. In: *Nature* 525.7568, pp. 201–205. ISSN: 0028-0836, 1476-4687. DOI: 10.1038/nature14967. URL: http://www.nature.com/articles/nature14967 (visited on 01/05/2023).

DeConto, Robert M., David Pollard, Richard B. Alley, Isabella Velicogna, Edward Gasson, Natalya Gomez, Shaina Sadai, Alan Condron, Daniel M. Gilford, Erica L. Ashe, Robert E. Kopp, Dawei Li, and Andrea Dutton (May 2021). "The Paris Climate Agreement and future sea-level rise from Antarctica". en. In: *Nature* 593.7857, pp. 83–89. ISSN: 0028-0836, 1476-4687. DOI: 10.1038/s41586-021-03427-0. URL: http://www.nature.com/articles/s41586-021-03427-0 (visited on 01/20/2023).

Dietz, Simon, James Rising, Thomas Stoerk, and Gernot Wagner (Aug. 2021). "Economic impacts of tipping points in the climate system". en. In: *Proceedings of the National Academy of Sciences* 118.34, e2103081118. ISSN: 0027-8424, 1091-6490. DOI: 10.1073/pnas.2103081118. URL: https://pnas.org/doi/full/10.1073/pnas.2103081118 (visited on 03/03/2023).

Dirzo, Rodolfo and Peter H. Raven (Nov. 2003). "Global State of Biodiversity and Loss". en. In: *Annual Review of Environment and Resources* 28.1, pp. 137–167. ISSN: 1543-5938, 1545-2050. DOI: 10.1146/annurev.energy.28.050302.105532. URL: https://www

.annualreviews.org/doi/10.1146/annurev.energy.28.050302.105532 (visited on 01/10/2023).

Dobinski, Wojciech (2011). "Permafrost". In: *Earth-Science Reviews* 108.3-4, pp. 158–169. ISSN: 00128252. DOI: 10.1016/j.earscirev.2011.06.007.

Dosio, Alessandro, Martin W. Jury, Mansour Almazroui, Moetasim Ashfaq, Ismaila Diallo, Francois A. Engelbrecht, Nana A. B. Klutse, Christopher Lennard, Izidine Pinto, Mouhamadou B. Sylla, and Alain T. Tamoffo (Dec. 2021). "Projected future daily characteristics of African precipitation based on global (CMIP5, CMIP6) and regional (CORDEX, CORDEX-CORE) climate models". en. In: *Climate Dynamics* 57.11-12, pp. 3135–3158. ISSN: 0930-7575, 1432-0894. DOI: 10.1007/s00382-021-05859-w. URL: https://link.springer.com/10.1007/s00382-021-05859-w (visited on 01/07/2023).

Douglas, A.E. (Apr. 2003). "Coral bleaching—how and why?" en. In: *Marine Pollution Bulletin* 46.4, pp. 385–392. ISSN: 0025326X. DOI: 10.1016/S0025-326X(03)00037-7. URL: https://linkinghub.elsevier.com/retrieve/pii/S0025326X03000377 (visited on 01/09/2023).

Drijfhout, Sybren, Sebastian Bathiany, Claudie Beaulieu, Victor Brovkin, Martin Claussen, Chris Huntingford, Marten Scheffer, Giovanni Sgubin, and Didier Swingedouw (2015). "Catalogue of abrupt shifts in Intergovernmental Panel on Climate Change climate models". In: *Proceedings of the National Academy of Sciences of the United States of America* 112.43, E5777–E5786. ISSN: 10916490. DOI: 10.1073/pnas.1511451112.

Eddy, Tyler D., Vicky W.Y. Lam, Gabriel Reygondeau, Andrés M. Cisneros-Montemayor, Krista Greer, Maria Lourdes D. Palomares, John F. Bruno, Yoshitaka Ota, and William W.L. Cheung (Sept. 2021). "Global decline in capacity of coral reefs to provide ecosystem services". en. In: *One Earth* 4.9, pp. 1278–1285. ISSN: 25903322. DOI: 10.1016/j.oneear.2021.08.016. URL: https://linkinghub.elsevier.com/retrieve/pii/S2590332221004747 (visited on 01/09/2023).

Edwards, Tamsin L., Mark A. Brandon, Gael Durand, Neil R. Edwards, Nicholas R. Golledge, Philip B. Holden, Isabel J. Nias, Antony J. Payne, Catherine Ritz, and Andreas Wernecke (Feb. 2019). "Revisiting Antarctic ice loss due to marine ice-cliff instability". en. In: *Nature* 566.7742, pp. 58–64. ISSN: 0028-0836, 1476-4687. DOI: 10.1038/s41586-019-0901-4. URL: http://www.nature.com/articles/s41586-019-0901-4 (visited on 01/20/2023).

Elberling, Bo, Anders Michelsen, Christina Schädel, Edward A.G. Schuur, Hanne H. Christiansen, Louise Berg, Mikkel P. Tamstorf, and Charlotte Sigsgaard (2013). "Long-term CO2 production following permafrost thaw". In: *Nature Climate Change* 3.10, pp. 890–894. ISSN: 1758678X. DOI: 10.1038/nclimate1955.

Elias, Scott (2021). "Chapter 10 - Greenland Ice Sheet". In: *Threats to the Arctic*. Ed. by Scott Elias. Elsevier, pp. 265–321. ISBN: 978-0-12-821555-5. DOI: https://doi.org/10.10

16/B978-0-12-821555-5.00009-7. URL: https://www.sciencedirect.com/science/article/pii/B9780128215555000097.

Erfanian, Amir, Guiling Wang, Miao Yu, and Richard Anyah (Sept. 2016). "Multimodel ensemble simulations of present and future climates over West Africa: Impacts of vegetation dynamics: ENSEMBLE CLIMATE SIMULATIONS OVER WA". en. In: *Journal of Advances in Modeling Earth Systems* 8.3, pp. 1411–1431. ISSN: 19422466. DOI: 10.1002/2016MS000660. URL: http://doi.wiley.com/10.1002/2016MS000660 (visited on 01/07/2023).

Etminan, M., G. Myhre, E. J. Highwood, and K. P. Shine (2016). "Radiative forcing of carbon dioxide, methane, and nitrous oxide: A significant revision of the methane radiative forcing". In: *Geophysical Research Letters* 43.24, pp. 12, 614–12, 623. ISSN: 19448007. DOI: 10.1002/2016GL071930.

Euskirchen, E. S., A. D. McGuire, F. S. Chapin, S. Yi, and C. C. Thompson (June 2009). "Changes in vegetation in northern Alaska under scenarios of climate change, 2003–2100: implications for climate feedbacks". en. In: *Ecological Applications* 19.4, pp. 1022–1043. ISSN: 1051-0761. DOI: 10.1890/08-0806.1. URL: http://doi.wiley.com/10.1890/08-0806.1 (visited on 12/23/2022).

Eyring, Veronika, Sandrine Bony, Gerald A. Meehl, Catherine A. Senior, Bjorn Stevens, Ronald J. Stouffer, and Karl E. Taylor (2016). "Overview of the Coupled Model Intercomparison Project Phase 6 (CMIP6) experimental design and organization". In: *Geoscientific Model Development* 9.5, pp. 1937–1958. ISSN: 19919603. DOI: 10.5194/gmd-9-1937-2016.

Forster, P., T. Storelvmo, K. Armour, W. Collins, J.-L. Dufresne, D. Frame, D.J. Lunt, T. Mauritsen, M.D. Palmer, M. Watanabe, M. Wild, and H. Zhang (2021). "The Earth's Energy Budget, Climate Feedbacks, and Climate Sensitivity". In: *Climate Change 2021: The Physical Science Basis. Contribution of Working Group I to the Sixth Assessment Report of the Intergovernmental Panel on Climate Change*. Ed. by V. Masson-Delmotte, P. Zhai, A. Pirani, S.L. Connors, C. Péan, S. Berger, N. Caud, Y. Chen, L. Goldfarb, M.I. Gomis, M. Huang, K. Leitzell, E. Lonnoy, J.B.R. Matthews, T.K. Maycock, T. Waterfield, O. Yelekçi, R. Yu, and B. Zhou. Cambridge, United Kingdom and New York, NY, USA: Cambridge University Press, pp. 923–1054. DOI: 10.1017/9781009157896.009.

Fox-Kemper, B., H.T. Hewitt, C. Xiao, G. Aðalgeirsdóttir, S.S. Drijfhout, T.L. Edwards, N.R. Golledge, M. Hemer, R.E. Kopp, G. Krinner, A. Mix, D. Notz, S. Nowicki, I.S. Nurhati, L. Ruiz, J.-B. Sallée, A.B.A. Slangen, and Y. Yu (2021). "Ocean, Cryosphere and Sea Level Change". In: *Climate Change 2021: The Physical Science Basis. Contribution of Working Group I to the Sixth Assessment Report of the Intergovernmental Panel on Climate Change*. Ed. by V. Masson-Delmotte, P. Zhai, A. Pirani, S.L. Connors, C. Péan, S. Berger, N. Caud, Y. Chen, L. Goldfarb, M.I. Gomis, M. Huang, K. Leitzell, E. Lonnoy, J.B.R.

Matthews, T.K. Maycock, T. Waterfield, O. Yelekçi, R. Yu, and B. Zhou. Cambridge, United Kingdom and New York, NY, USA: Cambridge University Press, pp. 1211–1362. DOI: 10.1017/9781009157896.011.

Fretwell, P., H. D. Pritchard, D. G. Vaughan, J. L. Bamber, N. E. Barrand, R. Bell, C. Bianchi, R. G. Bingham, D. D. Blankenship, G. Casassa, G. Catania, D. Callens, H. Conway, A. J. Cook, H. F. J. Corr, D. Damaske, V. Damm, F. Ferraccioli, R. Forsberg, S. Fujita, Y. Gim, P. Gogineni, J. A. Griggs, R. C. A. Hindmarsh, P. Holmlund, J. W. Holt, R. W. Jacobel, A. Jenkins, W. Jokat, T. Jordan, E. C. King, J. Kohler, W. Krabill, M. Riger-Kusk, K. A. Langley, G. Leitchenkov, C. Leuschen, B. P. Luyendyk, K. Matsuoka, J. Mouginot, F. O. Nitsche, Y. Nogi, O. A. Nost, S. V. Popov, E. Rignot, D. M. Rippin, A. Rivera, J. Roberts, N. Ross, M. J. Siegert, A. M. Smith, D. Steinhage, M. Studinger, B. Sun, B. K. Tinto, B. C. Welch, D. Wilson, D. A. Young, C. Xiangbin, and A. Zirizzotti (Feb. 2013). "Bedmap2: improved ice bed, surface and thickness datasets for Antarctica". en. In: *The Cryosphere* 7.1, pp. 375–393. ISSN: 1994-0424. DOI: 10.5194/tc-7-375-2013. URL: https://tc.copernicus.org/articles/7/375/2013/ (visited on 01/18/2023).

Frieler, K., M. Meinshausen, A. Golly, M. Mengel, K. Lebek, S. D. Donner, and O. Hoegh-Guldberg (Feb. 2013). "Limiting global warming to 2 °C is unlikely to save most coral reefs". en. In: *Nature Climate Change* 3.2, pp. 165–170. ISSN: 1758-678X, 1758-6798. DOI: 10.1038/nclimate1674. URL: http://www.nature.com/articles/nclimate1674 (visited on 01/09/2023).

Gaetani, Marco, Gabriele Messori, Qiong Zhang, Cyrille Flamant, and Francesco S. R. Pausata (Oct. 2017). "Understanding the Mechanisms behind the Northward Extension of the West African Monsoon during the Mid-Holocene". en. In: *Journal of Climate* 30.19, pp. 7621–7642. ISSN: 0894-8755, 1520-0442. DOI: 10.1175/JCLI-D-16-0299.1. URL: http://journals.ametsoc.org/doi/10.1175/JCLI-D-16-0299.1 (visited on 01/08/2023).

Gao, Fuchang and Lixing Han (2012). "Implementing the Nelder-Mead simplex algorithm with adaptive parameters". In: *Computational Optimization and Applications* 51.1, pp. 259–277. DOI: 10.1007/s10589-010-9329-3.

Garbe, Julius, Torsten Albrecht, Anders Levermann, Jonathan F. Donges, and Ricarda Winkelmann (Sept. 2020). "The hysteresis of the Antarctic Ice Sheet". en. In: *Nature* 585.7826, pp. 538–544. ISSN: 0028-0836, 1476-4687. DOI: 10.1038/s41586-020-2727-5. URL: https://www.nature.com/articles/s41586-020-2727-5 (visited on 01/17/2023).

Gasser, T., M. Kechiar, P. Ciais, E. J. Burke, T. Kleinen, D. Zhu, Y. Huang, A. Ekici, and M. Obersteiner (2018). "Path-dependent reductions in CO2 emission budgets caused by permafrost carbon release". In: *Nature Geoscience* 11.11, pp. 830–835. ISSN: 17520908. DOI: 10.1038/s41561-018-0227-0. URL: http://dx.doi.org/10.1038/s41561-018-0227-0 .

Gasson, Edward, Robert M. DeConto, David Pollard, and Richard H. Levy (Mar. 2016). "Dynamic Antarctic ice sheet during the early to mid-Miocene". en. In: *Proceedings of the National Academy of Sciences* 113.13, pp. 3459–3464. ISSN: 0027-8424, 1091-6490. DOI: 10.1073/pnas.1516130113. URL: https://pnas.org/doi/full/10.1073/pnas.1516130113 (visited on 01/19/2023).

Gatti, Luciana V., Luana S. Basso, John B. Miller, Manuel Gloor, Lucas Gatti Domingues, Henrique L.G. Cassol, Graciela Tejada, Luiz E.O.C. Aragão, Carlos Nobre, Wouter Peters, Luciano Marani, Egidio Arai, Alber H. Sanches, Sergio M. Corrêa, Liana Anderson, Celso Von Randow, Caio S.C. Correia, Stephane P. Crispim, and Raiane A.L. Neves (2021). "Amazonia as a carbon source linked to deforestation and climate change". In: *Nature* 595.7867, pp. 388–393. ISSN: 14764687. DOI: 10.1038/s41586-021-03629-6. URL: http://dx.doi.org/10.1038/s41586-021-03629-6.

Gauthier, S., P. Bernier, T. Kuuluvainen, A. Z. Shvidenko, and D. G. Schepaschenko (Aug. 2015). "Boreal forest health and global change". en. In: *Science* 349.6250, pp. 819–822. ISSN: 0036-8075, 1095-9203. DOI: 10.1126/science.aaa9092. URL: https://www.science.org/doi/10.1126/science.aaa9092 (visited on 01/05/2023).

Gentry, Alwyn H. (Jan. 1988). "Tree species richness of upper Amazonian forests". en. In: *Proceedings of the National Academy of Sciences* 85.1, pp. 156–159. ISSN: 0027-8424, 1091-6490. DOI: 10.1073/pnas.85.1.156. URL: https://pnas.org/doi/full/10.1073/pnas.85.1.156 (visited on 01/10/2023).

Gidden, Matthew J., Keywan Riahi, Steven J. Smith, Shinichiro Fujimori, Gunnar Luderer, Elmar Kriegler, Detlef P. Van Vuuren, Maarten Van Den Berg, Leyang Feng, David Klein, Katherine Calvin, Jonathan C. Doelman, Stefan Frank, Oliver Fricko, Mathijs Harmsen, Tomoko Hasegawa, Petr Havlik, Jérôme Hilaire, Rachel Hoesly, Jill Horing, Alexander Popp, Elke Stehfest, and Kiyoshi Takahashi (2019). "Global emissions pathways under different socioeconomic scenarios for use in CMIP6: A dataset of harmonized emissions trajectories through the end of the century". In: *Geoscientific Model Development* 12.4, pp. 1443–1475. ISSN: 19919603. DOI: 10.5194/gmd-12-1443-2019.

Golledge, N. R., D. E. Kowalewski, T. R. Naish, R. H. Levy, C. J. Fogwill, and E. G. W. Gasson (Oct. 2015). "The multi-millennial Antarctic commitment to future sea-level rise". en. In: *Nature* 526.7573, pp. 421–425. ISSN: 0028-0836, 1476-4687. DOI: 10.1038/nature15706. URL: http://www.nature.com/articles/nature15706 (visited on 01/22/2023).

Grosse, Guido, Jennifer Harden, Merritt Turetsky, A. David McGuire, Philip Camill, Charles Tarnocai, Steve Frolking, Edward A.G. Schuur, Torre Jorgenson, Sergei Marchenko, Vladimir Romanovsky, Kimberly P. Wickland, Nancy French, Mark Waldrop, Laura Bourgeau-Chavez, and Robert G. Striegl (2011). "Vulnerability of high-latitude soil or-

ganic carbon in North America to disturbance". In: *Journal of Geophysical Research: Biogeosciences* 116.3, pp. 1–23. ISSN: 01480227. DOI: 10.1029/2010JG001507.

Guetschow, Johannes, M. Louise Jeffery, Robert Gieseke, Ronja Gebel, David Stevens, Mario Krapp, and Marcia Rocha (2016). "The PRIMAP-hist national historical emissions time series". In: *Earth System Science Data* 8.2, pp. 571–603. ISSN: 18663516. DOI: 10.5194/essd-8-571-2016.

Gulev, S.K., P.W. Thorne, J. Ahn, F.J. Dentener, C.M. Domingues, S. Gerland, D. Gong, D.S. Kaufman, H.C. Nnamchi, J. Quaas, J.A. Rivera, S. Sathyendranath, S.L. Smith, B. Trewin, K. von Schuckmann, and R.S. Vose (2021). "Changing State of the Climate System". In: *Climate Change 2021: The Physical Science Basis. Contribution of Working Group I to the Sixth Assessment Report of the Intergovernmental Panel on Climate Change*. Ed. by V. Masson-Delmotte, P. Zhai, A. Pirani, S.L. Connors, C. Péan, S. Berger, N. Caud, Y. Chen, L. Goldfarb, M.I. Gomis, M. Huang, K. Leitzell, E. Lonnoy, J.B.R. Matthews, T.K. Maycock, T. Waterfield, O. Yelekçi, R. Yu, and B. Zhou. Cambridge, United Kingdom and New York, NY, USA: Cambridge University Press, pp. 287–422. DOI: 10.1017/9781009157896.004.

Hankel, Camille and Eli Tziperman (June 2021). "The Role of Atmospheric Feedbacks in Abrupt Winter Arctic Sea Ice Loss in Future Warming Scenarios". en. In: *Journal of Climate* 34.11, pp. 4435–4447. ISSN: 0894-8755, 1520-0442. DOI: 10.1175/JCLI-D-20-0558.1. URL: https://journals.ametsoc.org/view/journals/clim/34/11/JCLI-D-20-0558.1.xml (visited on 01/23/2023).

Haustein, K., M. R. Allen, P. M. Forster, F. E. L. Otto, D. M. Mitchell, H. D. Matthews, and D. J. Frame (Nov. 2017). "A real-time Global Warming Index". en. In: *Scientific Reports* 7.1, p. 15417. ISSN: 2045-2322. DOI: 10.1038/s41598-017-14828-5. URL: https://www.nature.com/articles/s41598-017-14828-5 (visited on 01/30/2023).

Hawkins, E., R. S. Smith, L. C. Allison, J. M. Gregory, T. J. Woollings, H. Pohlmann, and B. de Cuevas (May 2011). "Bistability of the Atlantic overturning circulation in a global climate model and links to ocean freshwater transport: BISTABILITY OF THE ATLANTIC MOC". en. In: *Geophysical Research Letters* 38.10, n/a–n/a. ISSN: 00948276. DOI: 10.1029/2011GL047208. URL: http://doi.wiley.com/10.1029/2011GL047208 (visited on 02/06/2023).

Hawkins, Ed and Rowan Sutton (Aug. 2009). "The Potential to Narrow Uncertainty in Regional Climate Predictions". en. In: *Bulletin of the American Meteorological Society* 90.8, pp. 1095–1108. ISSN: 0003-0007, 1520-0477. DOI: 10.1175/2009BAMS2607.1. URL: https://journals.ametsoc.org/doi/10.1175/2009BAMS2607.1 (visited on 03/01/2023).

Helton, J. C. and F. J. Davis (2003). "Latin hypercube sampling and the propagation of uncertainty in analyses of complex systems". In: *Reliability Engineering and System Safety* 81.1, pp. 23–69. ISSN: 09518320. DOI: 10.1016/S0951-8320(03)00058-9.

Hezel, P. J., T. Fichefet, and F. Massonnet (July 2014). "Modeled Arctic sea ice evolution through 2300 in CMIP5 extended RCPs". en. In: *The Cryosphere* 8.4, pp. 1195–1204. ISSN: 1994-0424. DOI: 10.5194/tc-8-1195-2014. URL: https://tc.copernicus.org/articles/8/1195/2014/ (visited on 01/23/2023).

Hoesly, R. M., S. J. Smith, L. Feng, Z. Klimont, G. Janssens-Maenhout, T. Pitkanen, J. J. Seibert, L. Vu, R. J. Andres, R. M. Bolt, T. C. Bond, L. Dawidowski, N. Kholod, J.-I. Kurokawa, M. Li, L. Liu, Z. Lu, M. C. P. Moura, P. R. O'Rourke, and Q. Zhang (2018). "Historical (1750–2014) anthropogenic emissions of reactive gases and aerosols from the Community Emissions Data System (CEDS)". In: *Geoscientific Model Development* 11.1, pp. 369–408. DOI: 10.5194/gmd-11-369-2018. URL: https://gmd.copernicus.org/articles/11/369/2018/.

Hugelius, G., J. Strauss, S. Zubrzycki, J. W. Harden, E. A.G. Schuur, C. L. Ping, L. Schirrmeister, G. Grosse, G. J. Michaelson, C. D. Koven, J. A. O'Donnell, B. Elberling, U. Mishra, P. Camill, Z. Yu, J. Palmtag, and P. Kuhry (2014). "Estimated stocks of circumpolar permafrost carbon with quantified uncertainty ranges and identified data gaps". In: *Biogeosciences* 11.23, pp. 6573–6593. ISSN: 17264189. DOI: 10.5194/bg-11-6573-2014.

Hugelius, Gustaf, Julie Loisel, Sarah Chadburn, Robert B. Jackson, Miriam Jones, Glen MacDonald, Maija Marushchak, David Olefeldt, Maara Packalen, Matthias B. Siewert, Claire Treat, Merritt Turetsky, Carolina Voigt, and Zicheng Yu (2020). "Large stocks of peatland carbon and nitrogen are vulnerable to permafrost thaw". In: *Proceedings of the National Academy of Sciences of the United States of America* 117.34, pp. 20438–20446. ISSN: 10916490. DOI: 10.1073/pnas.1916387117.

Hughes, Terry P., Michele L. Barnes, David R. Bellwood, Joshua E. Cinner, Graeme S. Cumming, Jeremy B. C. Jackson, Joanie Kleypas, Ingrid A. van de Leemput, Janice M. Lough, Tiffany H. Morrison, Stephen R. Palumbi, Egbert H. van Nes, and Marten Scheffer (June 2017). "Coral reefs in the Anthropocene". en. In: *Nature* 546.7656, pp. 82–90. ISSN: 0028-0836, 1476-4687. DOI: 10.1038/nature22901. URL: http://www.nature.com/articles/nature22901 (visited on 01/09/2023).

Hugonnet, Romain, Robert McNabb, Etienne Berthier, Brian Menounos, Christopher Nuth, Luc Girod, Daniel Farinotti, Matthias Huss, Ines Dussaillant, Fanny Brun, and Andreas Kääb (Apr. 2021). "Accelerated global glacier mass loss in the early twenty-first century". en. In: *Nature* 592.7856, pp. 726–731. ISSN: 0028-0836, 1476-4687. DOI: 10.1038/s41586-021-03436-z. URL: http://www.nature.com/articles/s41586-021-03436-z (visited on 01/30/2023).

Huss, Matthias and Regine Hock (Feb. 2018). "Global-scale hydrological response to future glacier mass loss". en. In: *Nature Climate Change* 8.2, pp. 135–140. ISSN: 1758-678X,

1758-6798. DOI: 10.1038/s41558-017-0049-x. URL: http://www.nature.com/articles/s41558-017-0049-x (visited on 01/30/2023).

IPCC (2021). "Summary for Policymakers". In: *Climate Change 2021: The Physical Science Basis. Contribution of Working Group I to the Sixth Assessment Report of the Intergovernmental Panel on Climate Change*. Ed. by V. Masson-Delmotte, P. Zhai, A. Pirani, S.L. Connors, C. Péan, S. Berger, N. Caud, Y. Chen, L. Goldfarb, M.I. Gomis, M. Huang, K. Leitzell, E. Lonnoy, J.B.R. Matthews, T.K. Maycock, T. Waterfield, O. Yelekçi, R. Yu, and B. Zhou. Cambridge, United Kingdom and New York, NY, USA: Cambridge University Press, 3-32. DOI: 10.1017/9781009157896.001.

Jackson, L. C., R. Kahana, T. Graham, M. A. Ringer, T. Woollings, J. V. Mecking, and R. A. Wood (Dec. 2015). "Global and European climate impacts of a slowdown of the AMOC in a high resolution GCM". en. In: *Climate Dynamics* 45.11-12, pp. 3299–3316. ISSN: 0930-7575, 1432-0894. DOI: 10.1007/s00382-015-2540-2. URL: http://link.springer.com/10.1007/s00382-015-2540-2 (visited on 02/06/2023).

Jakobsson, Martin, Kelly A. Hogan, Larry A. Mayer, Alan Mix, Anne Jennings, Joe Stoner, Björn Eriksson, Kevin Jerram, Rezwan Mohammad, Christof Pearce, Brendan Reilly, and Christian Stranne (May 2018). "The Holocene retreat dynamics and stability of Petermann Glacier in northwest Greenland". en. In: *Nature Communications* 9.1, p. 2104. ISSN: 2041-1723. DOI: 10.1038/s41467-018-04573-2. URL: https://www.nature.com/articles/s41467-018-04573-2 (visited on 01/19/2023).

Jewell, Jessica and Aleh Cherp (Jan. 2020). "On the political feasibility of climate change mitigation pathways: Is it too late to keep warming below 1.5°C?" en. In: *WIREs Climate Change* 11.1. ISSN: 1757-7780, 1757-7799. DOI: 10.1002/wcc.621. URL: https://onlinelibrary.wiley.com/doi/10.1002/wcc.621 (visited on 03/12/2023).

Jorgenson, M.T. (2013). "Volume 8: Glacial and Periglacial Geomorphology". In: *Treatise on Geomorphology Vol.* Ed. by R. Giardino and J. Harbor. New York: Academic Press, pp. 313–324. ISBN: 9780080885223.

Keil, Paul, Thorsten Mauritsen, Johann Jungclaus, Christopher Hedemann, Dirk Olonscheck, and Rohit Ghosh (July 2020). "Multiple drivers of the North Atlantic warming hole". en. In: *Nature Climate Change* 10.7, pp. 667–671. ISSN: 1758-678X, 1758-6798. DOI: 10.1038/s41558-020-0819-8. URL: http://www.nature.com/articles/s41558-020-0819-8 (visited on 03/05/2023).

Khan, Shfaqat A, Andy Aschwanden, Anders A Bjørk, John Wahr, Kristian K Kjeldsen, and Kurt H Kjær (Apr. 2015). "Greenland ice sheet mass balance: a review". en. In: *Reports on Progress in Physics* 78.4, p. 046801. ISSN: 0034-4885, 1361-6633. DOI: 10.1088/0034-4885/78/4/046801. URL: https://iopscience.iop.org/article/10.1088/0034-4885/78/4/046801 (visited on 01/17/2023).

Khan, Shfaqat A., Anders A. Bjørk, Jonathan L. Bamber, Mathieu Morlighem, Michael Bevis, Kurt H. Kjær, Jérémie Mouginot, Anja Løkkegaard, David M. Holland, Andy Aschwanden, Bao Zhang, Veit Helm, Niels J. Korsgaard, William Colgan, Nicolaj K. Larsen, Lin Liu, Karina Hansen, Valentina Barletta, Trine S. Dahl-Jensen, Anne Sofie Søndergaard, Beata M. Csatho, Ingo Sasgen, Jason Box, and Toni Schenk (Nov. 2020). "Centennial response of Greenland's three largest outlet glaciers". en. In: *Nature Communications* 11.1, p. 5718. ISSN: 2041-1723. DOI: 10.1038/s41467-020-19580-5. URL: https://www.nature.com/articles/s41467-020-19580-5 (visited on 01/19/2023).

Khvorostyanov, Dimitry V., P. Ciais, G. Krinner, and S. A. Zimov (2008). "Vulnerability of east Siberia's frozen carbon stores to future warming". In: *Geophysical Research Letters* 35.10, pp. 1–5. ISSN: 00948276. DOI: 10.1029/2008GL033639.

King, Michalea D., Ian M. Howat, Salvatore G. Candela, Myoung J. Noh, Seongsu Jeong, Brice P. Y. Noël, Michiel R. van den Broeke, Bert Wouters, and Adelaide Negrete (Aug. 2020). "Dynamic ice loss from the Greenland Ice Sheet driven by sustained glacier retreat". en. In: *Communications Earth & Environment* 1.1, p. 1. ISSN: 2662-4435. DOI: 10.1038/s43247-020-0001-2. URL: https://www.nature.com/articles/s43247-020-0001-2 (visited on 01/09/2023).

Kokelj, S. V. and M. T. Jorgenson (2013). "Advances in thermokarst research". In: *Permafrost and Periglacial Processes* 24.2, pp. 108–119. ISSN: 10456740. DOI: 10.1002/ppp.1779.

Kriegler, Elmar, Jim W. Hall, Hermann Held, Richard Dawson, and Hans Joachim Schellnhuber (2009). "Imprecise probability assessment of tipping points in the climate system". In: *Proceedings of the National Academy of Sciences of the United States of America* 106.13, pp. 5041–5046. ISSN: 00278424. DOI: 10.1073/pnas.0809117106.

Kuhlbrodt, T., A. Griesel, M. Montoya, A. Levermann, M. Hofmann, and S. Rahmstorf (Apr. 2007). "On the driving processes of the Atlantic meridional overturning circulation". en. In: *Reviews of Geophysics* 45.2, RG2001. ISSN: 8755-1209. DOI: 10.1029/2004RG000166. URL: http://doi.wiley.com/10.1029/2004RG000166 (visited on 02/06/2023).

Larrasoaña, Juan C., Andrew P. Roberts, and Eelco J. Rohling (Oct. 2013). "Dynamics of Green Sahara Periods and Their Role in Hominin Evolution". en. In: *PLoS ONE* 8.10. Ed. by Michael D. Petraglia, e76514. ISSN: 1932-6203. DOI: 10.1371/journal.pone.0076514. URL: https://dx.plos.org/10.1371/journal.pone.0076514 (visited on 01/08/2023).

Le Quéré, Corinne, Robbie M. Andrew, Josep G. Canadell, Stephen Sitch, Jan Ivar Korsbakken, Glen P. Peters, Andrew C. Manning, Thomas A. Boden, Pieter P. Tans, Richard A. Houghton, Ralph F. Keeling, Simone Alin, Oliver D. Andrews, Peter Anthoni, Leticia Barbero, Laurent Bopp, Frédéric Chevallier, Louise P. Chini, Philippe Ciais, Kim Currie, Christine Delire, Scott C. Doney, Pierre Friedlingstein, Thanos Gkritzalis, Ian Harris, Judith Hauck, Vanessa Haverd, Mario Hoppema, Kees Klein Goldewijk, Atul K. Jain,

Etsushi Kato, Arne Körtzinger, Peter Landschützer, Nathalie Lefèvre, Andrew Lenton, Sebastian Lienert, Danica Lombardozzi, Joe R. Melton, Nicolas Metzl, Frank Millero, Pedro M.S. Monteiro, David R. Munro, Julia E.M.S. Nabel, Shin Ichiro Nakaoka, Kevin O'Brien, Are Olsen, Abdirahman M. Omar, Tsuneo Ono, Denis Pierrot, Benjamin Poulter, Christian Rödenbeck, Joe Salisbury, Ute Schuster, Jörg Schwinger, Roland Séférian, Ingunn Skjelvan, Benjamin D. Stocker, Adrienne J. Sutton, Taro Takahashi, Hanqin Tian, Bronte Tilbrook, Ingrid T. Van Der Laan-Luijkx, Guido R. Van Der Werf, Nicolas Viovy, Anthony P. Walker, Andrew J. Wiltshire, and Sönke Zaehle (2016). "Global Carbon Budget 2016". In: *Earth System Science Data* 8.2, pp. 605–649. ISSN: 18663516. DOI: 10.5194/essd-8-605-2016.

Leach, Nicholas J., Stuart Jenkins, Zebedee Nicholls, Christopher J. Smith, John Lynch, Michelle Cain, Tristram Walsh, Bill Wu, Junichi Tsutsui, and Myles R. Allen (2021). "FaIRv2.0.0: A generalized impulse response model for climate uncertainty and future scenario exploration". In: *Geoscientific Model Development* 14.5, pp. 3007–3036. ISSN: 19919603. DOI: 10.5194/gmd-14-3007-2021.

Lee, J.-Y., J. Marotzke, G. Bala, L. Cao, S. Corti, J.P. Dunne, F. Engelbrecht, E. Fischer, J.C. Fyfe, C. Jones, A. Maycock, J. Mutemi, O. Ndiaye, S. Panickal, and T. Zhou (2021). "Future Global Climate: Scenario-Based Projections and Near-Term Information". In: *Climate Change 2021: The Physical Science Basis. Contribution of Working Group I to the Sixth Assessment Report of the Intergovernmental Panel on Climate Change*. Ed. by V. Masson-Delmotte, P. Zhai, A. Pirani, S.L. Connors, C. Péan, S. Berger, N. Caud, Y. Chen, L. Goldfarb, M.I. Gomis, M. Huang, K. Leitzell, E. Lonnoy, J.B.R. Matthews, T.K. Maycock, T. Waterfield, O. Yelekçi, R. Yu, and B. Zhou. Cambridge, United Kingdom and New York, NY, USA: Cambridge University Press, pp. 553–672. DOI: 10.1017/9781009157896.006.

Lehner, Flavio, Clara Deser, Nicola Maher, Jochem Marotzke, Erich M. Fischer, Lukas Brunner, Reto Knutti, and Ed Hawkins (May 2020). "Partitioning climate projection uncertainty with multiple large ensembles and CMIP5/6". en. In: *Earth System Dynamics* 11.2, pp. 491–508. ISSN: 2190-4987. DOI: 10.5194/esd-11-491-2020. URL: https://esd.copernicus.org/articles/11/491/2020/ (visited on 03/01/2023).

Lenton, Timothy M (2012). "Arctic Climate Tipping Points". In: pp. 10–22. DOI: 10.1007/s13280-011-0221-x.

Lenton, Timothy M, Johan Rockström, Owen Gaffney, Stefan Rahmstorf, Katherine Richardson, Will Steffen, and Hans Joachim Schellnhuber (2019). "Climate tipping points — too risky to bet against". In: *Nature* 575, pp. 592–595.

Lenton, Timothy M. (2011). "Early warning of climate tipping points". In: *Nature Climate Change* 1.4, pp. 201–209. ISSN: 1758678X. DOI: 10.1038/nclimate1143.

Lenton, Timothy M., Hermann Held, Elmar Kriegler, Jim W. Hall, Wolfgang Lucht, Stefan Rahmstorf, and Hans Joachim Schellnhuber (Feb. 2008). "Tipping elements in the Earth's

climate system". In: *Proceedings of the National Academy of Sciences* 105.6, pp. 1786–1793. ISSN: 0027-8424. DOI: 10.1073/pnas.0705414105. URL: https://pnas.org/doi/full/10.1073/pnas.0705414105.

Levermann, Anders, Jonathan L. Bamber, Sybren Drijfhout, Andrey Ganopolski, Winfried Haeberli, Neil R.P. Harris, Matthias Huss, Kirstin Krueger, Timothy M. Lenton, Ronald W. Lindsay, Dirk Notz, Peter Wadhams, and Susanne Weber (2012). "Potential climatic transitions with profound impact on Europe". In: *Climatic Change* 110.3-4, pp. 845–878. ISSN: 01650009. DOI: 10.1007/s10584-011-0126-5.

Lindgren, Amelie, Gustaf Hugelius, and Peter Kuhry (2018). "Extensive loss of past permafrost carbon but a net accumulation into present-day soils". In: *Nature* 560.7717, pp. 219–222. ISSN: 14764687. DOI: 10.1038/s41586-018-0371-0. URL: http://dx.doi.org/10.1038/s41586-018-0371-0.

Liu, Wei, Zhengyu Liu, and Esther C. Brady (Mar. 2014). "Why is the AMOC Monostable in Coupled General Circulation Models?" en. In: *Journal of Climate* 27.6, pp. 2427–2443. ISSN: 0894-8755, 1520-0442. DOI: 10.1175/JCLI-D-13-00264.1. URL: http://journals.ametsoc.org/doi/10.1175/JCLI-D-13-00264.1 (visited on 02/06/2023).

Liu, Wei, Shang-Ping Xie, Zhengyu Liu, and Jiang Zhu (Jan. 2017). "Overlooked possibility of a collapsed Atlantic Meridional Overturning Circulation in warming climate". en. In: *Science Advances* 3.1, e1601666. ISSN: 2375-2548. DOI: 10.1126/sciadv.1601666. URL: https://www.science.org/doi/10.1126/sciadv.1601666 (visited on 02/06/2023).

Lohmann, Johannes and Peter D. Ditlevsen (Mar. 2021). "Risk of tipping the overturning circulation due to increasing rates of ice melt". en. In: *Proceedings of the National Academy of Sciences* 118.9, e2017989118. ISSN: 0027-8424, 1091-6490. DOI: 10.1073/pnas.2017989118. URL: https://pnas.org/doi/full/10.1073/pnas.2017989118 (visited on 02/06/2023).

Lontzek, Thomas S., Yongyang Cai, Kenneth L. Judd, and Timothy M. Lenton (May 2015). "Stochastic integrated assessment of climate tipping points indicates the need for strict climate policy". en. In: *Nature Climate Change* 5.5, pp. 441–444. ISSN: 1758-678X, 1758-6798. DOI: 10.1038/nclimate2570. URL: http://www.nature.com/articles/nclimate2570 (visited on 03/11/2023).

Luke, C. M. and P. M. Cox (2011). "Soil carbon and climate change: From the Jenkinson effect to the compost-bomb instability". In: *European Journal of Soil Science* 62.1, pp. 5–12. ISSN: 13510754. DOI: 10.1111/j.1365-2389.2010.01312.x.

McGuire, A. David, David M. Lawrence, Charles Koven, Joy S. Clein, Eleanor Burke, Guangsheng Chen, Elchin Jafarov, Andrew H. MacDougall, Sergey Marchenko, Dmitry Nicolsky, Shushi Peng, Annette Rinke, Philippe Ciais, Isabelle Gouttevin, Daniel J. Hayes, Duoying Ji, Gerhard Krinner, John C. Moore, Vladimir Romanovsky, Christina Schädel, Kevin Schaefer, Edward A.G. Schuur, and Qianlai Zhuang (2018). "Dependence of the

evolution of carbon dynamics in the northern permafrost region on the trajectory of climate change". In: *Proceedings of the National Academy of Sciences of the United States of America* 115.15, pp. 3882–3887. ISSN: 10916490. DOI: 10.1073/pnas.1719903115.

McKay, M. D., R. J. Beckman, and W. J. Conover (1979). "A Comparison of Three Methods for Selecting Values of Input Variables in the Analysis of Output from a Computer Code". In: *Technometrics* 21.2. Publisher: [Taylor & Francis, Ltd., American Statistical Association, American Society for Quality], pp. 239–245. ISSN: 00401706. DOI: 10.2307/1268522. URL: http://www.jstor.org/stable/1268522 (visited on 02/04/2023).

Meehl, Gerald A., Catherine A. Senior, Veronika Eyring, Gregory Flato, Jean-Francois Lamarque, Ronald J. Stouffer, Karl E. Taylor, and Manuel Schlund (June 2020). "Context for interpreting equilibrium climate sensitivity and transient climate response from the CMIP6 Earth system models". en. In: *Science Advances* 6.26, eaba1981. ISSN: 2375-2548. DOI: 10.1126/sciadv.aba1981. URL: https://www.science.org/doi/10.1126/sciadv.aba1981 (visited on 03/02/2023).

Meier, Mark F., Mark B. Dyurgerov, Ursula K. Rick, Shad O'Neel, W. Tad Pfeffer, Robert S. Anderson, Suzanne P. Anderson, and Andrey F. Glazovsky (Aug. 2007). "Glaciers Dominate Eustatic Sea-Level Rise in the 21st Century". en. In: *Science* 317.5841, pp. 1064–1067. ISSN: 0036-8075, 1095-9203. DOI: 10.1126/science.1143906. URL: https://www.science.org/doi/10.1126/science.1143906 (visited on 01/30/2023).

Meier, Walter N., Greta K. Hovelsrud, Bob E.H. van Oort, Jeffrey R. Key, Kit M. Kovacs, Christine Michel, Christian Haas, Mats A. Granskog, Sebastian Gerland, Donald K. Perovich, Alexander Makshtas, and James D. Reist (Sept. 2014). "Arctic sea ice in transformation: A review of recent observed changes and impacts on biology and human activity: ARCTIC SEA ICE: REVIEW OF RECENT CHANGES". en. In: *Reviews of Geophysics* 52.3, pp. 185–217. ISSN: 87551209. DOI: 10.1002/2013RG000431. URL: http://doi.wiley.com/10.1002/2013RG000431 (visited on 01/23/2023).

Meinshausen, Malte, Jared Lewis, Christophe McGlade, Johannes Gütschow, Zebedee Nicholls, Rebecca Burdon, Laura Cozzi, and Bernd Hackmann (Apr. 2022). "Realization of Paris Agreement pledges may limit warming just below 2 °C". en. In: *Nature* 604.7905, pp. 304–309. ISSN: 0028-0836, 1476-4687. DOI: 10.1038/s41586-022-04553-z. URL: https://www.nature.com/articles/s41586-022-04553-z (visited on 03/09/2023).

Meinshausen, Malte, Zebedee R.J. Nicholls, Jared Lewis, Matthew J. Gidden, Elisabeth Vogel, Mandy Freund, Urs Beyerle, Claudia Gessner, Alexander Nauels, Nico Bauer, Josep G. Canadell, John S. Daniel, Andrew John, Paul B. Krummel, Gunnar Luderer, Nicolai Meinshausen, Stephen A. Montzka, Peter J. Rayner, Stefan Reimann, Steven J. Smith, Marten Van Den Berg, Guus J.M. Velders, Martin K. Vollmer, and Ray H.J. Wang (2020). "The shared socio-economic pathway (SSP) greenhouse gas concentrations and

their extensions to 2500". In: *Geoscientific Model Development* 13.8, pp. 3571–3605. ISSN: 19919603. DOI: 10.5194/gmd-13-3571-2020.

Meinshausen, Malte, S. J. Smith, K. Calvin, J. S. Daniel, M. L.T. Kainuma, J. Lamarque, K. Matsumoto, S. A. Montzka, S. C.B. Raper, K. Riahi, A. Thomson, G. J.M. Velders, and D. P.P. van Vuuren (2011). "The RCP greenhouse gas concentrations and their extensions from 1765 to 2300". In: *Climatic Change* 109.1, pp. 213–241. ISSN: 01650009. DOI: 10.1007/s10584-011-0156-z.

Mengel, M. and A. Levermann (June 2014). "Ice plug prevents irreversible discharge from East Antarctica". en. In: *Nature Climate Change* 4.6, pp. 451–455. ISSN: 1758-678X, 1758-6798. DOI: 10.1038/nclimate2226. URL: http://www.nature.com/articles/nclimate2226 (visited on 01/20/2023).

Metropolis, Nicholas, Arianna W. Rosenbluth, Marshall N. Rosenbluth, Augusta H. Teller, and Edward Teller (June 1953). "Equation of State Calculations by Fast Computing Machines". en. In: *The Journal of Chemical Physics* 21.6, pp. 1087–1092. ISSN: 0021-9606, 1089-7690. DOI: 10.1063/1.1699114. URL: http://aip.scitation.org/doi/10.1063/1.1699114 (visited on 03/03/2023).

Millar, J. Richard, Zebedee R. Nicholls, Pierre Friedlingstein, and Myles R. Allen (2017). "A modified impulse-response representation of the global near-surface air temperature and atmospheric concentration response to carbon dioxide emissions". In: *Atmospheric Chemistry and Physics* 17.11, pp. 7213–7228. ISSN: 16807324. DOI: 10.5194/acp-17-7213-2017.

Milner, Alexander M., Kieran Khamis, Tom J. Battin, John E. Brittain, Nicholas E. Barrand, Leopold Füreder, Sophie Cauvy-Fraunié, Gísli Már Gíslason, Dean Jacobsen, David M. Hannah, Andrew J. Hodson, Eran Hood, Valeria Lencioni, Jón S. Ólafsson, Christopher T. Robinson, Martyn Tranter, and Lee E. Brown (Sept. 2017). "Glacier shrinkage driving global changes in downstream systems". en. In: *Proceedings of the National Academy of Sciences* 114.37, pp. 9770–9778. ISSN: 0027-8424, 1091-6490. DOI: 10.1073/pnas.1619807114. URL: https://pnas.org/doi/full/10.1073/pnas.1619807114 (visited on 01/30/2023).

Mishra, Umakant, Gustaf Hugelius, Eitan Shelef, Yuanhe Yang, Jens Strauss, Alexey Lupachev, Jennifer W. Harden, Julie D. Jastrow, Chien Lu Ping, William J. Riley, Edward A.G. Schuur, Roser Matamala, Matthias Siewert, Lucas E. Nave, Charles D. Koven, Matthias Fuchs, Juri Palmtag, Peter Kuhry, Claire C. Treat, Sebastian Zubrzycki, Forrest M. Hoffman, Bo Elberling, Philip Camill, Alexandra Veremeeva, and Andrew Orr (2021). "Spatial heterogeneity and environmental predictors of permafrost region soil organic carbon stocks". In: *Science Advances* 7.9, pp. 1–13. ISSN: 23752548. DOI: 10.1126/sciadv.aaz5236.

Morlighem, M., C. N. Williams, E. Rignot, L. An, J. E. Arndt, J. L. Bamber, G. Catania, N. Chauché, J. A. Dowdeswell, B. Dorschel, I. Fenty, K. Hogan, I. Howat, A. Hubbard,

M. Jakobsson, T. M. Jordan, K. K. Kjeldsen, R. Millan, L. Mayer, J. Mouginot, B. P. Y. Noël, C. O'Cofaigh, S. Palmer, S. Rysgaard, H. Seroussi, M. J. Siegert, P. Slabon, F. Straneo, M. R. van den Broeke, W. Weinrebe, M. Wood, and K. B. Zinglersen (Nov. 2017). "BedMachine v3: Complete Bed Topography and Ocean Bathymetry Mapping of Greenland From Multibeam Echo Sounding Combined With Mass Conservation". en. In: *Geophysical Research Letters* 44.21. ISSN: 0094-8276, 1944-8007. DOI: 10.1002/2017GL074954. URL: https://onlinelibrary.wiley.com/doi/10.1002/2017GL074954 (visited on 01/17/2023).

Mouginot, Jérémie, Eric Rignot, Anders A. Bjørk, Michiel van den Broeke, Romain Millan, Mathieu Morlighem, Brice Noël, Bernd Scheuchl, and Michael Wood (May 2019). "Forty-six years of Greenland Ice Sheet mass balance from 1972 to 2018". en. In: *Proceedings of the National Academy of Sciences* 116.19, pp. 9239–9244. ISSN: 0027-8424, 1091-6490. DOI: 10.1073/pnas.1904242116. URL: https://pnas.org/doi/full/10.1073/pnas.1904242116 (visited on 01/17/2023).

Myhre G.and Shindell, D., F.-M. Bréon, J. Collins W.and Fuglestvedt, J. Huang, D. Koch, J.-F. Lamarque, B. Lee D.and Mendoza, A. Nakajima T.and Robock, G. Stephens, T. Takemura, and H. Zhang (2013). "Anthropogenic and Natural Radiative Forcing". In: *Climate Change 2013: The Physical Science Basis. Contribution of Working Group I to the Fifth Assessment Report of the Intergovernmental Panel on Climate Change*. Ed. by T. F. Stocker, D. Qin, G.-K. Plattner, M. Tignor, S. K. Allen, J. Boschung, A. Nauels, Y. Xia, V. Bex, and P. M. Midgley. Cambridge, United Kingdom and New York, NY, USA: Cambridge University Press. Chap. 8, pp. 650–740. URL: https://doi.org/10.1017/CBO9781107415324.018.

Nicholls, Z. R. J., M. Meinshausen, J. Lewis, R. Gieseke, D. Dommenget, K. Dorheim, C.-S. Fan, J. S. Fuglestvedt, T. Gasser, U. Golueke, P. Goodwin, C. Hartin, A. P. Hope, E. Kriegler, N. J. Leach, D. Marchegiani, L. A. McBride, Y. Quilcaille, J. Rogelj, R. J. Salawitch, B. H. Samset, M. Sandstad, A. N. Shiklomanov, R. B. Skeie, C. J. Smith, S. Smith, K. Tanaka, J. Tsutsui, and Z. Xie (2020). "Reduced Complexity Model Intercomparison Project Phase 1: introduction and evaluation of global-mean temperature response". In: *Geoscientific Model Development* 13.11, pp. 5175–5190. DOI: 10.5194/gmd-13-5175-2020. URL: https://gmd.copernicus.org/articles/13/5175/2020/.

Nicholson, Sharon E. (Sept. 2018). "Climate of the Sahel and West Africa". en. In: *Oxford Research Encyclopedia of Climate Science*. Oxford University Press. ISBN: 978-0-19-022862-0. DOI: 10.1093/acrefore/9780190228620.013.510. URL: http://climatescience.oxfordre.com/view/10.1093/acrefore/9780190228620.001.0001/acrefore-9780190228620-e-510 (visited on 01/08/2023).

Nobre, Carlos A., Gilvan Sampaio, Laura S. Borma, Juan Carlos Castilla-Rubio, José S. Silva, and Manoel Cardoso (2016). "Land-use and climate change risks in the amazon and the need of a novel sustainable development paradigm". In: *Proceedings of the National Academy*

*of Sciences of the United States of America* 113.39, pp. 10759–10768. ISSN: 10916490. DOI: 10.1073/pnas.1605516113.

Nobre, Carlos A., Piers J. Sellers, and Jagadish Shukla (1991). "Amazonian Deforestation and Regional Climate Change". In: *Journal of Climate* 4.10, pp. 957–988. ISSN: 0894-8755. DOI: 10.1175/1520-0442(1991)004<0957:adarcc>2.0.co;2.

Noël, B., L. van Kampenhout, J. T. M. Lenaerts, W. J. van de Berg, and M. R. van den Broeke (Mar. 2021). "A 21st Century Warming Threshold for Sustained Greenland Ice Sheet Mass Loss". en. In: *Geophysical Research Letters* 48.5. ISSN: 0094-8276, 1944-8007. DOI: 10.1029/2020GL090471. URL: https://onlinelibrary.wiley.com/doi/10.1029/2020GL090471 (visited on 01/09/2023).

Notz, Dirk (Dec. 2009). "The future of ice sheets and sea ice: Between reversible retreat and unstoppable loss". en. In: *Proceedings of the National Academy of Sciences* 106.49, pp. 20590–20595. ISSN: 0027-8424, 1091-6490. DOI: 10.1073/pnas.0902356106. URL: https://pnas.org/doi/full/10.1073/pnas.0902356106 (visited on 01/23/2023).

Notz, Dirk and Simip Community (May 2020). "Arctic Sea Ice in CMIP6". en. In: *Geophysical Research Letters* 47.10. ISSN: 0094-8276, 1944-8007. DOI: 10.1029/2019GL086749. URL: https://onlinelibrary.wiley.com/doi/10.1029/2019GL086749 (visited on 01/24/2023).

O'Neill, Brian C., Elmar Kriegler, Kristie L. Ebi, Eric Kemp-Benedict, Keywan Riahi, Dale S. Rothman, Bas J. van Ruijven, Detlef P. van Vuuren, Joern Birkmann, Kasper Kok, Marc Levy, and William Solecki (2015). "The roads ahead: Narratives for shared socioeconomic pathways describing world futures in the 21st century". In: *Global Environmental Change* 42, pp. 169–180. ISSN: 09593780. DOI: 10.1016/j.gloenvcha.2015.01.004. URL: http://dx.doi.org/10.1016/j.gloenvcha.2015.01.004.

O'Neill, Brian C., Claudia Tebaldi, Detlef P. Van Vuuren, Veronika Eyring, Pierre Friedlingstein, George Hurtt, Reto Knutti, Elmar Kriegler, Jean Francois Lamarque, Jason Lowe, Gerald A. Meehl, Richard Moss, Keywan Riahi, and Benjamin M. Sanderson (2016). "The Scenario Model Intercomparison Project (ScenarioMIP) for CMIP6". In: *Geoscientific Model Development* 9.9, pp. 3461–3482. ISSN: 19919603. DOI: 10.5194/gmd-9-3461-2016.

Obu, Jaroslav, Sebastian Westermann, Annett Bartsch, Nikolai Berdnikov, Hanne H. Christiansen, Avirmed Dashtseren, Reynald Delaloye, Bo Elberling, Bernd Etzelmüller, Alexander Kholodov, Artem Khomutov, Andreas Kääb, Marina O. Leibman, Antoni G. Lewkowicz, Santosh K. Panda, Vladimir Romanovsky, Robert G. Way, Andreas Westergaard-Nielsen, Tonghua Wu, Jambaljav Yamkhin, and Defu Zou (2019). "Northern Hemisphere permafrost map based on TTOP modelling for 2000–2016 at 1 km2 scale". In: *Earth-Science Reviews* 193.March, pp. 299–316. ISSN: 00128252. DOI: 10.1016/j.earscirev.2019.04.023. URL: https://doi.org/10.1016/j.earscirev.2019.04.023.

Oechel, Walter C., George L. Vourlitis, Steven J. Hastings, Rommel C. Zuluete, Larry Maxman, and Douglas Kane (2000). "Acclimation of ecosystem CO2 exchange in the Alaskan Arctic in response to decadal climate warming". In: *Nature* 406.6799, pp. 978–981. ISSN: 00280836. DOI: 10.1038/35023137.

Olefeldt, D., S. Goswami, G. Grosse, D. Hayes, G. Hugelius, P. Kuhry, A. D. Mcguire, V. E. Romanovsky, A. B.K. Sannel, E. A.G. Schuur, and M. R. Turetsky (2016). "Circumpolar distribution and carbon storage of thermokarst landscapes". In: *Nature Communications* 7, pp. 1–11. ISSN: 20411723. DOI: 10.1038/ncomms13043. URL: http://dx.doi.org/10.1038/ncomms13043.

Onarheim, Ingrid H. and Marius Årthun (2017). "Toward an ice-free Barents Sea". en. In: *Geophysical Research Letters* 44.16, pp. 8387–8395. ISSN: 1944-8007. DOI: 10.1002/2017GL074304. URL: https://onlinelibrary.wiley.com/doi/abs/10.1002/2017GL074304 (visited on 01/24/2023).

Pan, Yude, Richard A. Birdsey, Jingyun Fang, Richard Houghton, Pekka E. Kauppi, Werner A. Kurz, Oliver L. Phillips, Anatoly Shvidenko, Simon L. Lewis, Josep G. Canadell, Philippe Ciais, Robert B. Jackson, Stephen W. Pacala, A. David McGuire, Shilong Piao, Aapo Rautiainen, Stephen Sitch, and Daniel Hayes (Aug. 2011). "A Large and Persistent Carbon Sink in the World's Forests". en. In: *Science* 333.6045, pp. 988–993. ISSN: 0036-8075, 1095-9203. DOI: 10.1126/science.1201609. URL: https://www.science.org/doi/10.1126/science.1201609 (visited on 01/05/2023).

Parry, Isobel, Paul Ritchie, and Peter Cox (2022). "Evidence of Amazon rainforest dieback in CMIP6 models". In: *EGUsphere*, pp. 1–11. arXiv: 2203.11744. URL: http://arxiv.org/abs/2203.11744.

Pattyn, Frank (July 2018). "The paradigm shift in Antarctic ice sheet modelling". en. In: *Nature Communications* 9.1, p. 2728. ISSN: 2041-1723. DOI: 10.1038/s41467-018-05003-z. URL: https://www.nature.com/articles/s41467-018-05003-z (visited on 01/18/2023).

Pausata, Francesco S.R., Marco Gaetani, Gabriele Messori, Alexis Berg, Danielle Maia de Souza, Rowan F. Sage, and Peter B. deMenocal (Mar. 2020). "The Greening of the Sahara: Past Changes and Future Implications". en. In: *One Earth* 2.3, pp. 235–250. ISSN: 25903322. DOI: 10.1016/j.oneear.2020.03.002. URL: https://linkinghub.elsevier.com/retrieve/pii/S2590332220301007 (visited on 01/07/2023).

Radić, Valentina and Regine Hock (Feb. 2011). "Regionally differentiated contribution of mountain glaciers and ice caps to future sea-level rise". en. In: *Nature Geoscience* 4.2, pp. 91–94. ISSN: 1752-0894, 1752-0908. DOI: 10.1038/ngeo1052. URL: http://www.nature.com/articles/ngeo1052 (visited on 01/30/2023).

Rahmstorf, Stefan (Sept. 2002). "Ocean circulation and climate during the past 120,000 years". en. In: *Nature* 419.6903, pp. 207–214. ISSN: 0028-0836, 1476-4687. DOI: 10.1038/nature01090. URL: http://www.nature.com/articles/nature01090 (visited on 02/06/2023).

Riahi, Keywan, Detlef P. van Vuuren, Elmar Kriegler, Jae Edmonds, Brian C. O'Neill, Shinichiro Fujimori, Nico Bauer, Katherine Calvin, Rob Dellink, Oliver Fricko, Wolfgang Lutz, Alexander Popp, Jesus Crespo Cuaresma, Samir KC, Marian Leimbach, Leiwen Jiang, Tom Kram, Shilpa Rao, Johannes Emmerling, Kristie Ebi, Tomoko Hasegawa, Petr Havlik, Florian Humpenöder, Lara Aleluia Da Silva, Steve Smith, Elke Stehfest, Valentina Bosetti, Jiyong Eom, David Gernaat, Toshihiko Masui, Joeri Rogelj, Jessica Strefler, Laurent Drouet, Volker Krey, Gunnar Luderer, Mathijs Harmsen, Kiyoshi Takahashi, Lavinia Baumstark, Jonathan C. Doelman, Mikiko Kainuma, Zbigniew Klimont, Giacomo Marangoni, Hermann Lotze-Campen, Michael Obersteiner, Andrzej Tabeau, and Massimo Tavoni (2016). "The Shared Socioeconomic Pathways and their energy, land use, and greenhouse gas emissions implications: An overview". In: *Global Environmental Change* 42, pp. 153–168. ISSN: 09593780. DOI: 10.1016/j.gloenvcha.2016.05.009.

Rignot, E., J. Mouginot, M. Morlighem, H. Seroussi, and B. Scheuchl (2014). "Widespread, rapid grounding line retreat of Pine Island, Thwaites, Smith, and Kohler glaciers, West Antarctica, from 1992 to 2011". In: *Geophysical Research Letters* 41.10, pp. 3502–3509. ISSN: 19448007. DOI: 10.1002/2014GL060140.

Rignot, Eric, Jérémie Mouginot, Bernd Scheuchl, Michiel van den Broeke, Melchior J. van Wessem, and Mathieu Morlighem (Jan. 2019). "Four decades of Antarctic Ice Sheet mass balance from 1979–2017". en. In: *Proceedings of the National Academy of Sciences* 116.4, pp. 1095–1103. ISSN: 0027-8424, 1091-6490. DOI: 10.1073/pnas.1812883116. URL: https://pnas.org/doi/full/10.1073/pnas.1812883116 (visited on 01/20/2023).

Ritchie, Paul D.L., Joseph J. Clarke, Peter M. Cox, and Chris Huntingford (2021). "Overshooting tipping point thresholds in a changing climate". In: *Nature* 592.7855. Publisher: Springer US, pp. 517–523. ISSN: 14764687. DOI: 10.1038/s41586-021-03263-2. URL: http://dx.doi.org/10.1038/s41586-021-03263-2.

Robinson, Alexander, Reinhard Calov, and Andrey Ganopolski (June 2012). "Multistability and critical thresholds of the Greenland ice sheet". en. In: *Nature Climate Change* 2.6, pp. 429–432. ISSN: 1758-678X, 1758-6798. DOI: 10.1038/nclimate1449. URL: http://www.nature.com/articles/nclimate1449 (visited on 01/09/2023).

Ryan, Kevin (2002). "Dynamic interactions between forest structure and fire behavior in boreal ecosystems". en. In: *Silva Fennica* 36.1. ISSN: 22424075. DOI: 10.14214/sf.548. URL: https://www.silvafennica.fi/article/548 (visited on 01/06/2023).

Sanderson, Benjamin M. and A. Rosie A. Fisher (2020). "A fiery wake-up call for climate science". In: *Nature Climate Change* 10.3, pp. 173–183. ISSN: 17586798. DOI: 10.1038/s41558-020-0712-5.

Schaner, Neil, Nathalie Voisin, Bart Nijssen, and Dennis P Lettenmaier (Sept. 2012). "The contribution of glacier melt to streamflow". en. In: *Environmental Research Letters* 7.3, p. 034029. ISSN: 1748-9326. DOI: 10.1088/1748-9326/7/3/034029. URL: https://iopscience.iop.org/article/10.1088/1748-9326/7/3/034029 (visited on 01/30/2023).

Scheffer, Marten, Marina Hirota, Milena Holmgren, Egbert H. Van Nes, and F. Stuart Chapin (2012). "Thresholds for boreal biome transitions". In: *Proceedings of the National Academy of Sciences of the United States of America* 109.52, pp. 21384–21389. ISSN: 00278424. DOI: 10.1073/pnas.1219844110.

Schellnhuber, Hans Joachim, Stefan Rahmstorf, and Ricarda Winkelmann (2016). "Why the right climate target was agreed in Paris". In: *Nature Climate Change* 6.7, pp. 649–653. ISSN: 17586798. DOI: 10.1038/nclimate3013.

Schirrmeister, L., D. Froese, V. Tumskoy, G. Grosse, and S. Wetterich (2013). "PERMAFROST AND PERIGLACIAL FEATURES | Yedoma: Late Pleistocene Ice-Rich Syngenetic Permafrost of Beringia". In: *Encyclopedia of Quaternary Science (Second Edition)*. Ed. by Scott A. Elias and Cary J. Mock. Second Edition. Amsterdam: Elsevier, pp. 542–552. ISBN: 978-0-444-53642-6. DOI: https://doi.org/10.1016/B978-0-444-53643-3.00106-0. URL: https://www.sciencedirect.com/science/article/pii/B9780444536433001060.

Schneider von Deimling, T., G. Grosse, J. Strauss, L. Schirrmeister, A. Morgenstern, S. Schaphoff, M. Meinshausen, and J. Boike (2015). "Observation-based modelling of permafrost carbon fluxes with accounting for deep carbon deposits and thermokarst activity". In: *Biogeosciences* 12.11, pp. 3469–3488. ISSN: 17264189. DOI: 10.5194/bg-12-3469-2015.

Schneider von Deimling, T., M. Meinshausen, A. Levermann, V. Huber, K. Frieler, D. M. Lawrence, and V. Brovkin (2012). "Estimating the near-surface permafrost-carbon feedback on global warming". In: *Biogeosciences* 9.2, pp. 649–665. ISSN: 17264170. DOI: 10.5194/bg-9-649-2012.

Schoof, Christian (2007). "Marine ice-sheet dynamics. Part 1. The case of rapid sliding". In: *Journal of Fluid Mechanics* 573, pp. 27–55. DOI: 10.1017/S0022112006003570.

Schuur, E. A.G., A. D. McGuire, C. Schädel, G. Grosse, J. W. Harden, D. J. Hayes, G. Hugelius, C. D. Koven, P. Kuhry, D. M. Lawrence, S. M. Natali, D. Olefeldt, V. E. Romanovsky, K. Schaefer, M. R. Turetsky, C. C. Treat, and J. E. Vonk (2015). "Climate change and the permafrost carbon feedback". In: *Nature* 520.7546, pp. 171–179. ISSN: 14764687. DOI: 10.1038/nature14338.

Science Panel for the Amazon (2021). *Science Panel for the Amazon Amazon Assessment Report 2021 - Executive Summary*. Ed. by C. Nobre, A. Encalada, E. Anderson, F.H.

Roca Alcazar, M. Bustamante, C. Mena, M. Peña-Claros, G. Poveda, J.P. Rodriguez, S. Saleska, S. Trumbore, A.L. Val, L. Villa Nova, R. Abramovay, A. Alencar, A.C.R. Alzza, D. Armenteras, P. Artaxo, S. Athayde, H.T. Barretto Filho, J. Barlow, E. Berenguer, F. Bortolotto, F.A. Costa, M.H. Costa, N. Cuvi, P.M. Fearnside, J. Ferreira, B.M. Flores, S. Frieri, L.V. Gatti, J.M. Guayasamin, S. Hecht, M. Hirota, C. Hoorn, C. Josse, D.M. Lapola, C. Larrea, D.M. Larrea-Alcazar, Z. Lehm Ardaya, Y. Malhi, J.A. Marengo, M.R. Moraes, P. Moutinho, M.R. Murmis, E.G. Neves, B. Paez, L. Painter, A. Ramos, M.C. Rosero-Peña, M. Schmink, P. Sist, H. Ter Steege, P. Val, H. Van der Voort, M. Varese, and Zapata-Ríos. New York: United Nations Sustainable Development Solutions Network, p. 48. ISBN: 9781734808001.

Serreze, M C, A P Barrett, J C Stroeve, D N Kindig, and M M Holland (2009). "The emergence of surface-based Arctic amplification". en. In: *The Cryosphere*.

Sgubin, Giovanni, Didier Swingedouw, Sybren Drijfhout, Yannick Mary, and Amine Bennabi (Feb. 2017). "Abrupt cooling over the North Atlantic in modern climate models". en. In: *Nature Communications* 8.1, p. 14375. ISSN: 2041-1723. DOI: 10.1038/ncomms14375. URL: https://www.nature.com/articles/ncomms14375 (visited on 02/06/2023).

Shepherd, Andrew, Lin Gilbert, Alan S. Muir, Hannes Konrad, Malcolm McMillan, Thomas Slater, Kate H. Briggs, Aud V. Sundal, Anna E. Hogg, and Marcus E. Engdahl (July 2019). "Trends in Antarctic Ice Sheet Elevation and Mass". en. In: *Geophysical Research Letters* 46.14, pp. 8174–8183. ISSN: 0094-8276, 1944-8007. DOI: 10.1029/2019GL082182. URL: https://onlinelibrary.wiley.com/doi/10.1029/2019GL082182 (visited on 01/18/2023).

Smedsrud, Lars H., Igor Esau, Randi B. Ingvaldsen, Tor Eldevik, Peter M. Haugan, Camille Li, Vidar S. Lien, Are Olsen, Abdirahman M. Omar, Odd H. Otterå, Bjørg Risebrobakken, Anne B. Sandø, Vladimir A. Semenov, and Svetlana A. Sorokina (Sept. 2013). "THE ROLE OF THE BARENTS SEA IN THE ARCTIC CLIMATE SYSTEM". en. In: *Reviews of Geophysics* 51.3, pp. 415–449. ISSN: 8755-1209, 1944-9208. DOI: 10.1002/rog.20017. URL: https://onlinelibrary.wiley.com/doi/10.1002/rog.20017 (visited on 01/24/2023).

Smith, C., Z.R.J. Nicholls, K. Armour, W. Collins, P. Forster, M. Meinshausen, M.D. Palmer, and M. Watanabe (2021). "The Earth's Energy Budget, Climate Feedbacks, and Climate Sensitivity Supplementary Material". In: *Climate Change 2021: The Physical Science Basis. Contribution of Working Group I to the Sixth Assessment Report of the Intergovernmental Panel on Climate Change*. Ed. by V. Masson-Delmotte, P. Zhai, A. Pirani, S.L. Connors, C. Péan, S. Berger, N. Caud, Y. Chen, L. Goldfarb, M.I. Gomis, M. Huang, K. Leitzell, E. Lonnoy, J.B.R. Matthews, T.K. Maycock, T. Waterfield, O. Yelekçi, R. Yu, and B. Zhou. URL: Available%20from%20https://www.ipcc.ch/.

Smith, Christopher J. (2020). "Effective Radiative Forcing Time Series from the Shared Socioeconomic Pathways". In: DOI: 10.5281/zenodo.3973015.

Staal, Arie, Ingo Fetzer, Lan Wang-Erlandsson, Joyce H.C. Bosmans, Stefan C. Dekker, Egbert H. van Nes, Johan Rockström, and Obbe A. Tuinenburg (2020). "Hysteresis of tropical forests in the 21st century". In: *Nature Communications* 11.1, pp. 1–8. ISSN: 20411723. DOI: 10.1038/s41467-020-18728-7. URL: http://dx.doi.org/10.1038/s41467-020-18728-7.

Staal, Arie, Obbe A. Tuinenburg, Joyce H. C. Bosmans, Milena Holmgren, Egbert H. van Nes, Marten Scheffer, Delphine Clara Zemp, and Stefan C. Dekker (June 2018). "Forest-rainfall cascades buffer against drought across the Amazon". en. In: *Nature Climate Change* 8.6, pp. 539–543. ISSN: 1758-678X, 1758-6798. DOI: 10.1038/s41558-018-0177-y. URL: http://www.nature.com/articles/s41558-018-0177-y (visited on 01/10/2023).

Stat, Michael, Emily Morris, and Ruth D. Gates (July 2008). "Functional diversity in coral–dinoflagellate symbiosis". en. In: *Proceedings of the National Academy of Sciences* 105.27, pp. 9256–9261. ISSN: 0027-8424, 1091-6490. DOI: 10.1073/pnas.0801328105. URL: https://pnas.org/doi/full/10.1073/pnas.0801328105 (visited on 01/09/2023).

Steffen, Will, Johan Rockström, Katherine Richardson, Timothy M Lenton, Carl Folke, Diana Liverman, Colin P. Summerhayes, Anthony D. Barnosky, Sarah E. Cornell, Michel Crucifix, Jonathan F. Donges, Ingo Fetzer, Steven J. Lade, Marten Scheffer, Ricarda Winkelmann, and Hans Joachim Schellnhuber (2018). *Trajectories of the Earth System in the Anthropocene*. DOI: 10.1073/pnas.1810141115.

Stokes, Chris R., Nerilie J. Abram, Michael J. Bentley, Tamsin L. Edwards, Matthew H. England, Annie Foppert, Stewart S. R. Jamieson, Richard S. Jones, Matt A. King, Jan T. M. Lenaerts, Brooke Medley, Bertie W. J. Miles, Guy J. G. Paxman, Catherine Ritz, Tina van de Flierdt, and Pippa L. Whitehouse (Aug. 2022). "Response of the East Antarctic Ice Sheet to past and future climate change". en. In: *Nature* 608.7922, pp. 275–286. ISSN: 0028-0836, 1476-4687. DOI: 10.1038/s41586-022-04946-0. URL: https://www.nature.com/articles/s41586-022-04946-0 (visited on 01/19/2023).

Stommel, Henry (May 1961). "Thermohaline Convection with Two Stable Regimes of Flow". en. In: *Tellus* 13.2, pp. 224–230. ISSN: 00402826, 21533490. DOI: 10.1111/j.2153-3490.1961.tb00079.x. URL: http://tellusa.net/index.php/tellusa/article/view/9491 (visited on 02/06/2023).

Storch, Hans von and Francis W. Zwiers (1999). *Statistical Analysis in Climate Research*. Cambridge University Press. DOI: 10.1017/CBO9780511612336.

Strauss, J., L. Schirrmeister, K. Mangelsdorf, L. Eichhorn, S. Wetterich, and U. Herzschuh (2015). "Organic-matter quality of deep permafrost carbon - A study from Arctic Siberia". In: *Biogeosciences* 12.7, pp. 2227–2245. ISSN: 17264189. DOI: 10.5194/bg-12-2227-2015.

Strauss, Jens, Lutz Schirrmeister, Guido Grosse, Daniel Fortier, Gustaf Hugelius, Christian Knoblauch, Vladimir Romanovsky, Christina Schädel, Thomas Schneider von Deimling, Edward A.G. Schuur, Denis Shmelev, Mathias Ulrich, and Alexandra Veremeeva (2017). "Deep Yedoma permafrost: A synthesis of depositional characteristics and carbon vulnerability". In: *Earth-Science Reviews* 172.February, pp. 75–86. ISSN: 00128252. DOI: 10.1016/j.earscirev.2017.07.007.

Stroeve, Julienne and Dirk Notz (Sept. 2018). "Changing state of Arctic sea ice across all seasons". en. In: *Environmental Research Letters* 13.10, p. 103001. ISSN: 1748-9326. DOI: 10.1088/1748-9326/aade56. URL: https://iopscience.iop.org/article/10.1088/1748-9326/aade56 (visited on 01/23/2023).

Swingedouw, Didier, Adrien Bily, Claire Esquerdo, Leonard F. Borchert, Giovanni Sgubin, Juliette Mignot, and Matthew Menary (Nov. 2021). "On the risk of abrupt changes in the North Atlantic subpolar gyre in CMIP6 models". en. In: *Annals of the New York Academy of Sciences* 1504.1, pp. 187–201. ISSN: 0077-8923, 1749-6632. DOI: 10.1111/nyas.14659. URL: https://onlinelibrary.wiley.com/doi/10.1111/nyas.14659 (visited on 03/05/2023).

Teufel, B. and L. Sushama (2019). "Abrupt changes across the Arctic permafrost region endanger northern development". In: *Nature Climate Change* 9.11, pp. 858–862. DOI: 10.1038/s41558-019-0614-6. URL: http://dx.doi.org/10.1038/s41558-019-0614-6.

Thorncroft, Chris D., Hanh Nguyen, Chidong Zhang, and Philippe Peyrillé (Jan. 2011). "Annual cycle of the West African monsoon: regional circulations and associated water vapour transport: Annual Cycle of West African Monsoon". en. In: *Quarterly Journal of the Royal Meteorological Society* 137.654, pp. 129–147. ISSN: 00359009. DOI: 10.1002/qj.728. URL: https://onlinelibrary.wiley.com/doi/10.1002/qj.728 (visited on 01/08/2023).

Turetsky, Merritt R., Benjamin W. Abbott, Miriam C. Jones, Katey Walter Anthony, David Olefeldt, Edward A. G. Schuur, Charles Koven, A. David McGuire, Guido Grosse, Peter Kuhry, Gustaf Hugelius, David M. Lawrence, Carolyn Gibson, and A. Britta K. Sannel (2019). "Permafrost collapse is accelerating carbon release". In: *Nature* 569, pp. 32–34. URL: https://www.nature.com/articles/d41586-019-01313-4.

Turetsky, Merritt R., Benjamin W. Abbott, Miriam C. Jones, Katey Walter Anthony, David Olefeldt, Edward A.G. Schuur, Guido Grosse, Peter Kuhry, Gustaf Hugelius, Charles Koven, David M. Lawrence, Carolyn Gibson, A. Britta K. Sannel, and A. David McGuire (2020). "Carbon release through abrupt permafrost thaw". In: *Nature Geoscience* 13.2, pp. 138–143. ISSN: 17520908. DOI: 10.1038/s41561-019-0526-0. URL: http://dx.doi.org/10.1038/s41561-019-0526-0.

Turney, Chris S. M., Christopher J. Fogwill, Nicholas R. Golledge, Nicholas P. McKay, Erik van Sebille, Richard T. Jones, David Etheridge, Mauro Rubino, David P. Thornton,

Siwan M. Davies, Christopher Bronk Ramsey, Zoë A. Thomas, Michael I. Bird, Niels C. Munksgaard, Mika Kohno, John Woodward, Kate Winter, Laura S. Weyrich, Camilla M. Rootes, Helen Millman, Paul G. Albert, Andres Rivera, Tas van Ommen, Mark Curran, Andrew Moy, Stefan Rahmstorf, Kenji Kawamura, Claus-Dieter Hillenbrand, Michael E. Weber, Christina J. Manning, Jennifer Young, and Alan Cooper (Feb. 2020). "Early Last Interglacial ocean warming drove substantial ice mass loss from Antarctica". en. In: *Proceedings of the National Academy of Sciences* 117.8, pp. 3996–4006. ISSN: 0027-8424, 1091-6490. DOI: 10.1073/pnas.1902469117. URL: https://pnas.org/doi/full/10.1073/pnas.1902469117 (visited on 01/17/2023).

UNFCCC (2015). *Paris Agreement*. URL: https://treaties.un.org/pages/ViewDetails.aspx?src=TREATY&mtdsg_no=XXVII-7-d&chapter=27&clang=_en.

Van Breedam, Jonas, Heiko Goelzer, and Philippe Huybrechts (Nov. 2020). "Semi-equilibrated global sea-level change projections for the next 10 000 years". en. In: *Earth System Dynamics* 11.4, pp. 953–976. ISSN: 2190-4987. DOI: 10.5194/esd-11-953-2020. URL: https://esd.copernicus.org/articles/11/953/2020/ (visited on 01/09/2023).

Van Huissteden, J. (2020). *Thawing Permafrost - Permafrost Carbon in a Warming Arctic*. Cham, Switzerland: Springer Nature Switzerland AG. ISBN: 978-3-030-31379-1.

Van Marle, Margreet J.E., Silvia Kloster, Brian I. Magi, Jennifer R. Marlon, Anne Laure Daniau, Robert D. Field, Almut Arneth, Matthew Forrest, Stijn Hantson, Natalie M. Kehrwald, Wolfgang Knorr, Gitta Lasslop, Fang Li, Stéphane Mangeon, Chao Yue, Johannes W. Kaiser, and Guido R. Van Der Werf (2017). "Historic global biomass burning emissions for CMIP6 (BB4CMIP) based on merging satellite observations with proxies and fire models (1750-2015)". In: *Geoscientific Model Development* 10.9, pp. 3329–3357. ISSN: 19919603. DOI: 10.5194/gmd-10-3329-2017.

Walter Anthony, Katey, Thomas Schneider von Deimling, Ingmar Nitze, Steve Frolking, Abraham Emond, Ronald Daanen, Peter Anthony, Prajna Lindgren, Benjamin Jones, and Guido Grosse (2018). "21St-Century Modeled Permafrost Carbon Emissions Accelerated By Abrupt Thaw Beneath Lakes". In: *Nature Communications* 9.1. ISSN: 20411723. DOI: 10.1038/s41467-018-05738-9. URL: http://dx.doi.org/10.1038/s41467-018-05738-9.

Wang, Lei, James L. Davis, and Ian M. Howat (2021). "Complex Patterns of Antarctic Ice Sheet Mass Change Resolved by Time-Dependent Rate Modeling of GRACE and GRACE Follow-On Observations". en. In: *Geophysical Research Letters* 48.1. _eprint: https://onlinelibrary.wiley.com/doi/pdf/10.1029/2020GL090961, e2020GL090961. ISSN: 1944-8007. DOI: 10.1029/2020GL090961. URL: https://onlinelibrary.wiley.com/doi/abs/10.1029/2020GL090961 (visited on 01/19/2023).

Wang, Seaver, Adrianna Foster, Elizabeth A. Lenz, John D. Kessler, Julienne C. Stroeve, Liana O. Anderson, Merritt Turetsky, Richard Betts, Sijia Zou, Wei Liu, William R. Boos, and Zeke Hausfather (Mar. 2023). "Mechanisms and Impacts of Earth System Tipping Elements". en. In: *Reviews of Geophysics* 61.1. ISSN: 8755-1209, 1944-9208. DOI: 10.1029/2021RG000757. URL: https://onlinelibrary.wiley.com/doi/10.1029/2021RG000757 (visited on 03/01/2023).

Weertman, J. (1974). "Stability of the Junction of an Ice Sheet and an Ice Shelf". en. In: *Journal of Glaciology* 13.67, pp. 3–11. ISSN: 0022-1430, 1727-5652. DOI: 10.3189/S0022143000023327. URL: https://www.cambridge.org/core/product/identifier/S0022143000023327/type/journal_article (visited on 01/18/2023).

Wenzel, Sabrina, Peter M. Cox, Veronika Eyring, and Pierre Friedlingstein (2014). "Emergent constraints on climate-carbon cycle feedbacks in the CMIP5 Earth system models". In: *Journal of Geophysical Research: Biogeosciences* 119.5, pp. 794–807. ISSN: 21698961. DOI: 10.1002/2013JG002591.

Wilkinson, C. (2004). *Status of Coral Reefs of The World: 2004*. Townsville, Queensland: Global Coral Reef Monitoring Network. URL: https://portals.iucn.org/library/sites/library/files/documents/2004-074-1.pdf.

Wilson, David J., Rachel A. Bertram, Emma F. Needham, Tina van de Flierdt, Kevin J. Welsh, Robert M. McKay, Anannya Mazumder, Christina R. Riesselman, Francisco J. Jimenez-Espejo, and Carlota Escutia (Sept. 2018). "Ice loss from the East Antarctic Ice Sheet during late Pleistocene interglacials". en. In: *Nature* 561.7723, pp. 383–386. ISSN: 0028-0836, 1476-4687. DOI: 10.1038/s41586-018-0501-8. URL: http://www.nature.com/articles/s41586-018-0501-8 (visited on 01/20/2023).

Wood, Richard A., José M. Rodríguez, Robin S. Smith, Laura C. Jackson, and Ed Hawkins (Dec. 2019). "Observable, low-order dynamical controls on thresholds of the Atlantic meridional overturning circulation". en. In: *Climate Dynamics* 53.11, pp. 6815–6834. ISSN: 0930-7575, 1432-0894. DOI: 10.1007/s00382-019-04956-1. URL: http://link.springer.com/10.1007/s00382-019-04956-1 (visited on 03/03/2023).

Wunderling, Nico, Jonathan F. Donges, Jürgen Kurths, and Ricarda Winkelmann (2021). "Interacting tipping elements increase risk of climate domino effects under global warming". In: *Earth System Dynamics* 12.2, pp. 601–619. ISSN: 21904987. DOI: 10.5194/esd-12-601-2021.

Zhang, Y., X. Wang, R. Fraser, I. Olthof, W. Chen, D. McLennan, S. Ponomarenko, and W. Wu (2013). "Modelling and mapping climate change impacts on permafrost at high spatial resolution for an Arctic region with complex terrain". In: *Cryosphere* 7.4, pp. 1121–1137. ISSN: 19940416. DOI: 10.5194/tc-7-1121-2013.

# Appendix

## Derivation of CTEM Formulation

To derive the discrete form of CTEM (eq. 5), we start by rewriting the logistic equation for $S$ (eq. 2)

$$\frac{dS}{dt} = r\frac{T}{P}S - \frac{rT}{PK}S^2 \tag{7}$$

We simplify this equation by defining $a$ and $b$ as

$$a \coloneqq r\frac{T}{P} \tag{8}$$

$$b \coloneqq \frac{rT}{PK}. \tag{9}$$

With those definitions, we can rewrite eq. 7 as

$$\frac{dS}{dt} = aS - bS^2. \tag{10}$$

We further define

$$u \coloneqq S^{-1}, \tag{11}$$

which gives us

$$S = u^{-1},$$
$$\frac{dS}{du} = -u^{-2}\frac{du}{dt},$$

with which we can rewrite eq. 10 as

$$-u^{-2}\frac{du}{dt} = au^{-1} - bu^{-2}. \tag{12}$$

We multiply eq. 12 with $-u^2$ and rearrange which gives us

$$\frac{du}{dt} + au = b. \tag{13}$$

As eq. 13 is a Bernoulli differential equation, we know that an exact solution exists, which can be derived analytically. Since output variables from FaIR such as $T$ are treated as constant between timesteps, this also holds for $a$ and $b$ which are calculated using eq. 8 and eq, 9 with $T = T(\overline{t-1})$. Hence, eq. 13 is a Bernoulli differential equation with constant coefficients

which can be solved with an integrating factor $I$ defined as

$$I := e^{at}.$$

We now multiply eq. 13 with $I$ which yields

$$e^{at}\frac{du}{dt} + e^{at}au = be^{at}.$$

This equation is now integrated from $t-1$ to $t$ to give the new solution for $u$ at $t$

$$\int_{t-1}^{t} e^{at'}\frac{du}{dt'} + e^{at'}au \; dt' = \int_{t-1}^{t} be^{at'} \; dt'.$$

The left-hand integral can now be solved using the chain rule

$$\left[e^{at'}u\right]_{t-1}^{t} = b\int_{t-1}^{t} e^{at'} \; dt'.$$

The right-hand integral can be solved directly, and we derive

$$e^{at}U_2 - e^{a(t-1)}U_1 = \frac{b}{a}\left(e^{at} - e^{a(t-1)}\right).$$

Here, $u$ is a function of $t$ but to prevent confusion of brackets, we write $U_2$ for $u(t)$ and $U_1$ for $u(t-1)$. We simplify this equation by dividing by $e^{at}$ and defining $\Delta t := t - (t-1)$

$$U_2 - e^{-a\Delta t}U_1 = \frac{a}{b}\left(1 - e^{-a\Delta t}\right).$$

Now, we resubstitute for $u$ using eq. 11

$$S_2^{-1} - e^{-a\Delta t}S_1^{-1} = \frac{b}{a}\left(1 - e^{-a\Delta t}\right),$$

which can be rewritten as

$$S_2 = \left(e^{-a\Delta t}\left(S_1^{-1} - \frac{b}{a}\right) + \frac{b}{a}\right)^{-1}.$$

Explicitly showing the time dependency of $S$, $b$ and $a$, we derive the final form of eq. 5

$$S(t) = \left(e^{-a(\overline{t-1})\Delta t}\left(S^{-1}(t-1) - \frac{b(\overline{t-1})}{a(\overline{t-1})}\right) + \frac{b(\overline{t-1})}{a(\overline{t-1})}\right)^{-1}.$$

As explained in Sec.2.3, bars over $t$ denote that the respective variable is treated as the average value between two gridpoints, whereas variables without a bar over $t$ are defined at the gridpoints (Fig. 3).

## Probability Distributions used by rriskDistributions

The rriskDistributions package chooses out of the following probability distributions: Normal, Beta, Cauchy, Logistic, Student T, Chi-squared, Non-central Chi-squared, Exponential, Fisher, Gamma, Log-normal, Continuous uniform, Weibull, Triangular, Gompertz, PERT, Truncated normal.

## Additional Plots

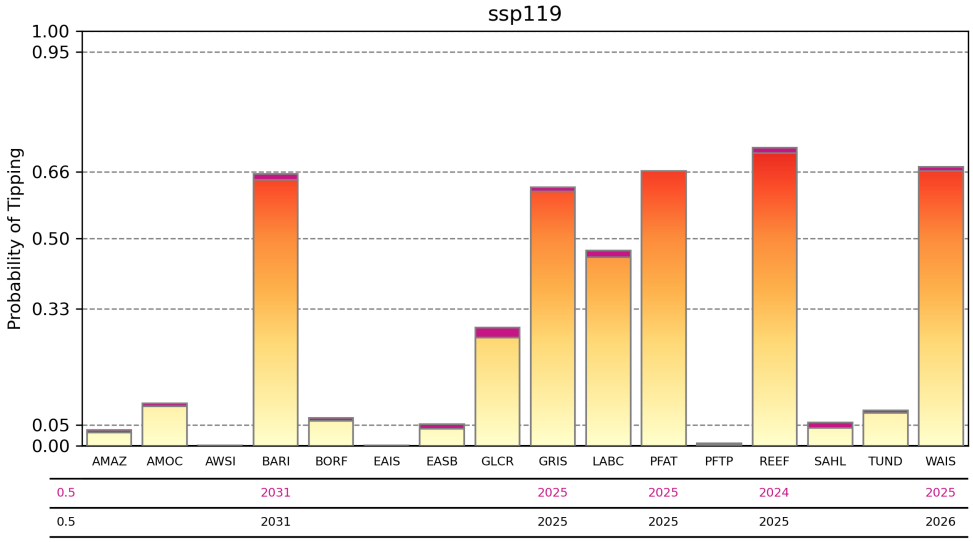


**Figure 32:** Probabilities of triggering the TEs until 2200 under SSP1-1.9. Additional probabilities from the carbon TEs are marked in purple. The table underneath states the years in which the 50% probability is crossed, with purple including carbon emissions from carbon TEs and black not.

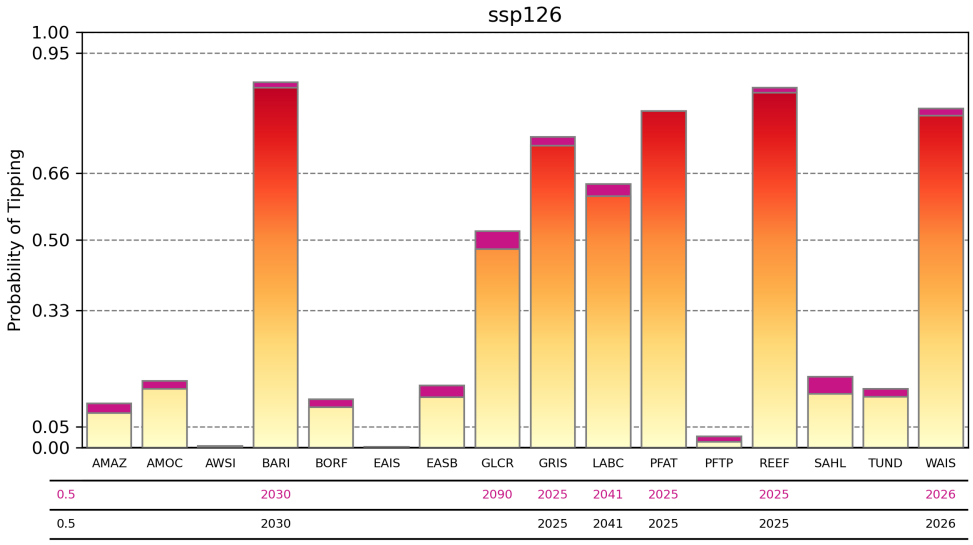


**Figure 33:** Probabilities of triggering the TEs until 2200 under SSP1-2.6. Additional probabilities from the carbon TEs are marked in purple. The table underneath states the years in which the 50% probability is crossed, with purple including carbon emissions from carbon TEs and black not.

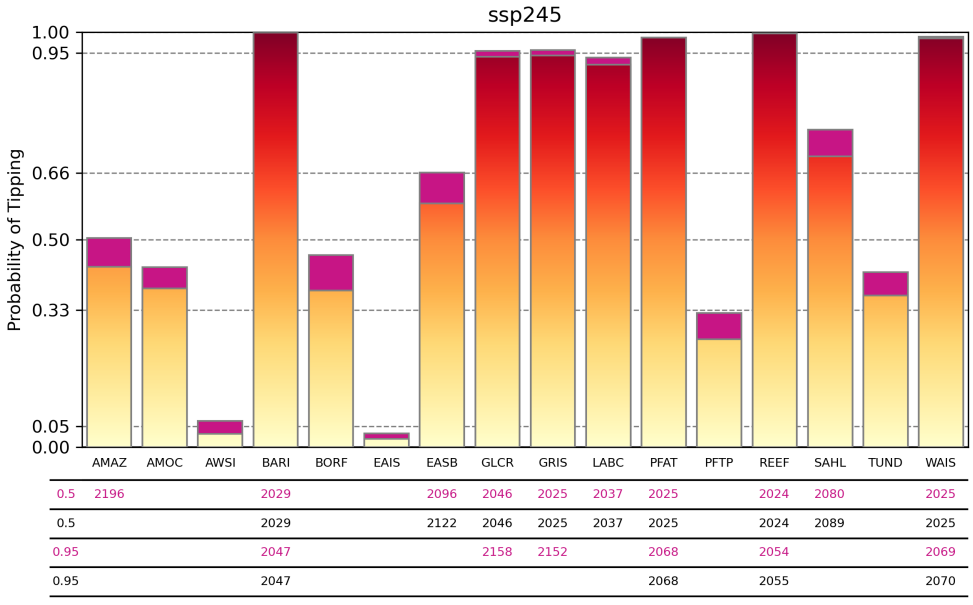


**Figure 34:** Probabilities of triggering the TEs until 2200 under SSP2-4.5. Additional probabilities from the carbon TEs are marked in purple. The table underneath states the years in which the 50% and the 95% probability are crossed, with purple including carbon emissions from carbon TEs and black not.

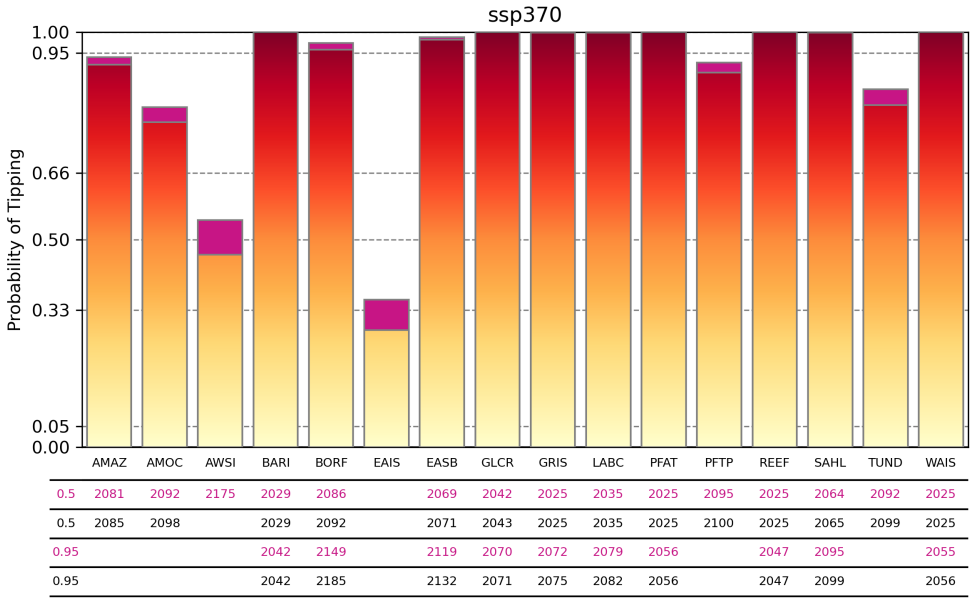


**Figure 35:** Probabilities of triggering the TEs until 2200 under SSP3-7.0. Additional probabilities from the carbon TEs are marked in purple. The table underneath states the years in which the 50% and the 95% probability are crossed, with purple including carbon emissions from carbon TEs and black not.

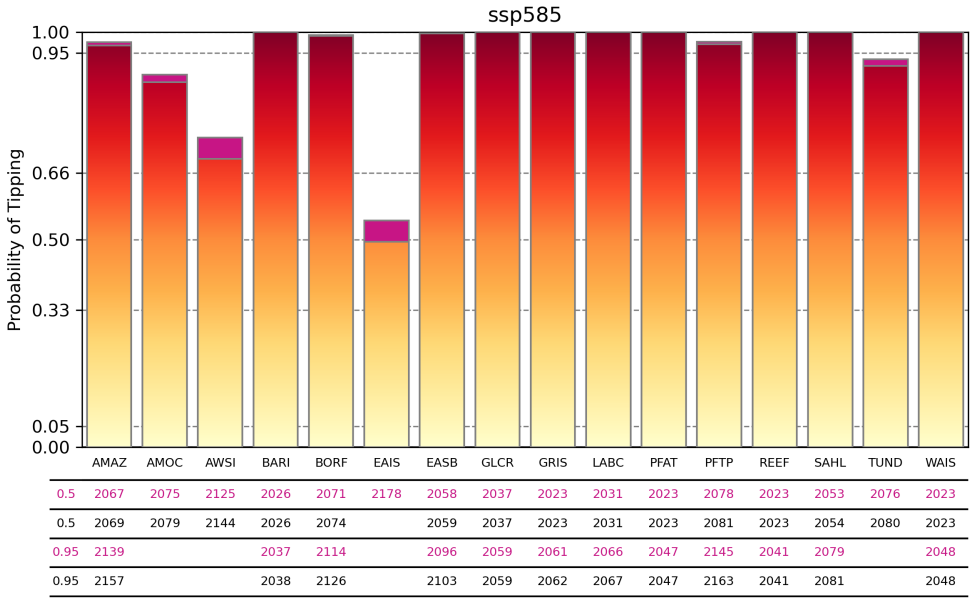


**Figure 36:** Probabilities of triggering the TEs until 2200 under SSP5-8.5. Additional probabilities from the carbon TEs are marked in purple. The table underneath states the years in which the 50% and the 95% probability are crossed, with purple including carbon emissions from carbon TEs and black not.

# Eidesstattliche Erklärung

Hiermit versichere ich an Eides statt, dass ich die vorliegende Arbeit im Studiengang Integrated Climate System Sciences selbstständig verfasst und keine anderen als die angegebenen Hilfsmittel – insbesondere keine im Quellenverzeichnis nicht benannten Internet-Quellen – benutzt habe. Alle Stellen, die wörtlich oder sinngemäß aus Veröffentlichungen entnommen wurden, sind als solche kenntlich gemacht. Ich versichere weiterhin, dass ich die Arbeit vorher nicht in einem anderen Prüfungsverfahren eingereicht habe und die eingereichte schriftliche Fassung der auf dem elektronischen Speichermedium entspricht.

Datum: 06.04.2023 Unterschrift: